VOLUME 9 NUMBER 3-4 2022 ISSN 2409-6121; eISSN 2522-1361

Physical Sciences and Technology

National Nanotechnological Laboratory of Open Type
Institute of Experimental and Theoretical Physics

Physical Sciences and Technology is publishing two number in a year by al-Farabi Kazakh
National University, al-Farabi ave., 71, 050040, Almaty, the Republic of Kazakhstan
website: http://phst.kaznu.kz/

Any inquiry for subscriptions should be send to:
Gauhar Mussabek, al-Farabi Kazakh National University
al-Farabi ave., 71, 050040, Almaty, the Republic of Kazakhstan
e-mail: gauharmussabek@gmail.com

SCOPE AND AIM

Physical Sciences and Technology provides an original paperback for the publication of peerreviewed research and review articles in all fields of Physics and related Technology. The topics, included in the scope, especially emphasize understanding of the physics underlying modern technology.

Subject areas may include, but are not limited to the following fields: Astronomy and Space Research, Theoretical Physics and Astrophysics, Plasma Physics and Related Technology, Chemical Physics and Related Technology, Condensed Matter Physics and Related Technology, Thermal physics and Related Technology, Nuclear Physics and Related Technology, Nanomaterials and Nanotechnology, Applied Atomic and Molecular Physics, Material Sciences and Related Technology, Electronics and Related Technology, Instrumentation, Photonics and Quantum Electronics, Signal processing.

The Journal is issued under the auspices of the National Nanotechnological Laboratory of Open Type and Institute of Experimental and Theoretical Physics and is published two times a year by the «Kazakh University» Publishing House. The International Editorial Board of the Journal consists of leading researchers from different countries of the world. The Journal is wide open for contributions that both lie at the far frontiers of contemporary physics and are particularly aimed at applications of the scientific principles of physics to modern technological problems.

Physical Sciences and Technology. Vol. 9 (No. 3-4), 2022: 4-12

IRSTI 29.19.22 https://doi.org/10.26577/phst.2022.v9.i2.01

Investigation and evaluation of the morphology properties of carbon nanowalls based on fractal analysis and Minkowski functionals

Ye. Yerlanuly[1,2], R. R. Nemkayeva[1],
R. Ye. Zhumadilov[1] and M. T. Gabdullin[1*]

[1]Kazakh-British Technical University, Almaty, Kazakhstan
[2]Institute of Applied Science and Information Technologies, Almaty, Kazakhstan
*e-mail: *gabdullin@physics.kz

(Received 03 August 2022; received in revised form 20 September; accepted 28 October 2022)

It is well-known that at the nano-scale, morphology can play a crucial role in the properties of nanomaterials and there is still a challenging task to control it during the synthesis. In this work, the morphology of carbon nanowalls (CNWs) is studied and evaluated on the basis of fractal analysis and Minkowski functionals. Synthesis of CNWs was carried out using ICP-PECVD method at different growth times. The obtained samples were examined using atomic force microscopy (AFM) with subsequent processing of the obtained data using the Gwyddion 2.55 program, which provides a fractal analysis including the height-height correlation function and the power spectral density function. The Minkowski functionals were plotted for evaluation of the morphology of the CNWs. The process of the formation of CNWs was considered depending on the synthesis duration. A possible time-dependent growth mechanism with certain stages of nanostructures formation is proposed. The correlation between the calculated parameters of morphology and the electrical properties of CNWs was revealed.

Keywords: carbon nanowalls, Minkowski functionals, fractal analysis, atomic force microscopy, Gwyddion 2.55 program.
PACS number: 61.46.+w.

1 Introduction

Today, nanomaterials and nanotechnology play an increasingly important role in many key sectors of human activity in the new millennium [1]. An analysis of the state and trends in the current developing nanotechnology allows us to assert that nanostructured carbon materials are very promising objects for practical application in various industries [2–5]. One of the promising carbon nanomaterials is carbon nanowalls, which are a type of carbon nanostructure consisting of graphene sheets arranged vertically on a substrate in the form of walls with a wall thickness of several to tens of nanometers [6, 7]. To date, materials based on CNWs have already been applied in various electronic devices, such as solar cells [8, 9], LEDs [10, 11], gas sensors [12,13], etc.

Currently, work on the synthesis of carbon nanowalls with a predefined morphology is being actively carried out [6, 14, 15]. Recently the effect of morphology on various physical properties (optical, electrical, etc.) of CNWs has been revealed [16]. In this regard, one of the important issues of nanotechnology is the characterization of morphological properties of nanomaterials. It is well known that today the study of morphology is carried out using scanning electron microscopy and scanning probe microscopy [17], etc. However, the results obtained require additional interpretation; therefore, Minkowski functionals and fractal analysis currently used for these purposes provide information on the geometrical parameters of the structure and morphology of the nanomaterial system [18–20]. This work emphasizes on the study and the evaluation of the morphological characteristics of CNWs synthesized on a quartz substrate [16] based on the Minkowski functionals and fractal analysis. In addition, the correlation of the electrical properties of CNWs with the obtained morphological parameters is analyzed.

2 Methods and analysis

CNW films on quartz substrates were synthesized by the ICP-PECVD method. The synthesis process and characteristics of the resulting material are presented in more detail in our previous work [16]. Since this article is aimed at the evaluation of the morphological characteristics of CNWs depending on the synthesis time and assessing the relationship between morphology and electrical properties, the results of the morphology analysis were processed using the Gwyddion 2.55 program [21, 22], where the height-height correlation function, the power spectral density function and Minkowski functionals were calculated. More details about the analysis methods and the Gwyddion 2.55 program are described in [20].

3 Results and discussion

The electrical properties of the synthesized CNWs as a function of growth time were previously reported in [16] and are given in Table 1. As can be seen, there is a trend towards an increase in height and a decrease in surface resistance as a function of synthesis time. The specific conductivity of the samples is approximately the same depending on the synthesis time, with the exception of the sample grown for 50 min, which demonstrates a small minimum. In [16], this effect was explained by a change of the morphological and structural properties (ratio of Raman peaks and degree of graphitization) of CNWs depending on the synthesis time. However, a complete morphological analysis based on the calculated height-height correlation function, power spectral density function, and Minkowski functionals was not carried out.

Figure 1 shows 3D models of the CNWs at different synthesis durations. As can be seen, the morphology of the obtained CNWs differs significantly, both in height and in the topology. As in previously reported papers [20,23,24], the fractal analysis was carried out by means of the height-height correlation H(r) and power spectral density (PSD) functions. Figure 2a shows log plots of H(r) for four surfaces. H(r) is a function for determining fractal dimension using the power of difference between the points on different surface structural units (roughness). The resultanting plots are characterized by two modes; the first is a linear region at small *r* values and the second is a nonlinear region at large *r* values. Nonlinear regions have oscillatory characteristics. Such observations are typical for self-affine surfaces [20,23,24]. The graph shows an increase in the value of H (r) depending on the time of CNWs synthesis. It is noteworthy that the curve of the sample obtained at 50 min differs from the others. The value of α for the samples synthesized at 30,40,60 min is very similar and has a value of the order of ~1.2, while for the case of 50 min it equals to ~1.3. An increase in the value of α indicates a higher surface roughness [25].

Table 1 – Thickness and electrical properties of CNWs as a function of growth time [16]

Synthesis duration	**Height, nm**	**Sheet resistance, Ω/cm**	**Electrical conductivity, $\Omega^{-1}cm^{-1}$**
30 min	60	~2000	~80
40 min	85	~1600	~70
50 min	160	~900	~60
60 min	190	~600	~70

Next, fractal analysis was performed using Power Spectral Density Functions (PSDF), corresponding results are presented in logarithmic scales in Figure 2b. The plots are characterized by approximately constant PSDF values, which is smooth region at very low spatial frequencies, an area of constant slope, and a plateau at very high spatial frequencies. These characteristics are typical for surfaces with dominant random properties (self-affine) and less periodic behavior [26]. In addition, an increase in the PSDF value depending on the time of synthesis of CNWs is observed. The slope of the PSDF curve (γ) corresponds to various evolutionary processes occurring on the surface [27]. The γ value was estimated from the slope of the linear approximation of the high-frequency region of the PSDF curve (see Fig. 2b). The value of γ is ~2.4 for CNW films synthesized at 30–40 min. While in the case of synthesis at 50–60 min, an increase in the γ value up to ~2.5 of is observed. Thus, the obtained values of γ, which are rather close ~2.4–2.5, indicate diffusion processes associated with the morphological evolution of CNW films [25, 28].

Two-dimensional Minkowski functionals, volume (V), boundary length (S), and connectivity/Euler characteristic (χ), depicted in Figure 3, are used to describe morphological features that cannot be determined using classical image analysis methods. Minkowski functionals imply the division of the received images into two parts (upper and lower) based on a threshold value. The upper and lower regions correspond to plateaus and valleys, respectively.

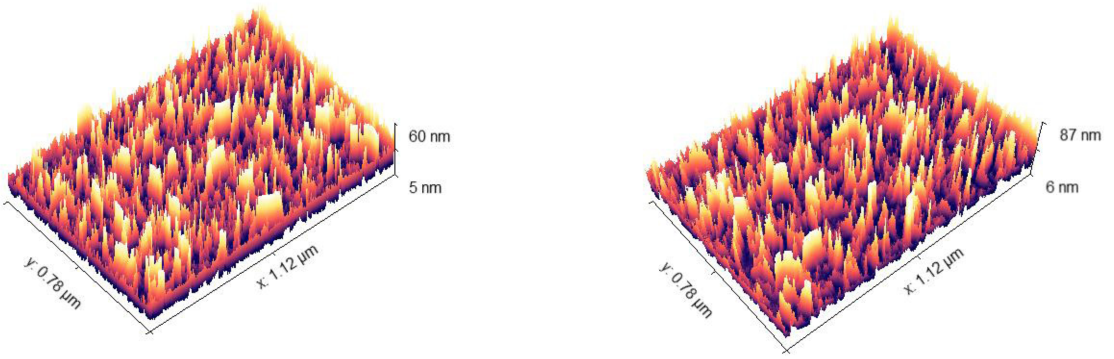

30 min 40 min

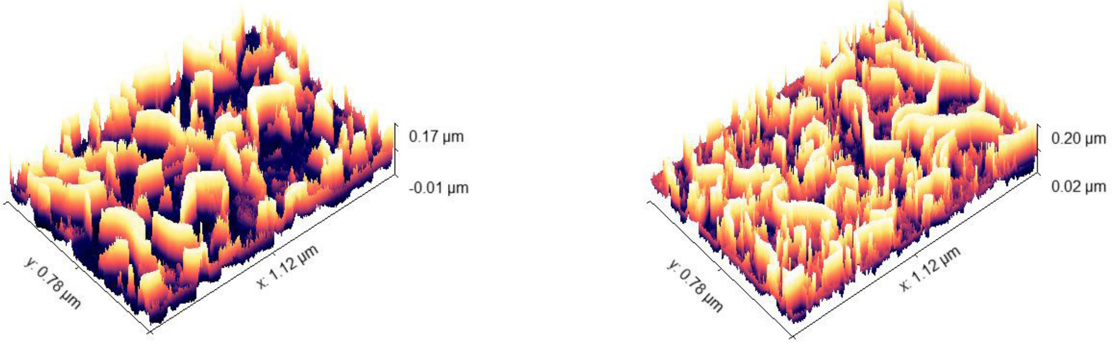

50 min 60 min

Figure 1 – 3D models of CNWs synthesized at different growth times

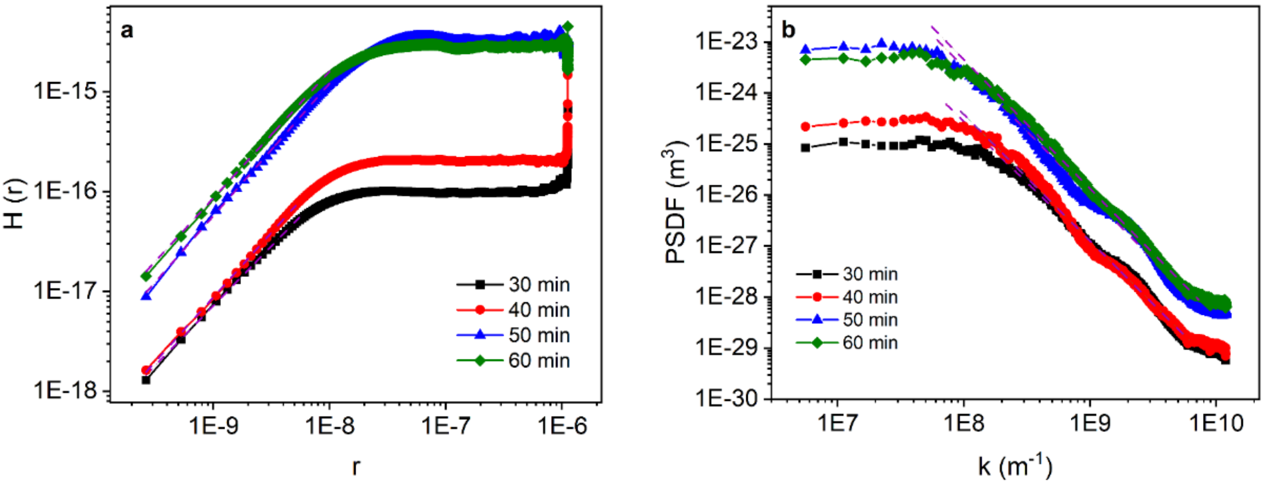

Figure 2 – (a) Double log plots of height–height correlation (H) as a function of shift (r) for CNWs, (b) double log plots of power spectral density (PSDF) as a function of the spatial frequency for CNWs

The Minkowski volume functional V, which basically shows surface coverage, varies across the samples. Figure 3a shows that the distributions in the samples obtained at 30, 40 and 60 minutes are very similar and the functionals are symmetrical. While the functional of the sample synthesized at 50 min is very different and asymmetric. Large V values indicate the dominance of high regions (plateaus), while small values are due to the dominance of trenches and tiny holes (valleys) on the surface.

The Minkowski boundary length (S) characterizes the global perimeter of any region (low or high region) and has the dimension of length. This parameter describes the character of the morphology of the film surface. Figure 3b shows curves similar for samples obtained at 30-, 40- and 60-minutes growth times, however, with increasing duration of synthesis of the CNWs leads to decrease in the value of S, which also indicates a decrease in the specific surface area and in roughness. The analysis results for the samples at 50 min are quite different. A shift of the peak is observed and the intensity is much greater compared to that for the samples at 40 and 60 min. This is apparently due to an increase in the roughness of the sample and a decrease in the density of the walls.

The Minkowski connectivity (χ) characterizes the difference in the number of high- and low-level regions and describes the topological pattern (fractal nature) of a microphotograph. χ is a characteristic of properties that depend on the relationship of nanostructures in the network, such as the percolation threshold, conductivity, and others associated with the transfer of gas, heat, electrons, etc. between nanostructures [29].

Positive values of χ mean the predominance of high-domain features on the surfaces. Negative values indicate the prevalence of valleys, a minimum indicates the highest density of valleys, and a maximum value corresponds to the densest peaks. As it is seen from Figure 3c, the χ value decreases depending on the synthesis time at 30, 40, and 60 min, which also indicates a decrease in the degree of roughness. There is a considerable difference at the synthesis time of 50 min, which is not consistent with other curves of connectivity. In particular, there is a noticeable shift in the peak position, which most likely describes the distinctive morphology of this sample.

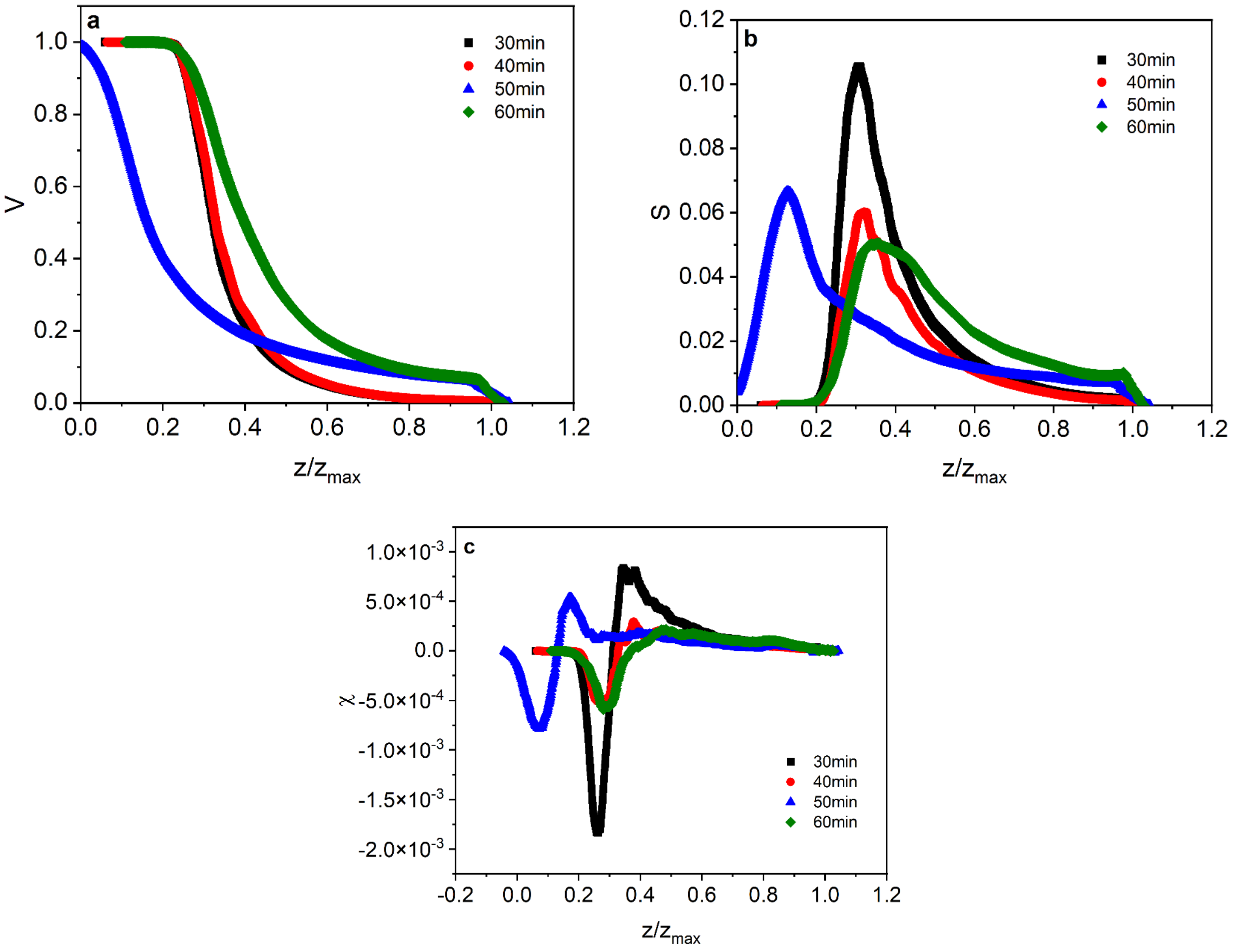

Figure 3 – Two-dimensional Minkowski functionals of carbon nanowalls (a) volume, (b) boundary length, (c) connectivity

The significant difference in the morphology of the samples obtained at 50 min from the rest is probably can be explained by the fact that depending on time a kind of cyclic growth process occurs during the synthesis of CNWs [30–32]. After the formation of initial CNWs, an increase in time leads to vertical growth of certain walls, the density of which comparatively low. A further increase in time leads to a growth of the CNWs in the horizontal direction, i.e., the wall density increases. Thus, an increase in synthesis time leads to the synthesis of CNWs with different morphology and structure, which in turn leads to a change in the electrical properties. Analysis of the results based on fractal analysis and Minkowski functionals (see Figure 2-3) indicate a distinctive morphology for the sample synthesized at 50 min, the density of CNWs in these samples is much lower compared to others, which leads to a minimum value of conductivity (see table one).

4 Conclusions

In this work, we studied and evaluated the morphological characteristics of CNWs synthesized on quartz substrates by the ICP-PECVD method. Morphology was evaluated usifn fractal analysis and Minkowski functionals. The dependence of the morphology of the obtained CNWs on the synthesis time was determined, which is also significantly noticeable when evaluating the fractality, roughness, and Minkowski functionals. The analysis results of the height-height correlation, power spectral density functions and two-dimensional Minkowski functionals, boundary length (S), volume (V), and connectivity / Euler characteristic (χ) indicate a significant difference in the morphology of the samples obtained at 50 min, which further explains the minimum value of specific electrical conductivity for this sample. The process of CNWs formation was considered depending on the synthesis time, and the effect of morphology on the electrical properties of CNWs was revealed.

Acknowledgments

This research was funded by the Science Committee of the Ministry of Education and Science of the Republic of Kazakhstan (Grant № AP08856684).

References

1. E. Inshakova, A. Inshakova. Nanomaterials and nanotechnology: prospects for technological re-equipment in the power engineering industry // IOP Conf. Ser. Mater. Sci. Eng. – 2020. -Vol. 709. -P. 033020. https://doi.org/10.1088/1757-899X/709/3/033020.

2. A. Roshani, M. Mousavizadegan, M. Hosseini. Carbon nanomaterials-based sensors for biomedical applications, in: Carbon Nanomater. Sensors, Elsevier, 2022: pp. 59–75. https://doi.org/10.1016/B978-0-323-91174-0.00003-2.

3. S. Doddamani, V.H. Mariswamy, V.K. Boraiah, S. Ningaiah. Trends in carbon nanomaterial-based sensors in the food industry, in: Carbon Nanomater. Sensors, Elsevier, 2022: pp. 95–103. https://doi.org/10.1016/B978-0-323-91174-0.00002-0.

4. M.I.S. J, S. S, P. Senthil Kumar, V.G. K, New analytical strategies amplified with carbon-based nanomaterial for sensing food pollutants // Chemosphere. -2022. -Vol. -P. 133847. https://doi.org/10.1016/j.chemosphere.2022.133847

5. U. Chadha, S.K. Selvaraj, S. Vishak Thanu, V. Cholapadath, A.M. Abraham, M. Zaiyan, M. Manikandan, V. Paramasivam. A review of the function of using carbon nanomaterials in membrane filtration for contaminant removal from wastewater // Mater. Res. Express. – 2022 – Vol.9 – P.012003 https://doi.org/10.1088/2053-1591/ac48b8

6. Y. Yerlanuly, D. Christy, N. Van Nong, H. Kondo, B. Alpysbayeva, R. Nemkayeva, M. Kadyr, T. Ramazanov, M. Gabdullin, D. Batryshev, M. Hori. Synthesis of carbon nanowalls on the surface of nanoporous alumina membranes by RI-PECVD method // Appl. Surf. Sci. – 2020. – Vol.523. – P.146533. https://doi.org/10.1016/j.apsusc.2020.146533

7. M. Hiramatsu, M. Hori. Carbon Nanowalls, Springer Vienna, Vienna, 2010. https://doi.org/10.1007/978-3-211-99718-5.

8. C. Yang, H. Bi, D. Wan, F. Huang, X. Xie, M. Jiang. Direct PECVD growth of vertically erected graphene walls on dielectric substrates as excellent multifunctional electrodes // J. Mater. Chem. A. – 2013. – Vol.1. – P.770–775. https://doi.org/10.1039/C2TA00234E

9. J. Liu, W. Sun, D. Wei, X. Song, T. Jiao, S. He, W. Zhang, C. Du. Direct growth of graphene nanowalls on the crystalline silicon for solar cells // Appl. Phys. Lett. – 2015 – Vol.106. – P.043904. https://doi.org/10.1063/1.4907284.

10. T.-H. Han, Y. Lee, M.-R. Choi, S.-H. Woo, S.-H. Bae, B.H. Hong, J.-H. Ahn, T.-W. Lee. Extremely efficient flexible organic light-emitting diodes with modified graphene anode // Nat. Photonics. – 2012. – Vol. 6. – P.105–110. https://doi.org/10.1038/nphoton.2011.318

11. H. Ci, H. Chang, R. Wang, T. Wei, Y. Wang, Z. Chen, Y. Sun, Z. Dou, Z. Liu, J. Li, P. Gao, Z. Liu. Enhancement of Heat Dissipation in Ultraviolet Light□Emitting Diodes by a Vertically Oriented Graphene Nanowall Buffer Layer// Adv. Mater. – 2019. – Vol.31. – P.1901624. https://doi.org/10.1002/adma.201901624

12. S. Kwon, H. Choi, S. Lee, G. Lee, Y. Kim, W. Choi, H. Kang. Room Temperature Gas Sensor Application of Carbon Nanowalls using Electrical Resistance Change by Surface Adsorption of Toxic Gases//Mater. Res. Bull. – 2021. – Vol.141. – P.111377. https://doi.org/10.1016/j.materresbull.2021.111377

13. P. Slobodian, U. Cvelbar, P. Riha, R. Olejnik, J. Matyas, G. Filipič, H. Watanabe, S. Tajima, H. Kondo, M. Sekine, M. Hori. High sensitivity of a carbon nanowall-based sensor for detection of organic vapours//RSC Adv. – 2015. – Vol.5. – P.90515–90520. https://doi.org/10.1039/C5RA12000D

14. T. Ichikawa, N. Shimizu, K. Ishikawa, M. Hiramatsu, M. Hori. Synthesis of isolated carbon nanowalls via high-voltage nanosecond pulses in conjunction with CH4/H2 plasma enhanced chemical vapor deposition // Carbon N. Y. – 2020. – Vol.161. – P.403–412. https://doi.org/10.1016/j.carbon.2020.01.064

15. M. Wang, Y. Kim, L. Zhang, W.K. Seong, M. Kim, S. Chatterjee, M. Wang, Y. Li, P. V. Bakharev, G. Lee, S.H. Lee, R.S. Ruoff. Controllable electrodeposition of ordered carbon nanowalls on Cu(111) substrates//Mater. Today. – 2022. – Vol.57. – P.75-83 https://doi.org/10.1016/j.mattod.2022.05.018

16. Y. Yerlanuly, R. Zhumadilov, R. Nemkayeva, B. Uzakbaiuly, A.R. Beisenbayev, Z. Bakenov, T. Ramazanov, M. Gabdullin, A. Ng, V. V. Brus, A.N. Jumabekov. Physical properties of carbon nanowalls synthesized by the ICP-PECVD method vs. the growth time // Sci. Rep. – 2021. – Vol.11. – P.19287. https://doi.org/10.1038/s41598-021-97997-8

17. E. Ortiz Ortega, H. Hosseinian, M.J. Rosales López, A. Rodríguez Vera, S. Hosseini. Characterization Techniques for Morphology Analysis, in: 2022: pp. 1–45. https://doi.org/10.1007/978-981-16-9569-8_1

18. I. Levchenko, J. Fang, K. (Ken) Ostrikov, L. Lorello, M. Keidar. Morphological Characterization of Graphene Flake Networks Using Minkowski Functionals//Graphene. – 2016. – Vol.05. – P.25–34. https://doi.org/10.4236/graphene.2016.51003

19. A. Grayeli Korpi, Ş. Ţălu, M. Bramowicz, A. Arman, S. Kulesza, B. Pszczolkowski, S. Jurečka, M. Mardani, C. Luna, P. Balashabadi, S. Rezaee, S. Gopikishan. Minkowski functional characterization and fractal analysis of surfaces of titanium nitride films//Mater. Res. Express. – 2019. – Vol. 6. – P.086463. https://doi.org/10.1088/2053-1591/ab26be

20. Y. Yerlanuly, R. Nemkayeva, R. Zhumadilov, T. Ramazanov, B. Alpysbayeva, M. Gabdullin. Morphological characterization of carbon nanowalls networks using Minkowski functionals // Jpn. J. Appl. Phys. – 2021. – Vol.60. – P. 115001. https://doi.org/10.35848/1347-4065/ac26e2

21. D. Nečas, P. Klapetek. Gwyddion: an open-source software for SPM data analysis // Open Phys. – 2012. – Vol.10.-P.1. https://doi.org/10.2478/s11534-011-0096-2

22. www.gwyddion.net, (n.d.). www.gwyddion.net

23. F.M. Mwema, E.T. Akinlabi, O.P. Oladijo. Effect of Substrate Type on the Fractal Characteristics of AFM Images of Sputtered Aluminium Thin Films//Mater. Sci. – 2019. – Vol.26. – P.49–57. https://doi.org/10.5755/j01.ms.26.1.22769

24. Ş. Ţălu, R.P. Yadav, O. Šik, D. Sobola, R. Dallaev, S. Solaymani, O. Man. How topographical surface parameters are correlated with CdTe monocrystal surface oxidation // Mater. Sci. Semicond. Process. – 2018. – Vol.85. – P.15–23. https://doi.org/10.1016/j.mssp.2018.05.030

25. A. Pandey, S. Tyagi, B.P. Singh, L. Kumar. Surface Morphological and Optical Evolution of Rf Sputtered Azo Films for Optoelectronic Devices// Physica B: Condensed Matter. – 2022. – Vol. 47. – P. 414393. https://doi.org/10.1016/j.physb.2022.414393

26. C. Buchko. Surface characterization of porous, biocompatible protein polymer thin films // Biomaterials. – 2001. – Vol.22. – P.1289–1300. https://doi.org/10.1016/S0142-9612(00)00281-7

27. P. Dash, P. Mallick, H. Rath, A. Tripathi, J. Prakash, D.K. Avasthi, S. Mazumder, S. Varma, P.V. Satyam, N.C. Mishra. Surface roughness and power spectral density study of SHI irradiated ultra-thin gold films // Appl. Surf. Sci. – 2009. – Vol.256. – P. 558–561. https://doi.org/10.1016/j.apsusc.2009.08.046

28. A.K. Manna, A. Kanjilal, D. Kanjilal, S. Varma. Dynamic Surface evolution and scaling studies on TiO2 thin films by Ti ion implantation//Nucl. Instruments Methods Phys. Res. Sect. B Beam Interact. with Mater. Atoms. – 2020. – Vol.474. – P.68–73. https://doi.org/10.1016/j.nimb.2020.04.031

29. J.-F. Gouyet, A.L.R. Bug. Physics and Fractal Structures // Am. J. Phys. – 1997. – Vol.65. – P. 676–677. https://doi.org/10.1119/1.18629

30. M. Hiramatsu, K. Shiji, H. Amano, M. Hori. Fabrication of vertically aligned carbon nanowalls using capacitively coupled plasma-enhanced chemical vapor deposition assisted by hydrogen radical injection // Appl. Phys. Lett. – 2004.– Vol.84. – P. 4708–4710. https://doi.org/10.1063/1.1762702

31. T. Mori, M. Hiramatsu, K. Yamakawa, K. Takeda, M. Hori. Fabrication of carbon nanowalls using electron beam excited plasma-enhanced chemical vapor deposition // Diam. Relat. Mater. – 2008. – Vol.17. – P. 1513–1517. https://doi.org/10.1016/j.diamond.2008.01.070

32. A. Giese, S. Schipporeit, V. Buck, N. Wöhrl. Synthesis of carbon nanowalls from a single-source metal-organic precursor // Beilstein J. Nanotechnol. – 2018. – Vol.9. – P.1895–1905. https://doi.org/10.3762/bjnano.9.181

Funded by Al-Farabi KazNU

Physical Sciences and Technology. Vol. 9 (No. 3-4), 2022: 11-17

IRSTI 30.19.31 https://doi.org/10.26577/phst.2022.v9.i2.02

Influence of plasma and heat treatments on the properties of ZnO nanorods

D.B. Tolubayeva[1], Y.Y. Kedruk[2] and L.V. Gritsenko[2*]

[1]Karaganda Industrial University, Temirtau, Kazakhstan
[2]Satbayev University, Almaty, Kazakhstan
*e-mail: gritsenko_lv@mail.ru

(Received 31 August 2022; received in revised form 28 September; accepted 5 November 2022)

Oxide semiconductor nanostructured materials attract considerable attention of researchers due to their efficiency in electronics, optics, photonics, and other applications. One-dimensional semiconductor nanostructures such as nanowires, nanorods, and nanotubes are widely used for both academic research and industrial applications. Such nanostructures are useful materials for investigating of the dependence of electrical, thermal, and mechanical properties on dimensionality and size reduction. Actual study is the effect of postgrowth treatments on the properties of synthesized materials in order to improve their optical and electrical characteristics. In this work, we consider the effect of thermal annealing and treatment in hydrogen plasma on the morphology, optical, structural, and photoluminescent properties of samples consisting of zinc oxide nanorods obtained by chemical solution deposition. It is shown that the passivation of charged oxygen acceptors on the surface of grain boundaries upon short-term treatment in hydrogen plasma followed by thermal treatment in air makes it possible to activate the photoluminescence of ZnO obtained by chemical solution deposition and to obtain conductive transparent layers of ZnO nanorods with intense photoluminescence.

Keywords: zinc oxide, chemical deposition, optical properties, photoluminescence, plasma treatment, heat treatment.
PACS number: 61.46.+w; 78.55.Et; 78.55.–m; 81.10.Dn.

1 Introduction

Nowadays, nanostructured materials of oxide semiconductors are used as functional units in the manufacture of electronic, optoelectronic, electrochemical, and electromechanical nanodevices [1–3]. Among one-dimensional nanostructures, zinc oxide (ZnO) nanorods are one of the most important nanomaterials actively used in the modern world [4].

Zinc oxide is a semiconductor material with a direct band gap (3.37 eV) and a high exciton binding energy (60 meV) at room temperature [5]. ZnO is also biocompatible, biodegradable, and biosafe for medical and environmental applications [6]. Under normal conditions, ZnO exhibits the hexagonal wurtzite structure. The structure of ZnO can be described as a series of alternating planes consisting of tetrahedrally coordinated O^{2-} and Zn^{2+} arranged alternately along the axis. Due to their characteristics in electronics, optics, and photonics ZnO nanorods are attractive for use in solar cells [7–9], nanogenerators [10], gas sensors [11], photodetectors [12], and other devices. Among these applications ZnO nanorods are increasingly being used as photocatalysts to inactivate bacteria and viruses as well as to decompose environmental pollutants such as dyes, pesticides, and volatile organic compounds with appropriate light irradiation [13-14].

To obtain ZnO layers with the required properties, different types of post-growth treatment of nanorods are used. Among others, heat treatment in atmosphere and hydrogen plasma treatment are often used. The annealing process is one of the most important methods that can greatly affect the properties of ZnO nanostructures. Many researchers report, that ZnO sensor devices become more sensitive to UV after annealing. Annealing as a surface treatment process can remove surface defects and impurities and change the surface absorption and desorption of oxygen molecules, thereby improving the surface condition of ZnO [15]. It is known that photoconductivity in ZnO nanostructures is controlled by the adsorption and desorption of oxygen on the surface [16]. Consequently, the annealing process can improve the photosensitivity as well as the photoresponse of ZnO by modifying the surface and improving the structure. In turn, annealing in a hydrogen atmosphere is often used to improve the electrical and optical properties of ZnO, since as known hydrogen atoms passivate broken bonds on the surface and energy states in the band gap [17]. During H-plasma treatment several processes occur in ZnO, including the diffusion of thermally and plasma-activated ZnO. Correspondingly, a significant increase in the near edge emission of ZnO was observed in a number of works after treatment with H_2 plasma [18, 19]. The processing leads to the appearance of various hydrogen-related transitions in the NBE emission band. It is assumed that complexes of zinc vacancies with oxygen and hydrogen atoms are responsible for these transitions [20]. It was found that the associated exciton transitions as well as the electronic levels associated with the surface effect on the luminescence spectra of ZnO at the band edge at low temperatures after treatment in H_2 plasma [21] and the emission at the band edge [22]. Another well-known effect caused by surface states in ZnO is the constant photoconductivity, which prevents the dark current from being rapidly restored after UV excitation and is a major drawback for the widespread use of ZnO-based thin-film transistors and photodetectors [23].

In this work we study the effect of thermal annealing, hydrogen plasma treatment, and treatment in hydrogen plasma with preliminary annealing in air on the morphology, optical, structural, and photoluminescent properties of zinc oxide samples, obtained by chemical solution deposition.

2 Description of the experiment and discussion of the results

Nanostructured zinc oxide layers were synthesized by chemical solution deposition. A thin seed layer of ZnO (~1–10 nm) was uniformly deposited on spotless glass substrates by the sol–gel method. The sol solution was prepared by dissolving 0.4 g of zinc acetate ($Zn(CH_3COO)_2$) in 10 ml of ethanol with thorough stirring on a magnetic stirrer at room temperature for two hours. Drying at 110°C and final annealing at a temperature of 450°C for 60 minutes in a muffle furnace led to the formation of uniform over the entire surface of the substrates seed layer.

The synthesis was carried out in a glass beaker on a steam bath for two hours on a heated magnetic stirrer at a temperature of 90°C.

The ZnO rods were grown in an equimolar solution containing 75 mM zinc nitrate $Zn(NO_3)_2\times6H_2O$ (Sigma Aldrich) and 75 mM hexamethylenetetramine $C_6H_{12}N_4$ (HMTA, Sigma Aldrich) dissolved in distilled water (18.2 MΩ×cm). The samples were placed at a slight angle to the vertical, with their faces facing the walls of the beaker. At the end of the synthesis, the samples were washed with distilled water and then dried in an oven at a temperature of 110–115°C.

Thermal annealing was carried out at atmospheric pressure in air in the temperature range from 100°C to 450°C in a quartz tube furnace. Plasma treatment in a hydrogen atmosphere (H-treatment) was carried out in a quartz cylindrical reactor with an inner diameter of 30 mm. During the hydrogen plasma treatment, the frequency of the high-frequency generator, the power of the high-frequency source and the discharge pressure were maintained at 27.12MHz, 15 W and 70 Pa, respectively. Plasma treatment was carried out at room temperature without intentional heating of the substrate; however, the temperature of the substrate during treatment in hydrogen plasma slightly increased to ~60°C due to high frequency absorption.

The results of the study by electron microscopy of ZnO samples synthesized by chemical solution deposition: initial, subjected to thermal annealing in a muffle furnace at a temperature of 450 ° C for one hour (AT), treated in hydrogen plasma (PT), and also treated in hydrogen plasma with preliminary annealing in air (A + PT), – showed that the synthesized samples are homogeneous layers over the entire surface of the substrate, consisting of rods fused at the base, oriented perpendicular to the substrate (Figure 1).

Initial samples have the highest ratio of crystal length to their thickness (aspect ratio AR), while samples subjected to plasma treatment have the lowest AR (Table 1).

Optical properties, such as optical density spectra and transmission spectra, were studied for all synthesized ZnO samples (Figure 2a, 2b, respectively). The results of the analysis of optical properties allowed us to determine the energy gap of the prepared samples using Tauc's method (Figure 2c).

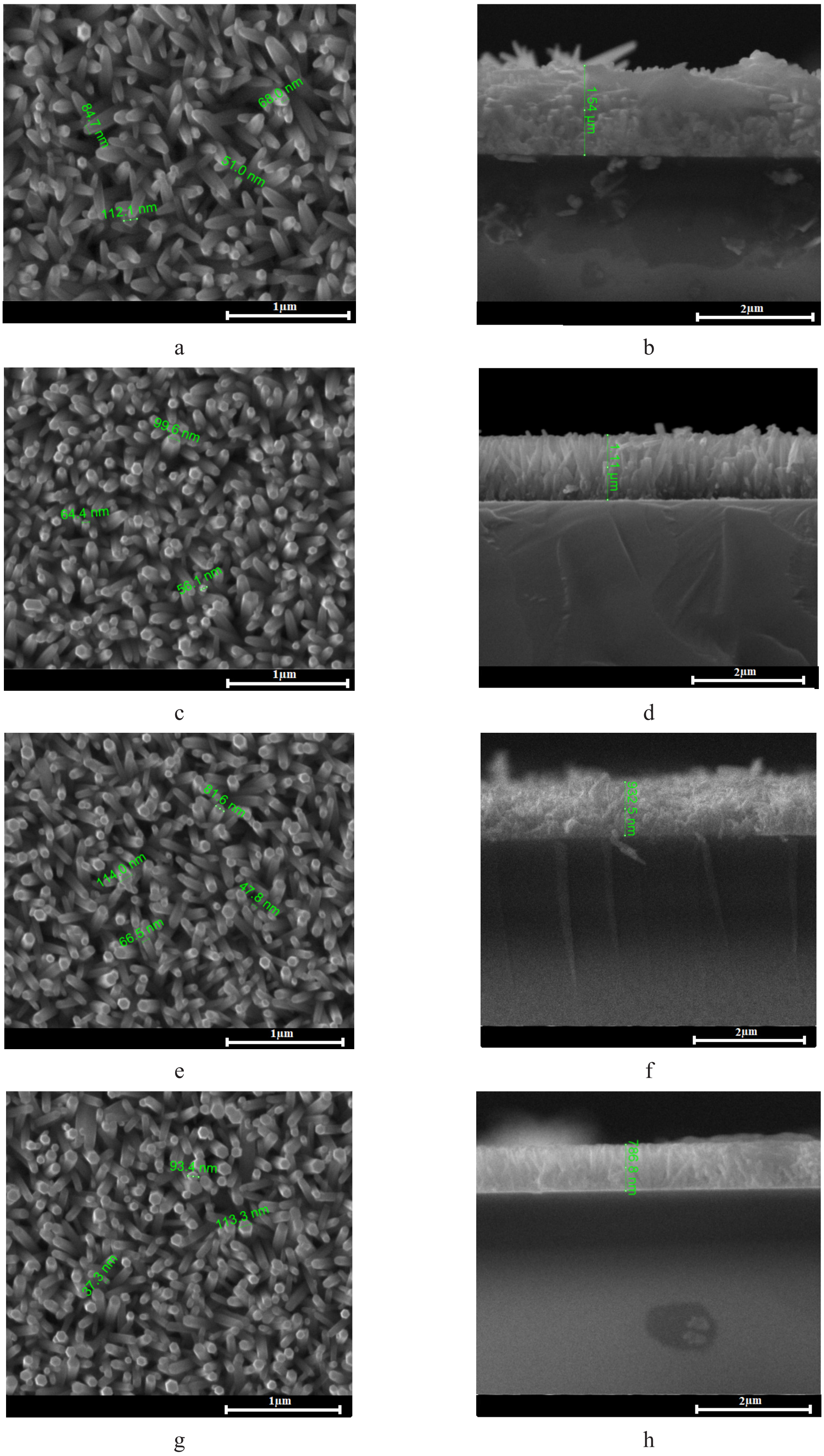

Figure 1 – Morphology of ZnO samples: a, b – initial; c, d – subjected to thermal annealing in a muffle furnace at a temperature of 450 °C for one hour; e, f – treated in hydrogen plasma with preliminary annealing in air; g, h – treated in hydrogen plasma

Table 1 – Physicochemical properties of ZnO nanorods

Sample	FESEM		Length/thickness, l/d	Cell Options, Å		E_g, eV
	Thickness d, nm	Length l, nm		a	c	
Initial	80±30	1540±10	19.25	3.246	5.201	3.125
AT samples	78±20	1100±10	14.1	3.245	5.201	3.15
A+PT-samples	77±20	933±20	12.1	3.246	5.206	3.2
PT samples	78±20	787±10	10.1	3.247	5.204	3.25

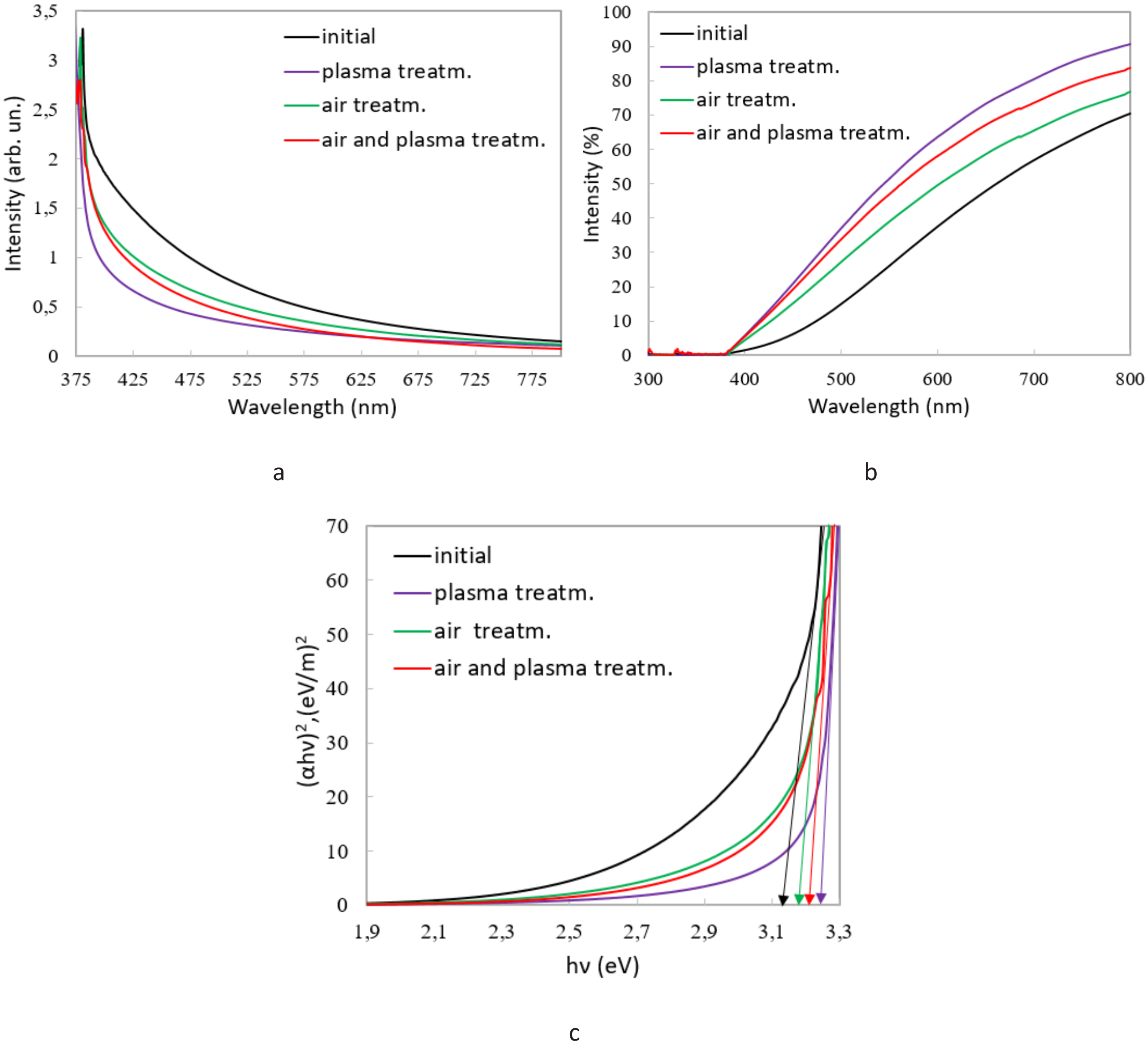

Figure 2 – Optical properties of ZnO films obtained by chemical deposition: (a) absorption spectra, (b) transmission spectra, (c) Tauc Plot diagram

The optical absorption spectra near the band gap of the sample annealed in air and also annealed in air followed by treatment in hydrogen plasma are similar. Samples treated in hydrogen plasma had the lowest absorption. This suggests that grown ZnO has numerous large number of electronic levels that are involved in light absorption, and the optical activity of these levels can be passivated by H-treatment. The highest absorption was noted for the original samples. It was found that the optical band gap is Eg = 3.125 eV for the original samples, 3.15 eV for the samples subjected to thermal annealing, 3.2 eV for the samples annealed in air followed by treatment in hydrogen plasma, 3.25 eV for samples treated with hydrogen plasma only (Table 1).

The XRD measurements were carried out under the same conditions. The diffraction peaks present indicate the hexagonal structure of the wurtzite of all samples under study. An analysis of the diffraction patterns showed a high crystallinity of all samples with a predominant (002) orientation with a slight difference in the intensity of the diffraction peaks. No significant effect of treatments on the structural properties of the samples was noted. The cell parameters of all samples are given in Table 1. Figure 3 shows the X-ray diffraction pattern of the original ZnO sample.

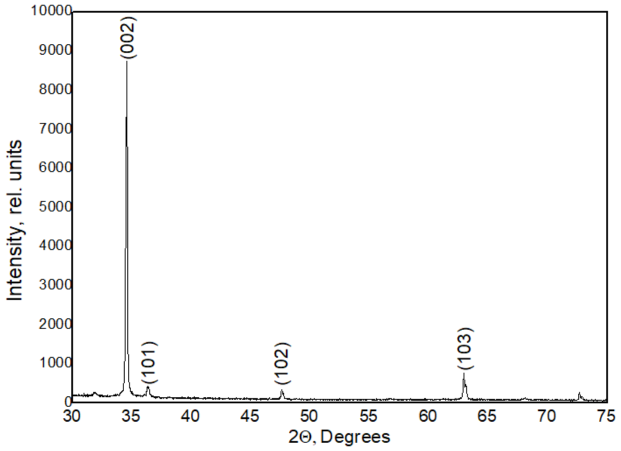

Figure 3 – Diffractogram of the initial ZnO sample

The photoluminescence spectra of ZnO samples synthesized by chemical solution deposition were studied (Figure 4). The photoluminescence spectra were measured at room temperature under excitation with light with a wavelength of 300 nm. As can be seen from Figure 4, immediately after synthesis the PL spectra show mainly an impurity band with a maximum at ~620 nm, and the intrinsic PL band almost does not appear. After annealing in air for an hour the maximum of the impurity PL band shifts by ~560 nm. Plasma treatment leads to a change in the ratio of the intensities of intrinsic and impurity photoluminescence bands. Preliminary annealing in the atmosphere followed by plasma treatment promotes a sharp increase in the intrinsic PL band.

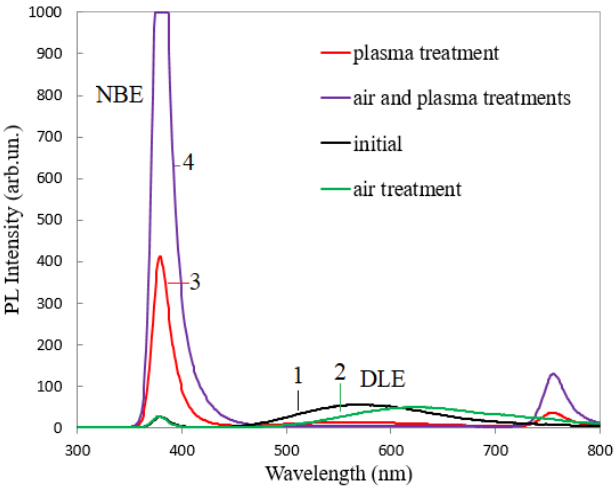

Figure 4 – Photoluminescence spectra of ZnO samples: 1. initial; 2. thermally annealed in a muffle furnace at 450°C for one hour; 3. treated in hydrogen plasma; 4. treated in hydrogen plasma with pre-annealing in air

A difference was noted in the photoluminescence spectra of the initial samples and after treatments [24]. The DLE band, which in the original samples had approximately the same intensity as the NBE band (Figure 4, spectra 1, 2), was completely passivated after treatment in hydrogen plasma (Figure 4, spectra 3, 4). The intensity of the NBE band in PT samples increased after treatment in hydrogen plasma (Figure 4, spectrum 3) by ~17 times compared to the initial spectrum (Figure 4, spectrum 1). An increase in the PL intensity may be associated with the passivation of recombination centers on the surface and in the bulk, the introduction of shallow donors, and others. For example, specific chemisorbed oxygen and various radicals obtained during synthesis are present on the surface of ZnO, which significantly effect on the surface recombination and can be passivated hydrogen [25].

Samples annealed at 450°C followed by treatment in hydrogen plasma showed an increase in NBE intensity by a factor of ~65 compared to the initial PL spectrum (Figure 4). This increase can be explained by a change in the structure of surface defects during thermal annealing, since it is known that the photoluminescent properties of nano- and microcrystalline ZnO are largely determined by surface effects [26]. It is known that the adsorption of oxygen forms causes the quenching of UV radiation of ZnO nanoparticles and the restoration of visible radiation [27].

3 Conclusions

The optical, structural, and photoluminescent properties of samples consisting of zinc oxide nanorods vertically oriented with respect to the substrate, synthesized by chemical solution deposition, initial, subjected to thermal annealing in a muffle furnace at a temperature of 450 °C for one hour, treated in hydrogen plasma, as well as processed in hydrogen plasma with preliminary annealing in air, were compared. It is shown that samples processed in hydrogen plasma had the lowest absorption coefficient, and the initial ZnO samples had the highest. The optical band gap for initial samples was 3.125 eV, 3.15 eV for samples subjected to thermal annealing, 3.2 eV for samples annealed in air followed by treatment in hydrogen plasma, 3.25 eV for samples processed only with hydrogen plasma. It is noted that the synthesized ZnO samples subjected to thermal annealing followed by treatment in hydrogen plasma had the highest photoluminescence intensity.

Acknowledgments

This research has been funded by the Science Committee of the Ministry of Education and Science of the Republic of Kazakhstan (Grant No. AP08856173).

References

1. R. Sauvik, Md. Ahmaruzzaman. ZnO nanostructured materials and their potential applications: progress, challenges and perspectives // J. Nanoscale Adv. – 2022. – Vol.4. – P.1868-1925. https://doi.org/10.1039/D1NA00880C
2. P. Hönicke, Y. Kayser, K.V. Nikolaev, V. Soltwisch, et. al. Simultaneous dimensional and analytical characterization of ordered nanostructures // J. Small. – 2022. – Vol. 18. – P. 2105776. https://doi.org/10.1002/smll.202105776
3. U. Wajid, Kh. Muhammad, A. Tariq, A. Muhammad, M. Hafiz, R. Naser. Synthesis, characterization and application of ZnO nanoparticles for improved growth and Zn biofortification in maize // J. Archives of Agronomy and Soil Science. -2021. –Vol. 67(9). – P. 1164-1176. https://doi.org/10.1080/03650340.2020.1782893
4. P.K. Aspoukeh, A.A. Barzinjy, S.M. Hamad. Synthesis, properties and uses of ZnO nanorods: a mini review // J. Int Nano Lett. – 2022. – Vol. 12. – P. 153 – 168. https://doi.org/10.1007/s40089-021-00349-7
5. N. B. Raj, N. T. Gowda, O. S. Pooja, B. Purushotham, M. R. A. Kumar, S. K. Sukrutha, C.R Ravikumar., H.P. Nagaswarupa, H.C. AnandaMurty, S. B. Boppana. Harnessing ZnO nanoparticles for antimicrobial and photocatalytic activities // Journal of Photochemistry and Photobiology. – 2021. – Vol. 6 – P. 100021. https://doi.org/10.1016/j.jpap.2021.100021
6. M. Carofiglio, S. Barui, V. Cauda, M. Laurenti. Doped zinc oxide nanoparticles: Synthesis, characterization and potential use in nanomedicine //J. Applied Sciences. – 2020. – Vol. 10 (15) – P. 5194. https://doi.org/10.3390/app10155194
7. S. Chu, G. Wang, W. Zhou. Electrically pumped waveguide lasing from ZnO nanowires // J. Nature Nanotechnology. – 2011. – Vol. 6 (8). – P. 506–510. https://doi.org/10.1038/nnano.2011.97
8. R. Macaluso, G. Lullo, I. Crupi, D. Sciré, F. Caruso, E. Feltin, M. Mosca. Progress in violet light-emitting diodes based on ZnO/GaN heterojunction // J. Electronics. – 2020. – Vol. 9(6). – P.991. https://doi.org/10.3390/electronics9060991
9. S. Shahzad, S. Javed, M. Usman. A Review on synthesis and optoelectronic applications of nanostructured ZnO // J. Front. Mater. – 2021. – Vol. 8. – P. 613825. https://doi.org/10.3389/fmats.2021.613825
10. A. R. Prasad, L. Williams, J. Garvasis, K. O. Shamsheera, S. M. Basheer, M. Kuruvilla, A. Joseph. Applications of phytogenic ZnO nanoparticles: A review on recent advancements // Journal of Molecular Liquids. – 2021. – Vol. 331 (6). – P. 115805. https://doi.org/10.1016/j.molliq.2021.115805
11. Zh. Zheng, K. Liu, X. Chen, B. Qiao, H. Ma, D. Liu, L. Liu, D. Shen. High-performance flexible UV photodetector based on self-supporting ZnO nano-networks fabricated by substrate-free chemical vapor deposition // J. *Nanotechnology*. – 2021. –Vol. 32(47). – P.475201. https://doi.org/10.1088/1361-6528/ac1bda
12. B. Cheng, J. Xu, Zh. Ouyang, C. Xie, X. Su, Y. Xiao, Sh. Lei. Individual ZnO nanowires for photodetectors with wide response range from solar-blind ultraviolet to near-infrared modulated by bias voltage and illumination intensity // J. Optics Express. – 2013. – Vol. 21 (24). – P. 29719-2973. https://doi.org/10.1364/OE.21.029719

13. N.K. Rajendran, B.P. George, N.N. Houreld, H. Abrahamse. Synthesis of zinc oxide nanoparticles using rubus fairholmianus root extract and their activity against pathogenic bacteria // J. Molecules. – 2021. – Vol. 26. – P. 3029. https://doi.org/10.3390/molecules26103029

14. A. Spoial, C.-I. Ilie, R.-D. Trus, O.-C. Oprea,, V.-A. Surdu, B.S. Vasile, A. Ficai, D. Ficai, E. Andronescu, L.-M. Dit. Zinc oxide nanoparticles for water purification // J. Materials. – 2021. – Vol. 14. – P. 4747. https://doi.org/10.3390/ma14164747

15. S. M. Faraz, S. R. Jafri, H. Khan, Q. Wahab, O. Nur. Effect of annealing temperature on the interface state density of n-ZnO nanorod/p-Si heterojunction diodes // J. Open Physics. – 2021. -Vol. 19(1). – P. 467-476. https://doi.org/10.1515/phys-2021-0053

16. S. Dhara, P. K. Giri. Enhanced UV photosensitivity from rapid thermal annealed vertically aligned ZnO nanowires // J. Nanoscale Rres. Lett. – 2011. – Vol. 6(1). – P 1-8. https://doi.org/10.1186/1556-276X-6-504

17. K. A. Abdullin, G. Cicero, L. V. Gritsenko, S. E. Kumekov, A. A. Markhabaeva. Effect of annealing and hydrogen plasma treatment on the luminescence and persistent photoconductivity of polycrystalline ZnO films // Journal of Applied Physics. -2017. – Vol. 121(24). – P. 245303. https://doi.org/10.1063/1.4989826

18. I. Lorite, J. Wasik, T. Michalsky, R. Schmidt-Grund, P. Esquinazi. Hydrogen influence on the electrical and optical properties of ZnO thin films grown under different atmospheres // J. Thin Solid Films. – 2014. –Vol. 556. – P.18-22. https://doi.org/10.1016/j.tsf.2013.12.057

19. J. Han, A. Abliz, D. Wan. Impact of hydrogen plasma treatment on the electrical performances of ZnO thin-film transistors // Chinese Journal of Physics. – 2022. – Vol. 77. – P. 327-334. https://doi.org/10.1016/j.cjph.2022.03.005

20. L. Wang, Y. Jia, Y. Wang, Sh. Zang, Sh. Wei, J. Li, X. Zhang. Defect passivation of low-temperature processed ZnO electron transport layer with polyethylenimine for PbS quantum dot photovoltaics // J. ACS Appl. Energy Mater. – 2019. – Vol. 2(3). – P. 1695–1701. https://doi.org/10.1021/acsaem.8b01756

21. R. Crapanzano, I. Villa, S. Mostoni, M. D'Arienzo, B. Di Credico, M. Fasoli, R. Scotti, A. Vedda. Morphology related defectiveness in ZnO luminescence: From bulk to nano-size // Nanomaterials. – 2020. – Vol. 10. – P. 1983. https://doi.org/10.3390/nano10101983

22. J. Rodrigues, T. Holz, R. F. Allah, D. Gonzalez, T. Ben, M. R. Correia, T. Monteiro, F. M. Costa. Effect of N_2 and H_2 plasma treatments on band edge emission of ZnO microrods // J. Sci. Rep. – 2015. –V. 5. – P. 10783. https://doi.org/10.1038/srep10783

23. I.V. Tudose, P. Horvath, P. Horvath, M. Suchea, M. Suchea. Correlation of ZnO thin film surface properties with conductivity // J. Applied Physics A. – 2007. – Vol. 89(1). – P.57-61. https://doi.org/10.1007/s00339-007-4036-3

24. R. A. Kh. Abdullin, M. T. Gabdullin, S. K. Zhumagulov, G. A. Ismailova, L.V. Gritsenko, M. Mirzaeian, Y. Y. Kedruk. Stabilization of the surface of ZnO films and elimination of the aging effect // Materials. -2021. – V. 14 (21). – P. 6535. https://doi.org/10.3390/ma14216535

25. R. Gurwitz, R. Cohen, I. Shalish. Interaction of light with the ZnO surface: Photon induced oxygen "breathing," oxygen vacancies, persistent photoconductivity, and persistent photovoltage // J. Appl. Phys. – 2014. – Vol. 115. –P. 033701. https://doi.org/10.1063/1.4861413

26. Y. Ma, T. Choi, S.H. Cheung, Y. Cheng, X. Xu, Y. Xie, H. Li, M. Li, H. Luo, W. Zhang. Charge transfer induced photoluminescence in ZnO // J. Nanoparticles. Nanoscale. – 2019. Vol. 11. – P. 8736–8743. https://doi.org/10.1039/C9NR02020A

27. D.S. Bohle, C.J. Spina. The relationship of oxygen binding and peroxide sites and the fluorescent properties of zinc oxide semiconductor nanocrystals // J. Am. Chem. Soc. -2007. –Vol. 129. – P. 12380–12381. https://doi.org/10.1021/ja0747223

Funded by Al-Farabi KazNU

IRSTI 44.01.05 https://doi.org/10.26577/phst.2022.v9.i2.03

Capacitive electrodes based on a combination of activated carbon and graphene

Sh. Nurbolat[1,2*], M. Gabdullin[3], Zh. Kalkozova[2], M. Mirzaeian[4] and Kh. Abdullin[2]

[1]Almaty University of Power Engineering and Telecommunication, Almaty, Kazakhstan
[2]Al-Farabi Kazakh National University, Almaty, Kazakhstan
[3]Kazakh-British Technical University, Almaty, Kazakhstan
[4]School of Computing, Engineering and Physical Sciences, University of the West of Scotland, Paisley, UK
*e-mail: shyryn0709@gmail.com

(Received 27 September 2022; received in revised form 5 December; accepted 24 December 2022)

As an important element of energy storage systems, Supercapacitors are energy storage devices with high power density. The optimal materials and designs for supercapacitors are currently being studied very intensively, and despite many years of research in this area, the development of electrode materials with optimal properties problem remains very relevant. In order to ensure their high efficiency, along with a high specific capacitance, it is important to lower their series resistance. Carbon materials with a high specific surface area have been widely used as potential electrode material for supercapacitors, however their insufficiently low electrical resistivity limits the energy and power density of the device. Therefore, for optimizing the energy storage and power capability of supercapacitors, development of composite materials electrodes with optimized properties and low electric resistance is crucial. In this article, composite electrodes based on a combination of activated carbon and graphene are obtained and their properties are investigated. The capacitive performance of the composite electrodes is tested in an electrochemical cell and their advantage for lowering the electrical resistance of the device is shown.

Keywords: supercapacitors, energy storage, electrodes, graphene, carbon.
PACS number: 81.05.ue

1 Introduction

Renewable energy is rapidly developing at the present time. Various types of renewable green energy, such as solar photovoltaics, tidal and wind energies, show intermittent activity that depends on the time of day, season and weather. Therefore, energy storage and accumulation devices that dampen surges in the supply and consumption of electricity and ensure the security of the supply are necessary for the creation of modern energy systems and our future energy demands. An important role in such energy storage and accumulation systems is played by electrochemical devices, which are also widely used to power different electrical systems such as electric vehicles, electric autonomous devices, and various electrical gadgets [1-2].

Batteries and electrochemical capacitors are at the forefront of electrical energy storage technologies. Electrochemical batteries, in particular lithium-ion batteries are technologies with high energy density and maximum specific energy storage capacity. While supercapacitors, which are the most important element of energy storage and accumulation systems, have the highest specific power. In electrochemical double layer capacitors (also called supercapacitors), energy is stored in the form of opposite electric charges on electrodes separated by a separator creating an electric double layer at the electrode/electrolyte interface [3-5]. They store more energy than ordinary capacitors and since charge carriers on a double charged layer do not cross the electrode-electrolyte interface during charge-discharge processes, supercapacitors have very high stability during cyclic operation with a very fast accumulation and release of charge during charge/discharge. The specific capacitance of the device is determined by the amount of charge that can be accumulated on the electrode surface, and therefore the specific surface area of electrode is an important factor that determines the capacitance [6].

Supercapacitor technology has been intensively developed due to its high practical importance. However, despite of a significant research in the development of high energy supercapacitors in recent years, their performance to address the gap in the energy/power requirements of energy systems is not achieved yet [7-9].

Carbon-based nanostructured materials are very promising for the manufacture of electrochemical supercapacitors due to their significantly high specific surface area. Supercapacitors based on different carbon materials, such as activated carbon [10], graphene [11], reduced graphene oxide composites [12], carbon nanotubes [13–15], composites of graphene and carbon nanotubes [16], various carbon particles with developed morphology and high crystallinity, mesoporous carbon [17], doped porous carbon [18] with low electrical resistance are used as electrode materials for supercapacitors to improve the performance of their by lowering the electrical resistance of the electrodes. Li et al., and Bukhari et al., have also used carbon matrix to create a hybrid electrode material for supercapacitor electrodes [19, 20].

In order to improve the charge/discharge rate capability of the device by lowering the electric resistance of the electrodes and at the same time, maintaining its capacitance high by keeping the specific surface area of the carbon used as electroactive material, the fabrication of electrodes from carbon matrix composites is of high practical importance. This paper presents the results on the development of asymmetric supercapacitors using capacitive composite electrodes obtained from activated carbon and reduced graphene oxide.

2 Experiment details

The electrodes were made from activated carbon powder and graphene oxide. Commercial activated carbon had a surface area of 1800 m^2g^{-1} according to the manufacturer's certificate. The surface area of the activated carbon used in this work was measured by the BET method (Brunauer-Emmett-Teller Method) and amounted to 1718 m^2g^{-1}. Graphene oxide (GO) was obtained by a modified Hummers method [21]. The reduction of graphene oxide was carried out by annealing in vacuum at temperatures from 110°C to 500°C and irradiation with UV radiation. To obtain reduced graphene oxide (rGO) by irradiation with UV light, a DRT 400 mercury lamp fed was used. The lamp was fixed in a horizontal position 10 cm above the sample. The reduction of GO was monitored by XRD using a MiniFlex Rigaku diffractometer and by measuring the electrical resistance of GO layers. The GO layers were created by depositing a thin layer of an aqueous GO suspension on a 76×26 mm^2 glass substrate, followed by drying at ~100°C under atmospheric conditions. Then the glass substrate was cut into samples of the required size for further studies. The electrical resistance of the GO layers was measured with a Keithley Instruments 6517B electrometer. The morphology of the samples was studied using a Quanta 200i 3D scanning electron microscope (SEM).

Electrode were fabricated using ~80 wt% mixture of activated carbon and rGO as active material, ~10 wt% carbon black as conductivity enhancer and ~10% polyvinylidene fluoride (PVDF) as binder. Acetone was used as a PVDF solvent. Nickel foam was used as conductive substrates for capacitive electrodes. A uniform paste was produced by mixing the electrode constituents in acetone for 3 h under magnetic stirring. The paste was then applied on nickel foam substrate. A two-electrode cell was then constructed using the fabricated electrodes with paper filter as a separator between them where an electrolyte comprising a KOH solution (3.5M) was added to the separator. The electrochemical performance of the cell was measured using an Elins P-40X-FRA-24M potentiostat.

3 Results and discussion

Figures 1a and 1b show SEM images of the original graphene oxide GO and the reduced graphene oxide rGO. SEM images of activated carbon (AC) used in this work and carbon black, which serves to fill the voids between AC particles, are also shown in Figures 1c and 1d, respectively.

For XRD analysis and electrical measurements, GO films were formed on glass substrates. A volume of an aqueous GO emulsion of about 100 µL per 1 cm^2 was applied with a micropipette onto a previously degreased glass substrate. After the emulsion dried, a film about 5 microns thick was formed. XRD patterns of the GO sample (Figure 2, curve 1) indicate a large interplanar spacing between graphene GO planes and a high degree of oxidation of graphite obtained by the Hummers method. Annealing in vacuum at temperatures of 110°C (curve 2) and 500°C (curve 3) leads to a decrease in the distance between the graphene planes, which is an indication of the reduction of GO under vacuum. It should be noted that the decrease in the distance between graphene planes occurs very slowly at annealing temperatures from 100 to ~140°C, and upon annealing between 140 and 150°C, the distance between graphene planes is abruptly restored to values corresponding to graphite. This abrupt reduction corresponds to the desorption of oxidizing radicals intercalated into graphite and the release of gases [20]. In this case, GO films lose their mechanical strength. For applied purposes, it is important to obtain strong and conductive films; for this, it is necessary to use the control of the electrical properties of films in the process of reduction.

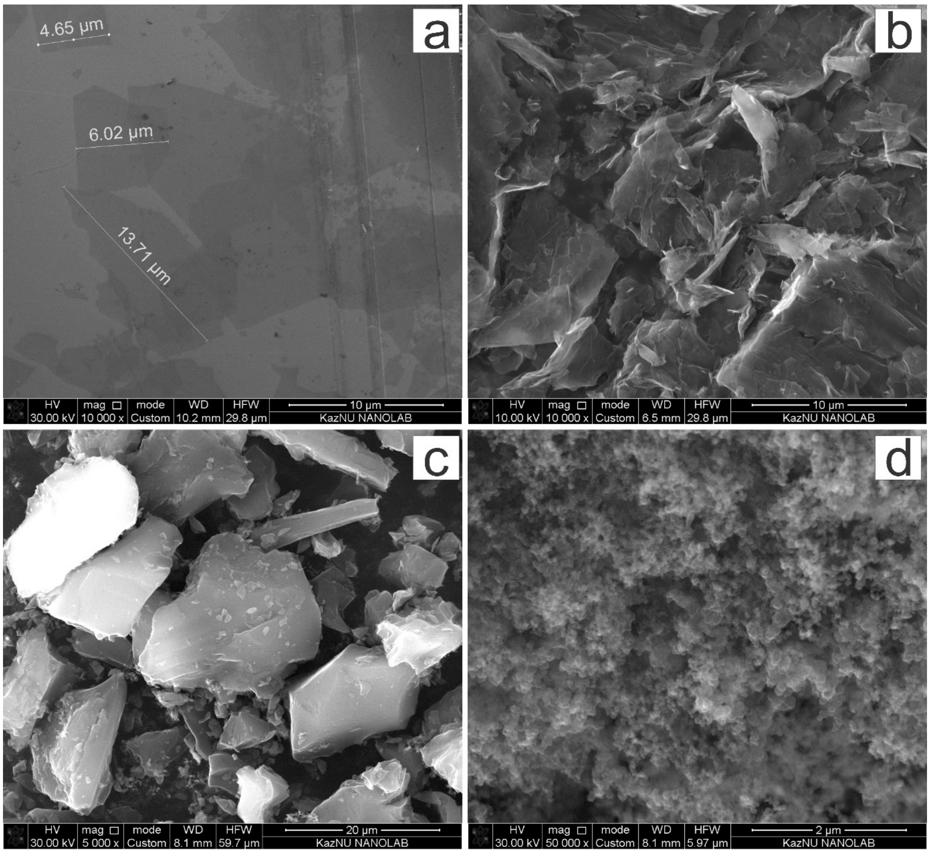

Figure 1 – SEM images of the carbon materials: (a) GO film on silicon substrate, (b) rGO, (c) activated carbon, and (d) carbon black

The original graphene oxide creates strong dielectric films on the substrate, by measuring the electrical resistance of the films, it is possible to monitor the GO reduction process at low (100–110°C) temperatures with high sensitivity and determine the optimal reduction modes. To reduce GO, we used two methods: vacuum annealing and UV irradiation with a mercury lamp; the electrical resistance of the films was determined by the two-probe method.

It was found that vacuum annealing is much more efficient than annealing in air. For example, GO films remained dielectric after annealing in air at 110°C for 60 minutes, and after vacuum annealing at the same temperature, the electrical resistance dropped to 8×10^8 Ohm. It is interesting to note that an increase in the duration of vacuum annealing of the GO film did not lead to a further drop in its electrical resistance. It can be concluded that the drop in resistance of the film is presumably due to both thermal action, which causes desorption of a part of oxidizing radicals, and film compaction.

Another method used for reducing GO was UV light irradiation. Figure 3 shows the result of various combinations of exposure to vacuum annealing at 110°C/60 minutes and exposure to light from a mercury lamp. Curve 1 corresponds to the resistance of samples that were first annealed in vacuum at 110°C and then subjected to UV irradiation for up to 200 minutes. It can be seen that an increase in the time of UV irradiation leads to a progressive decrease in the electrical resistance of GO film.

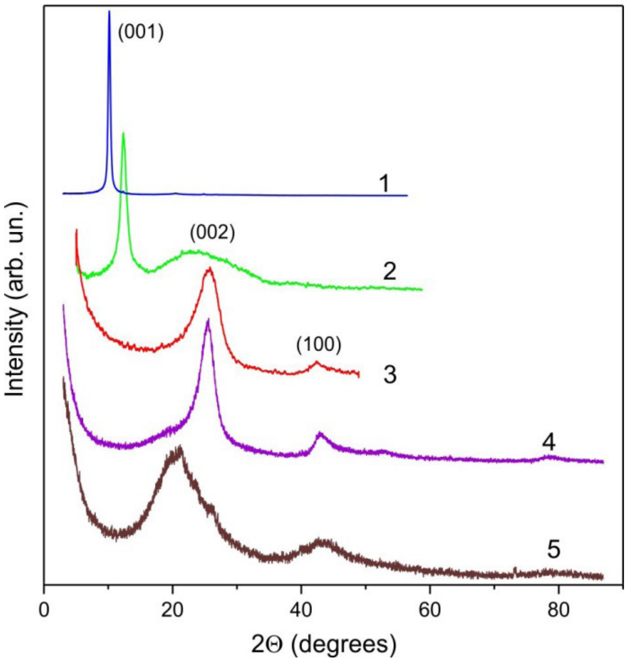

Figure 2 – XRD patterns of the carbon materials used: original GO (1), GO after vacuum annealing at 110°C (2) and 500°C (3), carbon black (4) and activated carbon (5)

It was found that when the sequence of operations is reversed, i.e., first irradiating the GO film with UV and then annealing it in vacuum at 110°C/60 minutes, the electrical resistance of the film decreases by approximately 3 orders of magnitude, as shown in Figure 3, curve 2. Moreover, if UV irradiation is carried out after vacuum annealing, then the electrical resistance of the films almost does not decrease (curve 3 in Figure 3). It can be concluded that vacuum treatment densifies the GO structure, which hinders the release of desorbing oxidative spices from graphene oxide; therefore, such treatment should be applied at the final stage of obtaining rGO.

Despite the drop in the electrical resistance of rGO by many orders of magnitude compared to the original GO, the XRD data show insignificant but regular changes in the structure of rGO relative to GO, as can be seen from Figure 4. The intensity decreases, while the relative intensity of the (002) reflection increases.

The capacitive electrodes were made of AC activated carbon with rGO additives, acetylene black as a filler, polyvinylidene fluoride PVDF polymer as a reinforcing material, nickel foam serving as a substrate. In order to reduce the series resistance of the electrodes, rGO, which has a higher electrical conductivity, was added to the activated carbon. The resulting mixture was applied to a nickel foil substrate with an area of 1×1 cm^2, which was thoroughly degreased beforehand. Two electrodes with the same mass were made in pairs.

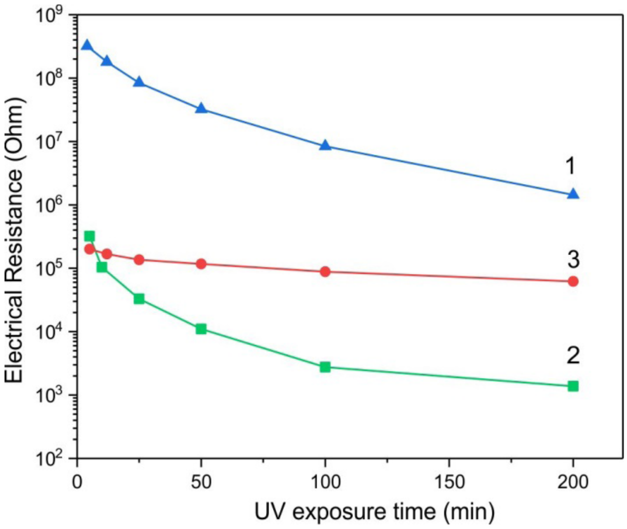

Figure 3 – Measurement of the electrical resistance of GO layers depending on the time of exposure to UV light: 1 – annealing in vacuum at 110°C followed by UV irradiation, 2 – UV irradiation followed by annealing at 110°C in vacuum, 3 – short-term (5 minutes) UV irradiation with subsequent annealing at 110°C in vacuum, followed by repeated UV irradiation

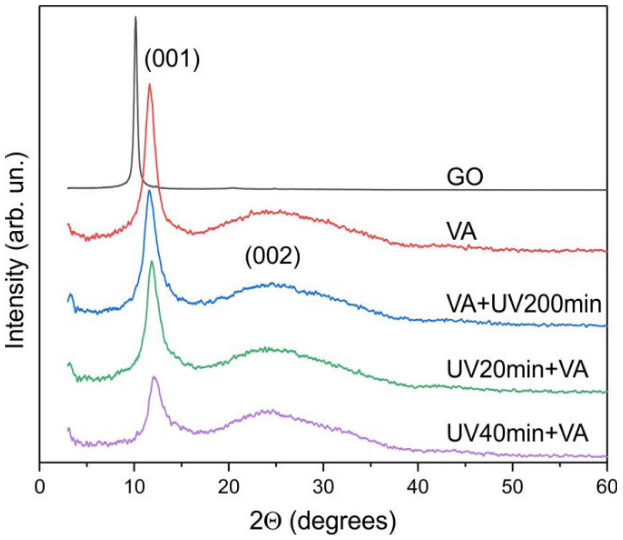

Figure 4 – XRD patterns of the graphene oxide: GO – as-synthisized GO, VA – vacuum annealing, VA+UV200min – vacuum annealing followed by irradiation with UV light for 200 min, UV20min+VA – irradiation with UV light for 20 min followed by vacuum annealing, UV40min+VA – irradiation with UV light for 40 min followed by vacuum annealing

Figure 5(a) shows the cyclic voltammograms of activated carbon (AC) and a mixture of AC : rGO = 10 : 1 (AC+Graphene) used as electroactive material with 3.5 M KOH electrolyte in the electrochemical capacitor measured at a sweep rate of 10 mV s^{-1}. It can be seen that the shape of the CV curves is close to rectangular, redox current peaks disappear, which corresponds to the purity density of the materials used. At the same time, for the AC + rGO capacitor, the CV curves are more rectangular than those for the AC capacitor. This is due to their lower series resistance of the AC-rGO mixture as shown before.

Galvanostatic charge-discharge (GCD) curves normalized to a current of 1 A g^{-1} (Figure 5 b) show that the capacitances of the AC and AC+rGO mixture capacitors are close, but the AC+rGO electrodes show less series resistance because the potential jump at the change in current direction is less than that of AC electrodes and correspond to a resistance of 6 ohms versus 10 ohms for AC electrodes.

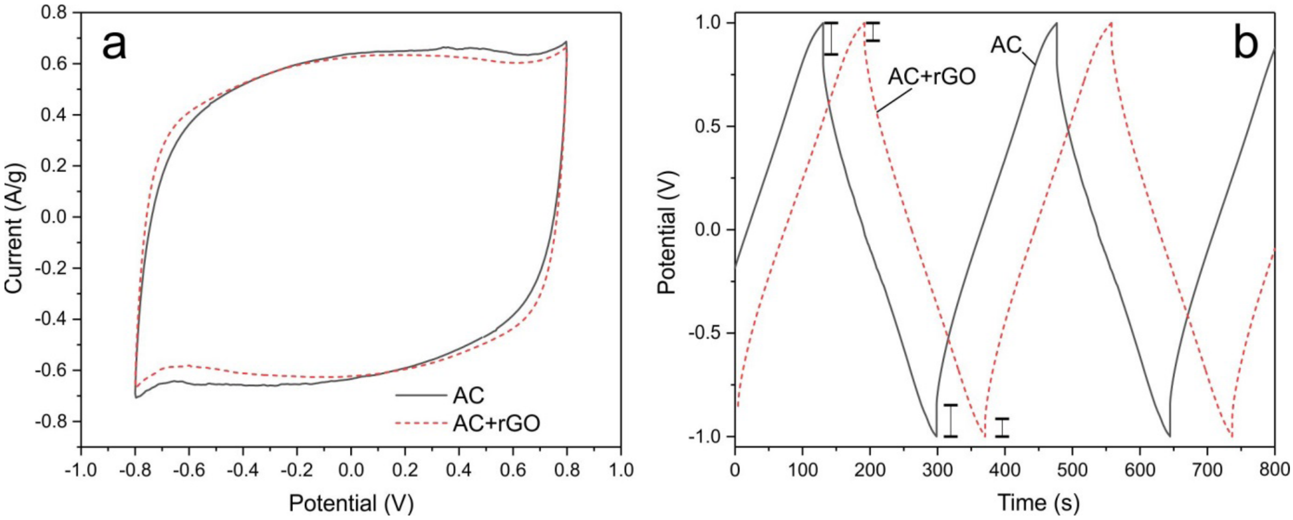

Figure 5 – Cyclic voltammograms of capacitors using activated carbon (AC) and a mixture of AC : rGO = 10 : 1 (AC+rGO) as electrode material (a); GCD curves of activated carbon (AC) and mixture (AC+rGO) capacitors at 1 Ag^{-1} current (b)

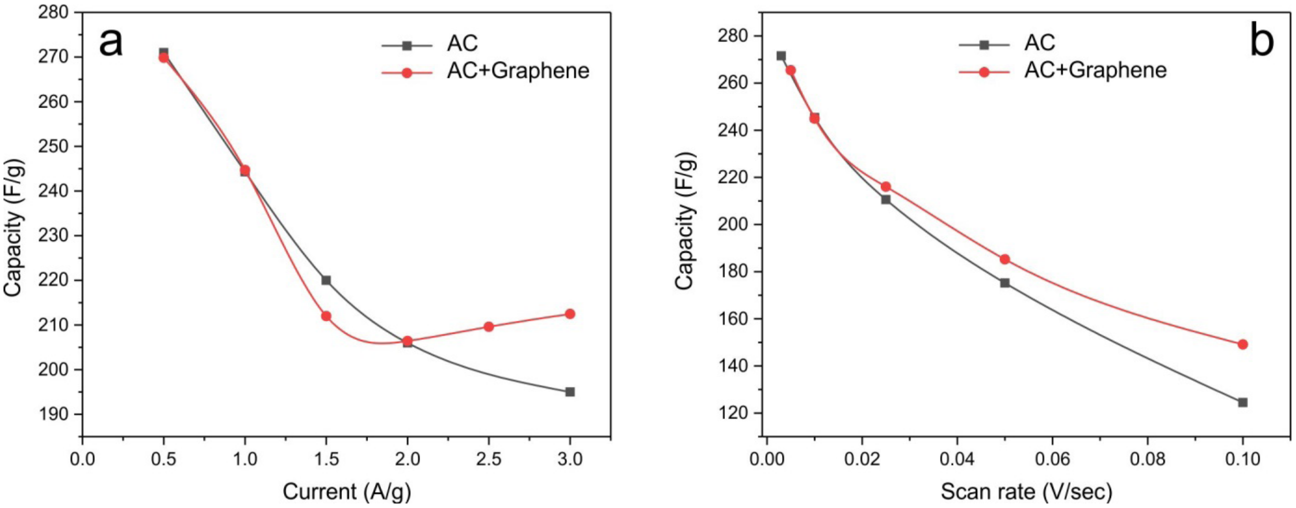

Figure 6 – The dependence of the capacitance of capacitors obtained from the current-voltage curves (a) and the galvanostatic charge-discharge curves (b)

Figure 6 shows graphs of capacitor capacitance changes with increasing galvanostatic charge-discharge GCD (Figure 6a) and increasing scan rate when measuring CV cyclic voltammograms (Figure 6b). It can be seen that the addition of graphene slows down the capacitance drop at high sweep rates for the CV curves and at high currents for the GCD curves. Thus, the presence of graphene improves performance in the high current region, that is, in the working region of supercapacitors, by improving the electrical characteristics of the material.

The specific capacitance of carbon capacitors also decreases with an increase in the mass of the electrode load, and this is a significant technical problem. The CV curves measured at low sweep rates for electrode loads in the range of 10 to 100 mg cm^{-2} are almost the same, however, as the potential scan rate increases, the electrodes with higher load masses show faster capacitance drops much faster for high load masses.

4 Conclusions

The drop in specific capacitance is due to an increase in the thickness of the carbon layer and, accordingly, an increase in the electrical resistance of the electrode. Series electrical resistance also limits the power of the capacitor. In thinner electrodes, the charge distribution in the electrode layer is kept the same and the contribution of the entire electrode to the capacitance is uniform, however with increase in the electrode's thickness, the charge distribution in the electrode depth varies and the contribution to the capacitance of regions remote from the surface in contact with the metal current collector decreases, and therefore in order to maintain their capacitive contribution, long charge-discharge times are required. This could be considered as one of the main advantages of supercapacitors which allows maintaining release of energy in different time scales to respond to the energy demands in a range of delivery times where, high developed powers, are leveled. The creation of a mixture of activated carbon and graphene with different ratios could contributes to a decrease in electrical resistance improving the energy/power response characteristics of capacitors in the energy continuum demands.

Acknowledgements

This research was funded by Ministry of Education and Science of the Republic of Kazakhstan, grant number AP09259253.

References

1. Zh. Jingyuan, B. Andrew. Review on supercapacitors: Technologies and performance evaluation // Journal of Energy Chemistry. – 2021. – Vol. 59. – P.276–291. http://doi:10.1016/j.jechem.2020.11.013.
2. A. González, E. Goikolea, J. A. Barrena and R. Mysyk. Review on supercapacitors Technologies and material // Renewable and Sustainable Energy Reviews – 2016. – Vol. 17. – P. 1189–1206. http://dx.doi.org/10.1016/j.rser.2015.12.249.
3. P. Naskar, D. Kundu, A. Maiti, P. Chakraborty, B. Biswas, and A. Banerjee. Frontiers in Hybrid Ion Capacitors: A Review on Advanced Materials and Emerging Devices // ChemElectroChem. – 2021. – Vol. 36. – P.1393 –1429. http://doi.org/10.1002/celc.202100029.
4. M. E. Sahin, F. Blaabjerg, A. Sangwongwanich. A Comprehensive Review on Supercapacitor Applications and Developments // Energies – 2022. . – Vol. 15. – P. 674. https://doi.org/10.3390/en15030674.
5. S. Huang, X. Zhu, S. Sarkar, and Y. Zhao. Challenges and opportunities for supercapacitors // APL Mater. – 2019. – Vol. 7. – P. 100901. http://doi.org/10.1063/1.5116146.
6. G.A. Tafete, M.K. Abera, G. Thothadri. Review on nanocellulose-based materials for supercapacitors applications // J. Energy Storage. – 2022. – Vol. 48. – P. 103938. https://doi.org/10.1016/j.est.2021.103938
7. Y. Zhang, L. Cheng, L. Zhang, D. Yang, C. Du, L. Wan, J. Chen, M. Xie. Effect of conjugation level on the performance of porphyrin polymer based supercapacitors // J. Energy Storage. – 2022. – Vol. 34. – P. 102018. https://doi.org/10.1016/j.est.2020.102018
8. S. Faraji, F. N. Ani. The development supercapacitor from activated carbon by electroless plating—A review // Renewable and Sustainable Energy Review. – 2015. – Vol. 42. – P.823-834. https://doi.org/10.1016/j.rser.2014.10.068
9. S.Dhibar, S.Malik. Morphological Modulation of Conducting Polymer Nanocomposites with Nickel Cobaltite/Reduced Graphene Oxide and Their Subtle Effects on the Capacitive Behaviors // ACS Applied Materials & Interfaces. – 2020. – Vol. 15. – P. 54053-54067. https://doi.org/10.1021/acsami.0c14478
10. I.P. Prado, D.S. Torres, R.R.Rosas, E. Morallón and D. C.Amorós. Design of Activated Carbon/Activated Carbon Asymmetric Capacitors // Frontiers in Materials. – 2016. – Vol. 12. https://doi.org/10.3389/fmats.2016.00016

11. W. K. Chee, H. N. Lim, Z. Zainal, N. M. Huang, I. Harrison, Y. Andou. Flexible Graphene-Based Supercapacitors A Review // J. Phys. Chem. – 2016. – Vol. 19. – P. 4153−4172. https://doi.org/10.1021/acs.jpcc.5b10187.

12. M. Rapisarda, F. Marken, M Meo. Graphene oxide and starch gel as a hybrid binder for environmentally friendly high-performance supercapacitors // Communications Chemistry. – 2021. – Vol. 11. – P. 169. https://doi.org/10.1038/s42004-021-00604-0

13. Z.Lu, R.Raad, F.Safaei, J.Xi, Z.Liu, J.Foroughi. Carbon Nanotube Based Fiber Supercapacitor as Wearable Energy Storage // Frontiers in Materials. – 2019. – Vol. 14. https://doi.org/10.3389/fmats.2019.00138.

14. W. Liang, I. Zhitomirsky. Composite Ti3C2Tx-carbon nanotube electrodes with high active mass for supercapacitors // Open Ceramics. – 2021. – Vol. 4. – P. 100158. https://doi.org/10.1016/j.oceram.2021.100158.

15. S.Wang, Y.Liang, W.Zhuo, H.Lei, M.S. Javed, B.Liu, W.Mai. Freestanding polypyrrole/carbon nanotube electrodes with high mass loading for robust flexible supercapacitors // Materials Chemistry Frontiers. – 2021. – Vol. 5. – P. 1324–1329. https://doi.org/10.1039/d0qm00649a.

16. A. Aphale, K.Maisuria, M. Mahapatra, et al. Hybrid Electrodes by In-Situ Integration of Graphene and Carbon-Nanotubes in Polypyrrole for Supercapacitors // Sci Rep. – 2015. – Vol. 5. – P. 14445. https://doi.org/10.1038/srep14445.

17. S. Yuan, Q. Gao, C. Ke, T. Zuo, J. Hou, J. Zhang. Mesoporous Carbon Materials for Electrochemical Energy Storage and Conversion // ChemElectroChem. – 2021. – Vol. 9. https://doi.org/10.1002/celc.202101182.

18. K. Wei, F. Zhang, Y. Yang, B. Zhai, X. Wang, Y. Song. Oxygenated N-doped porous carbon derived from ammonium alginate: Facile synthesis and superior electrochemical performance for supercapacitor // Journal of Energy Storage. – 2022. – Vol. 51. – P. 104342. https://doi.org/10.1016/j.est.2022.104342.

19. Q.B. Le, T. Nguyen, H. Fei, C. Bubulinca. Electrochemical performance of composite electrodes based on rGO, Mn/Cu metal–organic frameworks, and PANI // Scientific Reports. – 2022. – Vol. 12. – P. 664. https://doi.org/10.1038/s41598-021-04409-y.

20. S. W. Bokhari, Y. Hao, A. H. Siddique, Y. Ma, M. Imtiaz, R. Butt, P. Hui, Yao Li, S. Zhu. Assembly of hybrid electrode rGO–CNC–MnO_2 for a high performance supercapacitor // Results in Materials. – 2019. – Vol. 5. – P.100007. https://doi.org/10.1016/j.rinma.2019.100007.

21. J. Chen, B. Yao, C. Li, G. Shi. An improved Hummers method for eco-friendly synthesis of graphene oxide // Carbon – 2013. – Vol. 4. – P. 225 – 229. https://doi.org/10.1016/j.carbon.2013.07.055

Funded by Al-Farabi KazNU

Physical Sciences and Technology. Vol. 9 (No. 3-4), 2022: 37-44

IRSTI 55.09.35 https://doi.org/10.26577/phst.2022.v9.i2.04

Study of the structure and properties of SiC ceramics

Al. Zhilkashinova, M. Abilev, D. Zhambakin,
As. Zhilkashinova* and A. Pavlov

Sarsen Amanzholov East Kazakhstan University, Ust-Kamenogorsk, Kazakhstan
*e-mail: asssel2462@mail.ru

(Received 10 August 2022; received in revised form 20 September; accepted 5 November 2022)

This paper presents the results of the entropy calculation of the equilibrium constants of chemical reactions at liquid-phase sintering of SiC ceramics with eutectic additives. The composition of the charge for sintering ceramics with nanoadditives forming the liquid phase was determined: MnO_{nano} 1.5 wt. % + Al_2O_{3nano} 2 wt.% + $SiC_{\mu m}$ 94 wt. % + $SiO_{2\mu m}$ 2.5 wt. %. Possible chemical reactions of liquid-phase sintering of ceramics at a temperature of 1800 °C in a weakly reducing CO medium were established. The values of the change in the Gibbs energy for all possible chemical reactions at a sintering temperature of 1800 °C were calculated by the method of entropy calculation of the equilibrium constants. The elements of the liquid phase and reinforcing additives were determined.The elements of the liquid phase and reinforcing additives were determined. The structure and properties of finished sintered ceramic samples were studied. Microstructural analysis of ceramics indicated its grain structure with an average grain size of ~10 μm. The main phase components of the ceramics based on silicon oxide were determined. It was found that the sample consists of three main phases: modification of the ring radical of silicate Si_3O_6, silicon dioxide SiO_2 and anorthoclase $(SiAl)O_4$.

Keywords: silicon carbide, nanoparticles, ceramics, structure, chemical reactions, liquid phase sintering.
PACS numbers: 61.05.C; 77.84.Dy; 61.66.Fn; 61.46.−w; 75.50.Tt.

1 Introduction

Rapid development of science and technology results in the need to create fundamentally new materials capable of operating under extreme conditions and increased mechanical loads. Such materials should be resistant to thermal effects, have high density and low porosity, and other features for thermally and mechanically loaded material [1, 2]. The most promising today are ceramic composite materials obtained using modern technologies and the achievements of science and technology [3, 4]. Composite materials are heterophase systems of two or more components, with the preservation of the individual properties of each individual component [5].

The main advantage of ceramic composite materials is a special mechanism of their destruction under the action of loads [6]. In order to increase the strength of the material, reinforcing components are added to the ceramic matrix [7, 8]. Thus, reinforcing components tend to increase fracture toughness by redirecting crack paths, or minimizing crack growth. Thus, the control of the creep of aluminum oxide at elevated temperatures is carried out by introducing other phases – mullite and zirconium dioxide [9].

One of the most difficult tasks in the synthesis of ceramics based on silicon carbide is the creation of temperature and other conditions for its sintering. Since the temperature of solid phase sintering of SiC ceramics is 2100 °C in a CO atmosphere, this technological process requires special high-tech thermal equipment [10, 11]. The introduction of reinforcing additives into the ceramics based on SiC, with a properly selected eutectic, makes it possible to reduce the sintering temperature to 1800 °C and below [12].

The choice of oxide binders for silicon carbide sintering was studied in [13], following the thermodynamic arguments, Al_2O_3, BeO, HfO_2 are the most stable and do not contribute to the decomposition of silicon carbide during sintering. Oxides of zirconium, calcium, magnesium, on the contrary, contribute to the dissociation of SiC into metal and carbon. Suzuki et al. [14] used aluminum oxide to densify silicon carbide. The samples were fired in an oxygen-free environment (an atmosphere of argon or helium with vapors of aluminum, silicon, and carbon is preferable, contributing to better compaction). Fuentes et al. [15] activated SiC sintering with additions of Al_2O_3, CaO, and C. The addition of free carbon in the system, reacting with the calcium aluminate phase, gave a liquid oxycarbide phase, which led to an increase in the density of the material up to 97-99%. Liquid-phase sintering of silicon carbide with Al_2O_3 and/or MgO binders in the temperature range of 1800-2000 °C leads to the appearance of a second phase, which usually lowers the mechanical properties of the material at high temperatures. Such a negative effect indicates the need to reduce the proportion of additives introduced. To reduce the sintering temperature of the samples, ultrafine powders of the initial components are used [16].

To obtain products from powders with nanoadditives, it is necessary to compact them. The main goal of this stage is to keep the grain size in the nano range and get a quality product with minimal defects. The most developed technologies for producing silicon carbide ceramic products are high vacuum pressing, pressure sintering, hot isostatic pressing, etc. [17-21].

Thus, the aim of this study is to develop the composition of the charge for sintering carbide ceramics with nanoadditives that form a liquid phase at a sintering temperature of 1800 °C in a weakly reducing CO atmosphere, as well as the study of the structure and properties of finished sintered ceramic samples.

2 Materials and methods

The microstructure and point elemental analysis of the samples were studied using a scanning electron microscope with a JSM-6390LV, 2007 energy-dispersive microanalysis attachment with a resolution of up to 3 nm in high vacuum.

The value of the apparent density was determined according to GOST 2409-95 “Refractories. Method for determining apparent density, open, total and closed porosity, water absorption”. The dried sample was weighed, evacuated, and saturated with a liquid that wets the sample but does not interact with it. Then the test sample was weighed in the saturating liquid and in air. Based on the weightings and the value of the true density of the material, the apparent density was calculated with an accuracy of ± 0.001%, open and total porosity, and water absorption – with an accuracy of ± 0.0001%.

The determination of the microhardness of the samples was carried out using the indentation method using the Vickers method. A diamond pyramid was used as an indenter; the pressure force was 500 N.

X-ray phase analysis of powders and samples was carried out using an X’PertPRO X-ray diffractometer (PANanalytical, 2005).

3 Results and discussion

In order to select reinforcing and liquid-phase additives for SiC ceramic sintering, it is necessary to select the optimal ratio, amount and calculate the eutectic of impurities promoting ceramic sintering at a temperature of 1800 °C in a weakly reducing CO atmosphere. The significant affinity of aluminum for oxygen, as well as the cubic lattice of the synthesized yttrium aluminum garnet, make it possible to prevent the carbidization of the complex oxide up to a temperature of 2040 °C [22-25]. Metals that form oxides of the cubic system have the highest affinity for oxygen. This suggested that yttrium oxide in the form of a complex compound with aluminum oxide, for example, yttrium-aluminum garnet, which has a cubic crystal lattice, may be resistant to carbidization above 1850 °C. Oxides thermodynamically allowed for use as additives are reduced by carbon: CaO – at 2050 °C, MgO – 2060 °C, $Al_2O_{3\_}$ 1980 °C. Since the melting point of nanosized particles of powders in comparison with the micron size of particles of the same substance decreases, then the maximum allowable temperature for the synthesis of ceramics by the method of liquid-phase sintering will be 1800-1850 °C.

Taking into account the analysis and review of literature data, the composition of the charge for sintering carbide ceramics with additives that form the liquid phase has been developed:

$$MnO_{nano}\ 1.5\ \text{wt. \%} + Al_2O_{3nano}\ 2\ \text{wt. \%} +$$
$$+SiC_{\mu m}\ 94\ \text{wt. \%} + SiO_{2\mu m}\ 2.5\ \text{wt. \%}.$$

In the process of liquid-phase sintering of ceramics of the specified composition, the following chemical reactions are possible:

$$2SiO_2 + SiC \rightarrow 3SiO + CO \quad (1)$$
$$Al_2O_3 + SiC \rightarrow SiO + Al_2O + CO \quad (2)$$
$$MnO + SiC \rightarrow Mn + SiO_2 + CO \quad (3)$$
$$Al_2O_3 + SiO_2 \rightarrow Al_2(SiO_3)_3\ (Al_2O_3SiO_2) \quad (4)$$
$$SiO_2 + 2SiC \rightarrow 3Si + 2CO \quad (5)$$
$$MnO + SiO_2 \rightarrow MnO_2 + SiO \quad (6)$$

During the sintering of ceramics in a weakly reducing CO environment, the possible chemical reactions are:

$$Al_2O_3 + CO \rightarrow Al + CO_2 \tag{7}$$

$$SiO_2 + CO \rightarrow SiO + CO_2 \tag{8}$$

$$SiC + CO \rightarrow SiO_2 + C \tag{9}$$

To determine the possibility of interaction of these elements during sintering, one can use a simplified calculation, the so-called entropy method for calculating equilibrium constants, based on the Gibbs-Helmholtz equation:

$$A = Q + T\frac{dA}{dT} \tag{10}$$

one of the forms of which, for standard conditions, is the equation:

$$\Delta G_T^0 = \Delta H_{298}^0 - T\Delta S_{298}^0 \tag{11}$$

$$\begin{aligned} \Delta H^{\circ}_{298}(reaction) &= \\ = \sum n_i \cdot \Delta H^{\circ}_{298}\,(products) &- \\ - \sum n_i \cdot \Delta H^{\circ}_{298}\,(initial\ compounds) & \end{aligned} \tag{12}$$

n_i are stoichiometric coefficients.

The equilibrium constant of a chemical reaction at a temperature of 1800 °C was calculated using tables of standard values. For a given temperature, at a $\Delta G_T^0 < 0$ reaction is possible; when the $\Delta G_T^0 > 0$ reaction is impossible; when $\Delta G_T^0 = 0$ the system is in equilibrium.

Based on the above equations (1-12), the main thermodynamic quantities for chemical elements and compounds involved in the technological process of liquid-phase sintering were determined (Table 1).

Based on the data in Table 1, the values of the change in the Gibbs energy were calculated – ΔG_T^0 for all possible chemical reactions, at a sintering temperature of 1800 °C in a weakly reducing CO atmosphere (Table 2).

Table 1 – Thermodynamic values for chemical elements and ceramic compounds of the composition: MnO_{nano} 1.5 wt. % + Al_2O_{3nano} 2 wt. % + $SiC_{\mu m}$ 94 wt. % + $SiO_{2\ \mu m}$ 2.5 wt. %

Compound	**T_{melt}, °C**	**ρ, g/cm^3**	**$\Delta H_{,\,298\ K}$, kJ/mol**	**S, kJ/mol**
SiC	2830	3.22	− 66.1	16.61
SiO_2	1710	2.65	− 910	41.84
SiO	17 02	2.13	− 92.9	211.6
Si	1414	2.33	0	18.82
MnO	1245	7.21	− 385.1	61.5
MnO_2	535	5.08	− 521.5	53.1
Mn	1517	7.21	0	32.0
Al_2O_3	2044	4.0	− 1675.7	50.9
Al_2O	—	—	− 148.6	264.6
Al	660	2.69	329.1	164.4
CO_2	78	0.0019768	− 393.51	213.67
CO	−205	0.00125	− 110.52	197.54
C	3600	2.25	715.1	157.99
$Al_2(SiO_3)_3\ (Al_2O_3SiO_2)$	1860	3.23	− 166.2	20

Table 2 – Calculation of the change in the Gibbs energy, which determines the possibility of a spontaneous reaction at T = 1800 °C

Chemical reaction	ΔG, kJ/mol	Possibility of the reaction
$2SiO_2 + SiC \rightarrow 3SiO + CO$	− 460305	Reaction is possible
$Al_2O_3 + SiC \rightarrow SiO + Al_2O + CO$	− 1255325	
$MnO + SiC \rightarrow Mn + SiO_2 + CO$	− 401218	
$Al_2O_3 + SiO_2 \rightarrow Al_2(SiO_3)_3\,(Al_2O_3\,SiO_2)$	− 153209.5	
$SiO_2 + 2SiC \rightarrow 3Si + 2CO$	− 779622	
$MnO + SiO_2 \rightarrow MnO_2 + SiO$	− 333819	
Sintering in carbon monoxide (CO)		
$Al_2O_3 + CO \rightarrow Al + CO_2$	− 267309	Reaction is possible
$SiO_2 + CO \rightarrow SiO + CO_2$	− 384816	
$SiC + CO \rightarrow SiO_2 + C$	29667	Reaction is impossible

Thus, taking into account the decrease in the melting temperature of nanosized particles of Al_2O_3 and MnO powders, we can assume the formation of a liquid phase proceeds according to reactions in Table 1. Based on the values of the melting temperature and the end products of chemical reactions, SiO_2, SiO, Si and MnO will contribute to the formation of the liquid phase.

Samples of silicon carbide ceramics obtained by liquid-phase sintering were studied to establish their physical and mechanical properties and structural features. The results of physical and mechanical properties are shown in Table 3.

According to the results of testing the physical and mechanical properties, it was found that the studied ceramic sample reaches a microhardness of 2450 kgf/mm^2, which is an average value found in the literature, while the sintering temperature of ceramic samples obtained by other authors is higher on average by 20%. The density of the sample obtained by us, 3.11 g/cm^3, corresponds to the lower limit of previously encountered data in the literature. According to the experimental results, the open porosity was 0.8%, which also corresponds to the limits of previous studies by other authors. The resulting ceramic material has sufficient density and low porosity, while the use of additives of eutectic compositions of oxide systems with different temperatures of formation of the eutectic melt made it possible to study the effect of these additives on the temperature of compaction and hardening. These studies are relevant for obtaining SiC materials of a granular structure at a relatively low firing temperature while maintaining high mechanical properties.

The results of microstructural analysis of the obtained sample of SiC ceramics are shown in Figure 1.

Table 3 – Physical and mechanical properties of the resulting ceramic sample

Material	Apparent density, g/cm^3	Micro-hardness, kgf/mm^2	Open porosity, %	Total porosity, %	Closed porosity, %	Water absorption, %
Test sample	3.11	2450	0.8	0.34	0.33	0.03
Literature data [17-20]	3.12 – 3.17	2345-2855	0.5-1.2	-	-	-

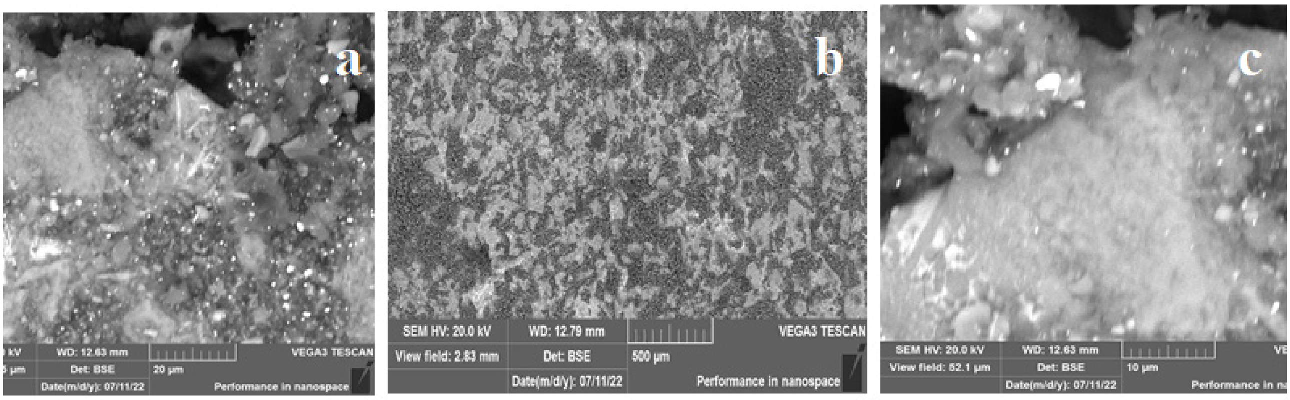

Figure 1 – Microstructure of a sample of SiC ceramics:
a – homogeneous grain structure; b – presence of small pores; c – grain microstructure

The ceramic microstructure is represented by a homogeneous grain structure with an average grain size of ~10 µm (Figure 1a,c). Separate grains of the second phase were not revealed. In the structure of ceramics, the presence of small pores is also observed, apparently formed due to the transformation of the crystal structure and shrinkage of impurity phases during sintering (Figure 1b).

The analysis indicates the presence of C in the composition of ceramics with its content of ~ 57% of the total composition, Al ~ 0.6%, Mn ~ 0.6%, Si ~ 15%, which corresponds to the presence of introduced eutectic additives .

X-ray phase analysis of the sample is shown in Figure 2.

XRD analysis showed that the test sample consists of three main phases, this is a modification of the ring radical of silicate Si_3O_6, silicon dioxide SiO_2 and anorthoclase $(SiAl)O_4$ (Table 4).

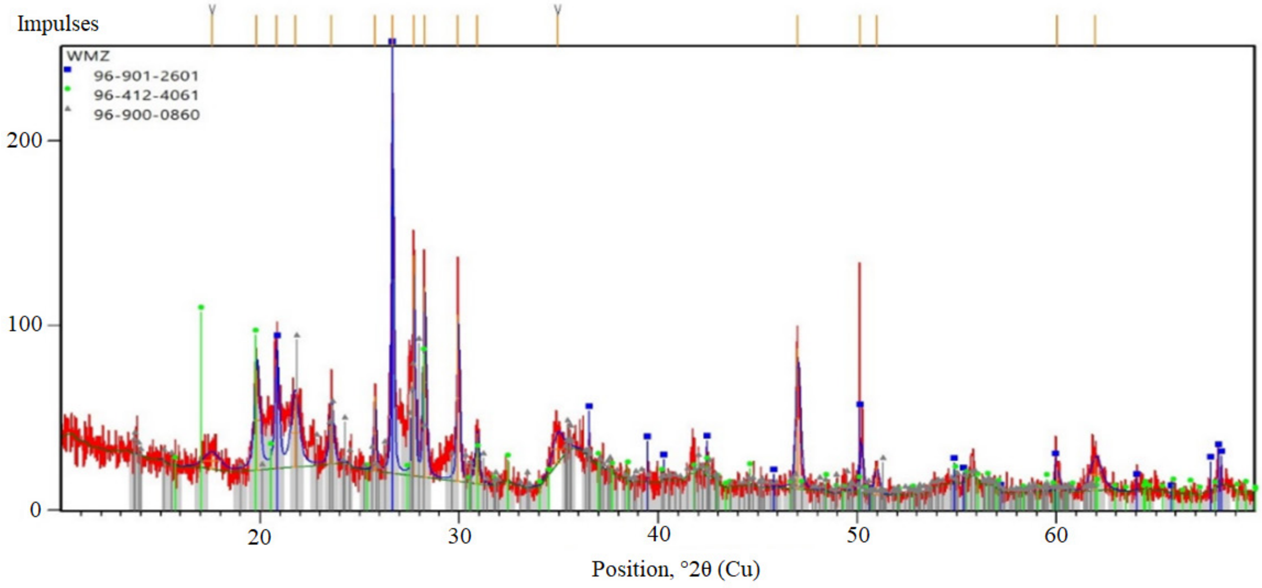

Figure 2 – X-ray spectrum of SiC ceramics sample

Table 4 – PDF cards and phase identification

Card number	Connection name	Offset, [°2θ]	Scale factor	Chemical formula
96-901-2601	Quartz	0.000	1.008	$Si_{3.00}O_{6.00}$
96-412-4061	SiO_2	0.000	0.342	$O_{24.00}Si_{12.00}$
96-900-0860	Anorthoclase	0.000	0.293	$Al_{2.00}Si_{6.00}Na_{1.70}K_{0.30}O_{16.00}$

4 Conclusions

Despite the existence of a wide range of ceramic materials for various purposes, developed based on SiC, the high energy and resource consumption of their manufacture makes it necessary to search for ways to create new types of materials. One of the main solutions is the use of various additives in conjunction with the dispersion of the starting materials. The synthesis of ceramics based on SiC requires high temperatures, and sintering without additives at 2150-2200°C does not allow obtaining dense products due to low diffusion coefficients and high volatility of SiC at these temperatures.

The composition of the charge for sintering carbide ceramics with nanoadditives that form a liquid phase has been developed: MnO_{nano} 1.5 wt. % + Al_2O_{3nano} 2 wt. % + $SiC_{μm}$ 94 wt. % + $SiO_{2μm}$ 2.5 wt. %. The possible chemical reactions during the liquid-phase sintering of ceramics at a temperature of 1800 °C were determined. The values of the change in the Gibbs energy for all possible chemical reactions at a sintering temperature of 1800 °C were calculated by the method of entropy calculation of the equilibrium constants. The elements of the liquid phase and reinforcing additives were determined.

The main physical and mechanical properties of the ceramic sample obtained by liquid-phase sintering at a temperature of 1800 °C were established: characteristics of water absorption, open, total and closed porosity, density and microhardness.

Microstructural analysis of ceramics indicates its grain structure with an average grain size of ~10 μm. The presence of small pores, apparently formed because of the transformation of the crystal structure and shrinkage of impurity phases during sintering, was also recorded in the ceramic structure. Based on the results of XRD analysis, the main phase components of the ceramics based on silicon oxide were determined. It was found that the sample consists of three main phases: modification of the ring radical of silicate Si_3O_6, silicon dioxide SiO_2 and anorthoclase $(SiAl)O_4$.

Such ceramic composite SiC material can have a wide range of applications: as parts of body armor, internal combustion engines and gas turbine engines, cutting tools, ceramic bearings, working units of pumps, nozzles and burners, equipment for firing ceramic products, chemically resistant parts of pipelines, heat exchangers operating in an aggressive environment, heaters of various grain compositions and sizes to obtain temperatures in furnaces in the range up to 1400-1500°C in air.

Acknowledgments

This research was funded by the Science Committee of the Ministry of Education and Science of the Republic of Kazakhstan (Grant No. AP 09058613).

References

1. A.W. Weimar Carbide, nitride and boride materials synthesis and processing / A.W.Weimar (Ed.). – Berlin: Springer Science & Business Media, 2012. – P. 670.

2. M. Khodaei, O. Yaghobizadeh, S.H.N. Alhosseini, S. Esmaeeli, S.R. Mousavie. The effect of oxide, carbide, nitride and boride additives on properties of pressureless sintered SiC: A review // Journal of the European Ceramic Society. – 2019. – Vol. 39 (7). – P. 2215-2231. https://doi.org/10.1016/j.jeurceramsoc.2019.02.042

3. A.A. Bataev, V.A. Botaev. Composite materials: structure, production, application. – M.: Logos, 2006. – P. 381.

4. M. Mokhtarzadeh, M. Carulla, R. Kozak, C. David. Optimization of etching processes for the fabrication of smooth silicon carbide membranes for applications in quantum technology // Micro and Nano Engineering. – 2022. – Vol. 16. – P. 155-206. http://dx.doi.org/10.2139/ssrn.4007858

5. N.T. Andrianov. Chemical technology of ceramics: textbook. Manual for universities / N.T. Andrianov (Ed.) – M.: OOO Reef «Building Materials», 2012. – P. 96.

6. B. Matovic, T. Yano. Silicon carbide and other carbides: from stars to the advanced ceramics. In: Handbook of Advanced Ceramics: Materials, Applications, Processing, and Properties. – Academic Press: Elsevier Inc., 2013. – P. 225.

7. D.V. Grashchenkov, N.E. Shchegoleva, E.P. Simonenko, G.V. Ermakova. High-temperature ceramic composite material, stable during long-term operation up to 2000 °C with a multilevel complex protection system //Polymer Sciences. Series D. – 2012. – No. 5. – P. 205–207. https://doi.org/10.1134/S1995421212030094

8. G. Liu, X. Zhang, X. Chen, Y. He, L. Cheng, M. Huo, J. Yin, F. Hao, S. Chen, P. Wang, S. Yi, L. Wan, Z. Mao, Z. Chen, X. Wang, Z. Cao, J. Lu. Additive manufacturing of structural materials // Materials Science and Engineering: R: Reports. – 2021. – Vol. 145. – P. 596. https://doi.org/10.1016/j.mser.2020.100596

9. Yu.A. Balinova, T.A. Kirienko. Continuous high-temperature oxide fibers for heat-shielding, heat-insulating and composite materials // All materials. Encyclopedic directory. – 2012. – No. 4. – P. 24-29.

10. T. Muranaka, Y. Kikuchi, T. Yoshizawa, J. Akimitsu. Super-conductivity in carrier-doped silicon carbide // Science and Technology of Advanced Materials. – 2008. – Vol. 9. – P. 044204. https://doi.org/10.1088/1468-6996/9/4/044204

11. A. Majid, N. Rani, M.F. Malik, N. Ahmad, al-Hassan N., F. Hussain, A. Shakoor. A review on transition metal doped silicon carbide // Ceramics International. – 2019. – Vol. 45 (7). – P. 8069-8080. https://doi.org/10.1016/j.ceramint.2019.01.167

12. A.P. Garshin, V.I. Kulik, A.S. Nilov. Shock-resistant materials based on technical ceramics: achievements and prospects for improving their ballistic efficiency // Refractories and Industrial Ceramics. – 2016. – Vol. 57. – P. 207-219. https://doi.org/10.1007/s11148-016-9955-0

13. M.B. Trigg, C.H. Oh, N. Rigopoulos. Process for producing dense ceramic product. US patent, No. 5855841 dated 01/05/1999.

14. K. Suzuki, T. Ono, N. Shinohara. Dense sintered silicon carbide ceramic. US patent, No. 4354991 dated 02/19/1982.

15. R. Fuentes. Silicon carbide sintering. US patent, No. 4876226 dated 2/24/1989.

16. M.N. Rahaman. Ceramic processing and sintering. 2nd ed. NY: Marcel Dekker Inc., 2003. – P. 875.

17. Z.H. Huang, D.C. Jia, Y. Zhou, Y.G. Liu. A new sintering additive for silicon carbide ceramic // Ceramics International. – 2003. – Vol.29(1). – P.13-17. https://doi.org/10.1016/S0272-8842(02)00082-2

18. R.A. Andrievsky. Nanostructural materials – state of development and prospects // Perspektivnye materialy. – 2001. – No. 6. – P. 5-11. (in Russian).

19. A. Noviyanto, B.-K. Min, H.-W. Yu, D.-H. Yoon. Highly dense and fine-grained SiC with a Sc-nitrate sintering additive // Journal of the European Ceramic Society. – 2014. – Vol. 34 (3). – P. 825-830. https://doi.org/10.1016/j.jeurceramsoc.2013.10.001

20. S.V. Zhitnyuk, O.Yu. Sorokin, P.L. Zhuravlev. Silicon carbide-based ceramic, obtained by sintering granulated powder // Composite materials. Proceedings VIAM. – 2020. – No.2 (86). – P. 50-59.

21. U. Degenhardt, F. Stegner, C. Liebscher, U. Glatzel, K. Berroth, W. Krenkel, G. Motz. Sintered silicon nitride/nano-silicon carbide materials based on preceramic polymers and ceramic powder // Journal of the European Ceramic Society. – 2012. – Vol. 32 (9). – P. 1893-1899. https://doi.org/10.1016/j.jeurceramsoc.2011.09.007

22. J. Boehmler, F. Moitrier, T. Bourré, J. Rossit, F. Delorme, S. Lemonnier. Influence of powder state and rheology on sintering behaviour of SiC // Open Ceramics. – 2021. – Vol. 8. – 100192. https://doi.org/10.1016/j.oceram.2021.100192

23. B. Yuan, H.-X. Li, G. Wang, J.-B. Yu, W.-K. Ma, L.-F. Liu, Y.-S. Liu, Z.-J. Shen. Preparation and properties of porous silicon carbide based ceramic filter // Journal of Alloys and Compounds. – 2016. – Vol. 684. – P.613-615. https://doi.org/10.1016/j.jallcom.2016.05.216

24. A.M. Zhilkashinova, S.K. Kabdrakhmanova, A.V. Troyeglazova, M.B. Abilev. Structure and properties of metallurgical-grade silicon // Silicon. – 2018. – Vol. 10, Issue 5. – P. 2201-2210.

25. A. Rahman, A. Singh, S.P. Harimkar, R.P. Singh. Mechanical characterization of fine grained silicon carbide consolidated using polymer pyrolysis and spark plasma sintering // Ceramics International. – 2014. – Vol. 40 (8). – P. 12081-12091. https://doi.org/10.1016/j.ceramint.2014.04.048

Physical Sciences and Technology. Vol. 9 (No. 3-4), 2022: 32-38

IRSTI 55.09.35 https://doi.org/10.26577/phst.2022.v9.i2.05

Features of the production and calibration of reference hardness test blocks

M.B Zhamanbalin and A.M. Ilyasov*

Karaganda branch of the Republican State Enterprise «Kazakhstan Institute of
Standardization and Metrology», Karaganda, Kazakhstan
*e-mail: a.ilyasov@ksm.kz

(Received 27 September 2022; received in revised form 1 December; accepted 13 December 2022)

This article provides an information about the production of reference hardness measurements on the Brinell scales (type MTB-K), Rockwell A, B, C (type MTR-K), Superficial Rockwell N and T (type MTSD-K), brief information about the state of production of hardness measures in the world and the research conducted at this institute in the development and improvement of manufacturing technology. The physical and chemical properties of the studied measuring instruments are given. Hardness measures are intended for setting, calibration or verification according to standardized hardness scales of stationary and portable hardness measuring instruments, for example, software. Reference hardness measures are manufactured in accordance with GOST 9031-75 «Exemplary hardness measures. Specifications» made of carbon and alloy steels, passing through the stages of mechanical and heat treatment, have a rectangular, triangular or round shape. Reference hardness measures in accordance with the law «On Ensuring the uniformity of measurements in the Republic of Kazakhstan» are calibrated. Primary and periodic verification of hardness measurements is carried out by the bodies of the metrological service accredited for the right to verify hardness measuring instruments. The verification interval is 2 years in accordance with the interstate standard GOST 8.335-2004 «Standard hardness measures. Verification method».

Keywords: hardness measurement, hardness test blocks, number of hardness, hardness scales, heat treatment, production.
PACS number: 06.20.– f

1 Introduction

In modern production, the assessment of the physical properties of metal products, as well as the solution of issues related to the control of technological processes in industry, are inextricably linked with mechanical testing of materials and, in particular, with hardness measurements. Hardness measurements are distinguished by simplicity and high productivity, the ability to test, without the manufacture of special samples, directly on the surface of the product, while slightly violating its shape and physical characteristics. The hardness of materials is determined by scales corresponding to the measurement method [1-4, 7].

Hardness measurements are used in engineering, metallurgy, mining, transport, and energy enterprises. For verification/calibration, as well as setting up stationary and portable devices for measuring hardness on the Brinell, Vickers, Rockwell and Super-Rockwell scales, reference hardness measures are used. Verification of these devices is carried out according to various methods of verification, incl. on [6, 8, 9].

In Kazakhstan, there was historically no production of hardness measures, they were imported in the vast majority from Russia (PO «Tochpribor», CPCR «MET»). Thus, the production of hardness blocks in the Republic of Kazakhstan is a new and promising direction in the production of measuring instruments, while the need for enterprises to use hardness blocks is high, and moreover, a further increase in demand is expected due to the opening of new production facilities.

Reference hardness measures [5], which are produced in the KF RSE «KazStandard», undergo metrological certification on state standards of hardness according to the Brinell, Vickers, Rockwell and Super-Rockwell scales. Calibration and measurement capabilities of the above standards are confirmed by international comparisons within COOMET and published on the BIPM website [10,11].

The main objective of this production is to increase the level of metrological support for verification / calibration of working hardness measuring instruments used at industrial enterprises of the Republic of Kazakhstan.

2 Development of production technology

The main requirement for a measure of hardness is the uniformity of the working surface and the stability of physical and mechanical properties over time. The homogeneity criterion is the range of hardness numbers. The arithmetic mean of the results of measurements of five prints applied evenly over its surface is taken as the actual value of the hardness of the measure.

When developing the technology, the factors affecting the uniformity of hardness measures were considered, and on the basis of research work, grades and assortment of steels were selected.

In all countries, in the production of hardness blocks, various technologies for their manufacture are used. The production technology of each manufacturer is unique, incl. differences in the steels used. National standards have their own steel grades and requirements for the assortment, their chemical composition and structure. Table 1 shows the chemical composition of the steels used in the production of test blocks in some countries.

In the process of developing the technology for the production of hardness blocks, a chemical and microstructural analysis of the hardness blocks produced by the Tochpribor software, manufactured in 1989, was carried out. The results of the analysis are shown in table 2.

Table 3 shows the requirements for the chemical composition of U8A-U10A, KhG, KhVG steels used for the production of hardness measures.

Table 1 – The chemical composition of steels used in various states

Manufacturer country	**Steel designation**	**Chemical composition of steel, %**									**Analogue of the steel grade according to the RD of the RK**
		C	Mn	Si	P	S	Cr	Ni	W	V	
Japan	SK4	0,9	0,36	0,25	0,013	0,007	0,04	-	-	-	U9A
Japan	JWP9	0,87	0,33	0,32	0,018	0,009	0,04	0,13	-	-	U8-U9A
USA	01	0,95	1,27	0,24	0,026	0,015	0,5	-	-	-	HGC
Great Britain	2S31	1,0	1,2	0,2	0,03	0,01	0,6	0,5	0,2	0,4	HBG

Table 2 – Studies of hardness measures produced by PO «Tochpribor»

Number, hardness scale	**Chemical composition, %**			**steel grade**	**macrostructure**	**microstructure**
	C	Mn	Si			
25 HRC	0,96	0,33	0,32	У10	1 score	Uniform sorbitol
61 HRC	Steeloscope			У10		Trostite hardening
104 HB	0,11	0,60	0,33	Ст10		Uniform ferrite-pearlite
203 HB	1,00	0,30	0,22	У10		Uniform sorbitol

Table 3 – Requirements for the chemical composition of steels

steel grade	**Chemical composition of steel, %**							**Source**
	C	Mn	Si	P	S	Cr	W	
У8А	0,75-0,84	0,17-0,28	0,17-0,33	0,025	0,018	-	-	GOST 1435-99
У9А	0,85-0,94	0,17-0,28	0,17-0,33	0,025	0,018	-	-	GOST 1435-99
У10А	0,95-1,09	0,17-0,28	0,17-0,33	0,025	0,018	-	-	GOST 1435-99
ХГС	0,95-1,05	0,85-1,25	0,4-0,7	-	-	1,3-1,65		GOST 5950-2000
ХВГ	0,9-1,05	0,8-1,1	0,1-0,4	-	-	0,9-1,2	1,2-1,6	GOST 5950-2000

Conducted studies and subsequent analysis show that carbon and alloy steels are used in most cases for production.

The range of steels used in the production of hardness tests is also individual. In Japan, hardness test blocks are made from forged billets, in Switzerland (HMT company) powder metallurgy technology is used, the rest of the countries use mainly rolled strip.

Heating for hardening in the Russian Federation, Great Britain, Poland is carried out in salt baths of various compositions, and in Japan, the Czech Republic in electric furnaces. Quenching media also differ: for alloy steels – oil, carbon steels – water or aqueous solutions of caustic soda or sodium chloride. After hardening, some manufacturers use cold treatment. Vacation is carried out in oil baths (Russia, Japan), salt baths (Poland, USA) or in electric furnaces (Great Britain, Russia) with artificial circulation of the medium.

In order to reduce costs in the production of hardness blocks, manufacturers use the smallest possible range and the cheapest steel grades.

In the production of hardness blocks, the conversion of hardness numbers according to various hardness scales is used, for example, hardness blocks of 25 HRC correspond to a hardness level of 200 HB. Figure 1 shows the ratio of the levels of various scales and methods of measuring hardness to HV30 [12].

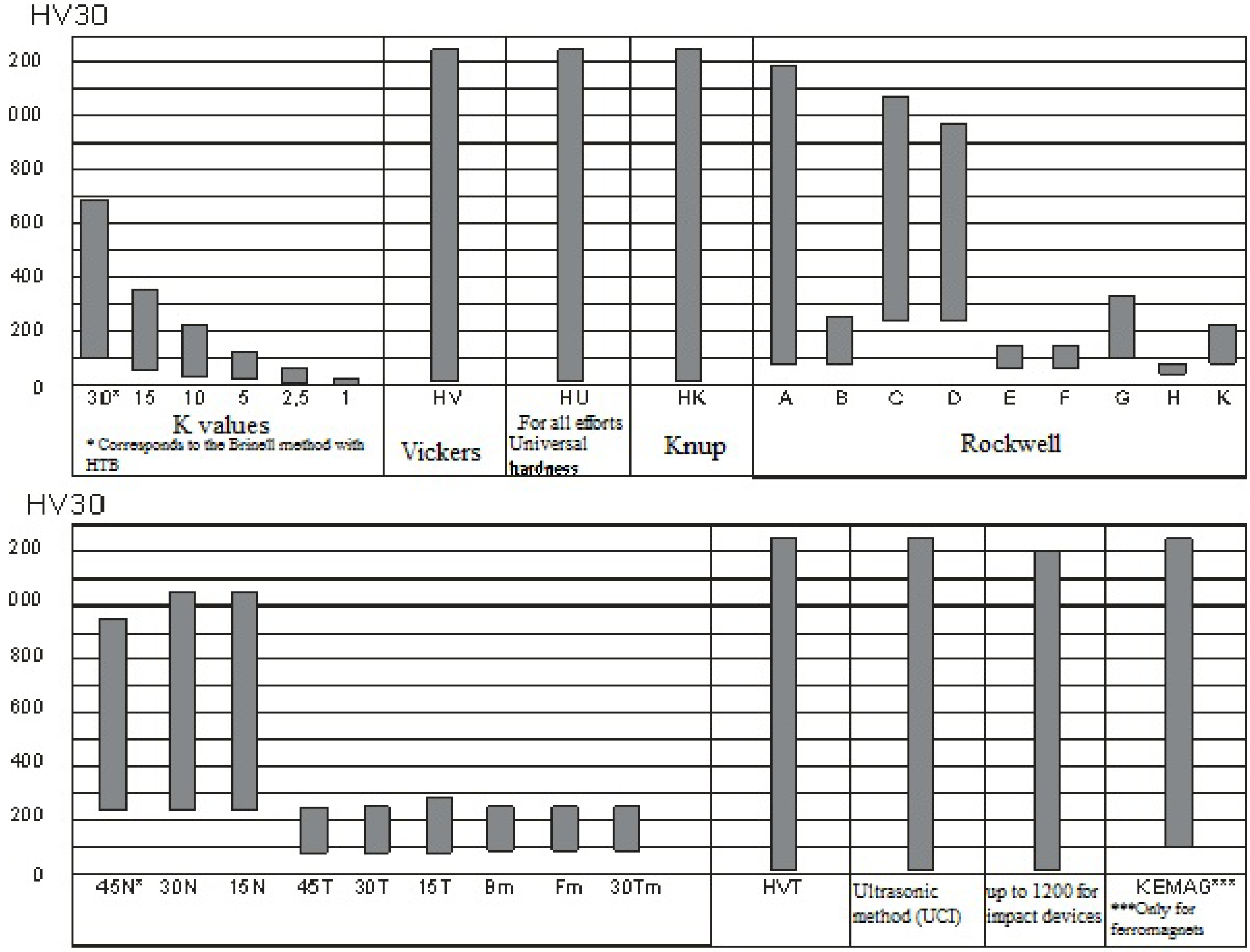

Figure 1 – The ratio of the levels of various scales and methods of measuring hardness to the Vickers hardness scale HV30

The developers of various portable and stationary, electronic devices for measuring hardness are also forced to use the conversion of hardness numbers [13], [14], [15].

Based on the information obtained in the study of hardness measures and pilot production of hardness samples, the main factors influencing the heterogeneity of hardness measures were determined, which include:

composition and grade of steel;

metallurgical production at the smelting stage (quality of steels, additional processing by remelting with slag, grain size, etc.);

assortment of rolled metal products, i.e. rolling method affecting the structure;

method of machining workpieces (cutting, milling);

heat treatment [16], [17];

finishing surface treatment of workpieces (grinding, polishing).

The method of steel smelting affects the purity of steels from impurities, the structure of grain boundaries. The use of steels, in the production of which electroslag remelting or vacuum holding of steel was used, makes it possible to increase the uniformity of hardness measures. Vacuum remelting frees steel from hidden impurities – nitrogen, oxygen, hydrogen and non-metallic inclusions. Vacuum pumps pump out gaseous oxides of CO, CO2 and H2O and reduce the oxygen content in steel. Electroslag remelting frees steel from non-metallic inclusions – sulfur, phosphorus, etc. In this process, the crystallization of the metal bath is slowed down from the bottom up, which allows you to clean the steel from gases, harmful impurities and non-metallic inclusions.

In [18], it is recommended to use rectangular hardness test blocks made from strips that are rolled with a high degree of reduction, which has a positive effect on uniformity. Also, the strip for the workpiece is selected as close as possible to the thickness of the workpiece, because the thinner the strip, the greater the degree of compression it undergoes.

According to [19], during grinding of parts, burns and surface stresses, the formation of a secondary hardened layer, and an inhomogeneous decrease in hardness can occur if the depth of cut during grinding goes beyond certain limits and measures are not taken to ensure sufficient cooling of the parts.

The technology for the production of hardness blocks as reference measuring instruments is complex and time-consuming. The technology for the production of hardness blocks as reference measuring instruments is complex and time-consuming.

3 Stages of development of own production

In 2010, for the first time in the Republic, RSE «KazStandard» on the basis of a branch in Karaganda, mastered small-scale production of hardness measures according to Brinell, Rockwell and Super-Rockwell scales. Technical and metrological characteristics of the produced hardness test blocks are presented in tables 4 and 5.

Table 4 – Technical and metrological characteristics of Brinell hardness test blocks MTB-K

Hardness scale HB (HBW)	Intervals of hardness numbers, HB (HBW)	Range of hardness numbers, no more, %	Weight, no more than, kg
10/3000	(400 ± 50); (200 ± 50)	3,0	1,6
10/1000	(100 ± 50)	4,0	
5/750	(400 ± 50); (200 ± 50)	3,0	

Table 5 – Technical and metrological characteristics of hardness test blocks according to Rockwell MTP-K and Super-Rockwell MTSR-K

Hardness scale	Intervals of hardness numbers, HR	Range of hardness numbers, no more, HR	Overall dimensions, (length × width × height), not less than, мм	Weight, no more than, kg
HRA	83 ± 3	0,6	60×40×6	0,24
HRB	90 ± 10	1,2		
HRC	25 ± 5 45 ± 5 65 ± 5	1,1 0,8 0,5		
HRN15	92 ± 2	0,6		
HRN30	80 ± 4 45 ± 5	0,6 1,1		
HRN45	49 ± 6	1,1		
HRT30	76 ± 6 45 ± 5	1,2 1,8		

In 2017, a pilot batch of reference hardness tests according to the Vickers MTV-K scales was produced, which are manufactured in accordance with [5]. The developed technology did not allow obtaining hardness measures due to the existing high level of defects. It is required to conduct research in order to adjust the technology. Vickers hardness measures are subject to higher requirements for the roughness of the working surface (roughness parameter Ra is not more than 0.04 μm [5], [14]) compared to measures of other scales, which significantly increases the complexity of their production [17]. Table 6 is given below with the metrological characteristics of Vickers hardness testers of the 2nd category [5].

Figure 2 shows a general view of the hardness blocks manufactured by the KF RSE «KazStandard».

Table 6 – Metrological characteristics of hardness measures according to Vickers

Test load, H	Hardness number	Range of hardness values, %, no more
1	450 ± 75 800 ± 50	5,0
5, 10	450 ± 75 800 ± 50	3,0
20, 30, 50	450 ± 75 800 ± 50	2,0

Figure 2 – General view of hardness measures

4 Conclusions

In 2020, the share of Kazakhstani content of hardness test blocks KF RSE «KazStandard» increased from 61.1% (as of 2016) to (97.2-98.4)% for hardness testers MTR-K and MTSR-K and (81 .0-89.7) % for MTB-K hardness test blocks.

Since 2010, the volume of production of hardness blocks has grown 4 times. The distribution of sales volumes until 2021 is shown in Figure 3.

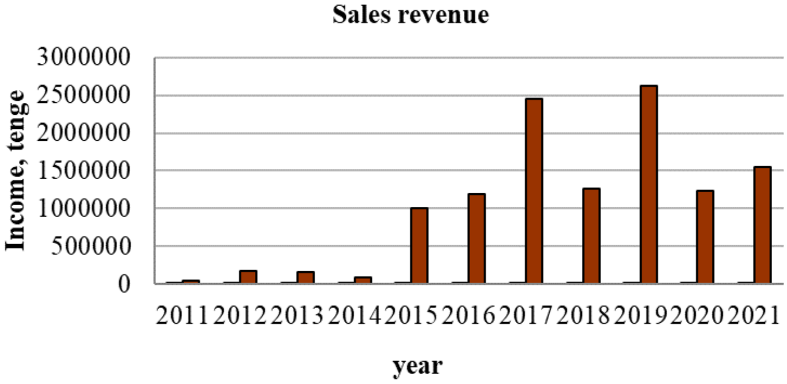

Figure 3 – Volumes of implementation of hardness measures

In the process of production of hardness blocks, problems arise regarding the dependence on third-party enterprises when they perform subcontracting work – cutting blanks, milling, grinding [25], which leads to a significant increase in the cost of manufacturing hardness blocks.

In order to optimize the activities for the production of reference hardness blocks and reduce costs on an ongoing basis, experimentally, some technological operations are being revised during the heat treatment of a batch of blanks of reference hardness blocks, depending on the results of metrological certification. Thus, this will provide the domestic market of Kazakhstan with a sufficient number of hardness measures at prices acceptable to users.

Prospects for the development of production include the following steps:

purchase of technological equipment;

continuation of work related to improving product quality.

References

1. GOST 9012-59 «Metals. Brinell hardness method» // Standartinform. Moscow, p. 40. Shop. http://shop.ksm.kz. (in Russian).
2. GOST 2999-75 «Metals. Method for measuring hardness with a Vickers diamond pyramid». Moscow, p. 31. http://shop.ksm.kz. (in Russian).
3. GOST 9013-59 «Metals. Rockwell hardness method». Moscow, p. 8. http://shop.ksm.kz. (in Russian).
4. GOST 22975-78 «Metals. Method for measuring Rockwell hardness at low loads (by Super Rockwell). Moscow, p. 12. http://shop.ksm.kz. (in Russian).
5. GOST 9031-75 «Measures of hardness are exemplary. Specifications». Moscow, p. 7. http://shop.ksm.kz. (in Russian).
6. GOST 8.335-2004 «Reference hardness measures. Verification procedure». Moscow, p. 11. http://shop.ksm.kz. (in Russian).
7. RMG 83-2007 «SMS. Measurement scales. Terms and Definitions». Standartinform. Moscow, p. 24. http://shop.ksm.kz. (in Russian).
8. GOST 8.398-80 «Instruments for measuring the hardness of metals and alloys. Methods and means of verification». Moscow, p. 18. http://shop.ksm.kz. (in Russian).
9. ST RK 2.309-2014 «Portable electronic devices for measuring the hardness of metals and alloys». Astana, p. 26. http://shop.ksm.kz. (in Russian).

10. Metrologia, 2009, 46, Tech. Suppl., 07001 COOMET.M.H-S1 Final Report, 2009, p. 12 . https://iopscience.iop.org/article/10.1088/0026-1394/46/1A/07001.

11. Final report on RMO Vickers key comparison COOMET M.H-K1, https://iopscience.iop.org/article/10.1088/0026-1394/50/1A/07015.

12. K. Herrmann. Hardness testing. Principles and application. ASM International. Ohio, USA. – 2011, 247 p. .

13. Leeb D. Dinamic measurement of hardness or strength of materials, own calculations.

14. M. Kompatscher Dynamic hardness measurements, MAPAN // Journal of Metrology Society of India. – 2005. -Vol. 20. -P. 25-36. https://www.springer.com/journal/12647/.

15. T. Polzin, D. Beisei, D. Schwenk. Revaluation of hardness values, remarks on the application of DIN EN ISO 18265 in practice, conference proceedings Material Testing // – 2006, ed. VDEh.

16. A.P. Gulyaev, A.S. Zhigarev. Thermomechanical treatment of steel and its effect on mechanical properties // Metal Science and Heat Treatment of Metals. -1961. -Vol. 3. -P. 190-192. https://doi.org/10.1007/BF00812973

17. E.A. Smolnikov. Thermal treatment of tools in salt baths, mechanical engineering. Mashinostroeniye. Moscow, 1981, 271 p. (in Russian).

18. E.A. Volkova, A.V. Smirnov. Heterogeneity of hardness test blocks from carbon steel and ways to eliminate it. Proceedings of VNIIM. Release 50 // L. Standardgiz. – 1961.

19. NIKIMP Report №895 – «Study of technological processes for manufacturing exemplary hardness tests for the TK-2 device»: M. – 1961.

20. ISO 6507-3:2018 Metallic materials – Vickers hardness test – Part 3: Calibration of reference blocks. https://www.iso.org/ru/standards.html.

21. ISO 6506-3:2014 Metallic materials – Brinell hardness test – Part 3: Calibration of reference blocks. https://www.iso.org/ru/standards.html.

22. GOST 2789-73 Surface roughness. Parameters and characteristics. Standartinform. Moscow, p. 7. http://shop.ksm.kz. (in Russian).

23. Z.I. Kremen, V.G. Yuriev, A.F. Baboshkin. Grinding technology in mechanical engineering. Politechnika. Moscow, Russia. 2007, 425 p. (in Russian).

24. Zhamanbalin M.B. Production of reference test blocks // Metrology. – 2016. № 3, p.12-14.

25. VNIIM Report No. Zh-Z/18 for 1961. Investigation of the reasons for the heterogeneity of hardness measures in order to eliminate them. – 1961.

Funded by Al-Farabi KazNU

IRSTI 29.19.04 https://doi.org/10.26577/phst.2022.v9.i2.06

Study of functional properties stability of SnO_2 films on the duration thermal exposure and temperature changes

R. M. Zhapakov*, M. A. Begunov and D. O. Murzalinov

Satbayev University, Almaty, Kazakhstan
*e-mail: zharash@mail.ru

(Received 12 October 2022; received in revised form 14 December; accepted 20 December 2022)

Thin films of tin oxide and composite systems based on them have found the greatest applications in solar energy. The properties of oxides depend on the obtaining technology and following processes. The choice of the optimal solution maturation time influences the functional properties of the films. In this research, solutions with the adding different volume of concentrated aqueous solution of ammonia (NH4OH) per 100 ml of the system were prepared: 0.8 ml (pH=1.40), (pH=1.46) and 1.6 ml (pH=1.49). This enabled the study of the properties of films obtained from solutions of different acidity. The resistance of the films was measured in the 10 different parts of the films. In addition, the effect of the isothermal annealing time at 2500C on the structural and optical properties of the samples was investigated. As a result of this study, there was found the correlation between an increase in the duration of annealing and a decrease in the transparency of films obtained from the SnCl4/EtOH. The annealing at temperature 2500C within 6 hours led to a change in transparency of films from 93% (λ=550nm) to 88%. The further increase of the annealing duration up to 9 hours does not affect the transparency of films.

Keywords: sol-gel, tin dioxide, surface resistance, thermal exposure, transmission spectra.
PACS numbers: 61.43. Dq, 39.30. +w

1 Introduction

The dual valency of Sn provides the reversible transformation of the stoichiometric surface with Sn4+ surface cations into a reduced surface with Sn2+ surface cations. This reaction depends on oxygen chemical potential of the system. As a result of the surface reduction, Sn 5s derived surface state forms. This surface state lowers the work function and located inside of the band gap. This property provides sensorial characteristics for materials.

Thin films of tin oxide and composite systems based on them have found the greatest applications as active layers in gas analytical equipment [1–4]. Films based on tin dioxide are of great importance for intensively developing solar energy [5–7]. Tin dioxide films are also used as transparent electrodes, catalysts, anti-reflective coatings. [8-13].

Tin oxide films have good adhesion to the glass surface, high electrical conductivity, transparency, mechanical strength and chemical resistance. These properties allow them to be used as transparent conductive coatings [14-16].

Tin dioxide is transparent in the visible and near ultraviolet regions. The properties of oxides depend on the manufacturing technology and subsequent processing [17]. Currently, several methods have been developed for producing a thin film of tin dioxide based on sol-gel technology [18-20]. In particular, the choice of the optimal solution maturation time affects the properties of the resulting films. Thus, in [21], it was found that 12 hours is the optimal time for the maturation of the solution for the manufacture of films with high transparency, and 8 hours for the manufacture of films with low resistance. It should be noticed that the change in color and viscosity of the film-forming solution indicates the gel formation. The gel formation in [21] begins 10 hours after the preparation of the solution.

This paper presents studies of changes in the resistance of films upon repeated annealing. Films obtained from solutions of SnCl4 dissolved in ethyl alcohol with a concentration of tin ions of 0.16 mol/l were used for analysis.

2 Materials and Methods

During operation, the films may be subjected to thermal stress. Therefore, along with studies of the properties of the obtained films, the question also arises of maintaining the stability of the functional properties of the films.

To study the properties of films obtained from solutions of different acidity, a series of solutions were prepared with the addition of 0.8 ml (pH=1.40), (pH=1.46) and 1.6 ml (pH=1.49) of a concentrated aqueous solution of ammonia (NH_4OH) per 100 ml of the system.

Film-forming systems were deposited on a glass substrate by dropping and flowing at an angle of 45^0. The resulting samples were dried at room temperature for 30 minutes and then annealed in a muffle furnace for 15 minutes. After cooling the sample at room temperature, its resistance was measured (the distance between the contacts was 1 mm).

3 Results and Discussion

The resistance of the films was determined by 10 measurements in different parts of the samples. Student's coefficient for 10 measurements with a reliability of 0.95 = 2.262. The error was calculated by the formula:

$$\Delta\bar{A} = t_{\gamma,n-1}\frac{\sqrt{\frac{\sum_{i=1}^{n}(A_i-\bar{A})^2}{n-1}}}{\sqrt{n}}$$

where, $\Delta\bar{A}$ – the absolute measurement error, $\Delta\bar{A}$ – the Student's coefficient, A_i – is the value of the i-th measurement, $\bar{A}$ – the arithmetic mean, n – the number of measurements.

The measurement results are presented in Table 1.

Table 1 – Resistance of samples obtained from solutions of $SnCl_4$ of different acidity, after a single annealing

pH	1.40	1.46	1.49
R, MOhm	0.755± 0.132	2.805± 0.383	11.02± 4.61

To study the preservation of the stability of the functional properties of the films under thermal exposure, the samples were reannealed at a temperature of 2000C and 4000C for 15 minutes. The measurement results are presented in Table 2.

Table 2 – Resistance of samples obtained from solutions of $SnCl_4$ of different acidity, after secondary annealing at temperatures t=200^0C and 400^0C

pH	1.40	1.46	1.49
R, MOhm (t=200^0C)	0.798± 0.223	2.861± 0.103	11.2± 2.2
R, MOhm (t=400^0C)	0.532± 0.094	0.742± 0.123	6.32± 2.52

A comparative analysis of tables 1 and 2 shows that repeated annealing at 200^0C (15 minutes) does not lead to a significant change in resistance. At the same time, after repeated annealing at a temperature of 400^0C, the resistance decreases by about 1.5 times for the initial sample (without the addition of ammonium hydroxide) with pH = 1.40 and by 2-4 times for films obtained from solutions with a higher pH value.

With an increase in the annealing temperature, the sizes of SnO_2 crystallites increase due to the crystallization of the amorphous phase and the association of crystallites as a result of partial or complete destruction of defective crystallites during annealing with the addition of their atoms to more advanced crystallites. An increase in the size of crystallites and their perfection contributes to a decrease in the resistance of the films.

Thus, annealing for 15 minutes is insufficient to form a complete structure with stable functional properties.

The practical application of films is often associated with their heating. The "working mode", in many cases, means the presence of films, for a long time, in a heated state. In connection with the foregoing, the question arises about the stability of the properties of the films under prolonged thermal exposure.

In this section, the influence of the duration of isothermal annealing at 250^0C on the structure and optical properties of the obtained films is considered.

Figure 1 shows the transmission spectra of thin SnO_2 films obtained from a film-forming system with pH=1.40; 1.46 and 1.49.

As can be seen from Figure 1a, the transmittance decreases for films obtained from the $SnCl_4$/EtOH system with a tin ion concentration of 0.16 mol/l (pH=1.40) with an increase in the annealing time. The transmittance varies from 93% (λ=550nm) to 88% with an annealing time of 6 hours at 250^0C. Increasing the annealing time to 9 hours does not lead to a further decrease in the transmittance.

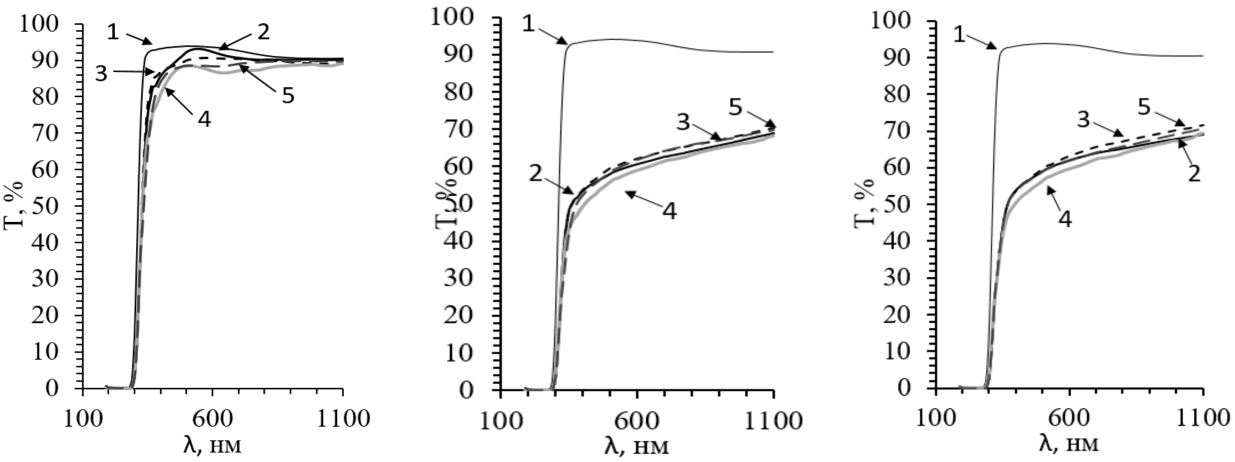

a) solution with acidity pH=1.40 b) solution with acidity pH=1.46 c) solution with acidity pH=1.49
1) glass substrate; 2) upon receipt; 3) annealing 3 hours; 4) annealing 6 hours; 5) annealing 9 hours
Figure 1 – Transmission spectra of thin SnO_2 films

The transmittance (Figure 1b, c) of samples obtained from the $SnCl_4$/EtOH system with pH = 1.46 and 1.49, with an increase in the duration of annealing up to 9 hours at 250^{0}C, changes by 1-2%.

Films, to study the stability of properties from the duration of thermal exposure, were prepared from the same film-forming systems as the films studied in the first section of this report. However, the application of the films was after three months of aging of the film-forming systems.

Figure 2 presents the surface structure of thin SnO_2 films obtained from the $SnCl_4$/EtOH film-forming system with a tin ion concentration of 0.16 mol/l.

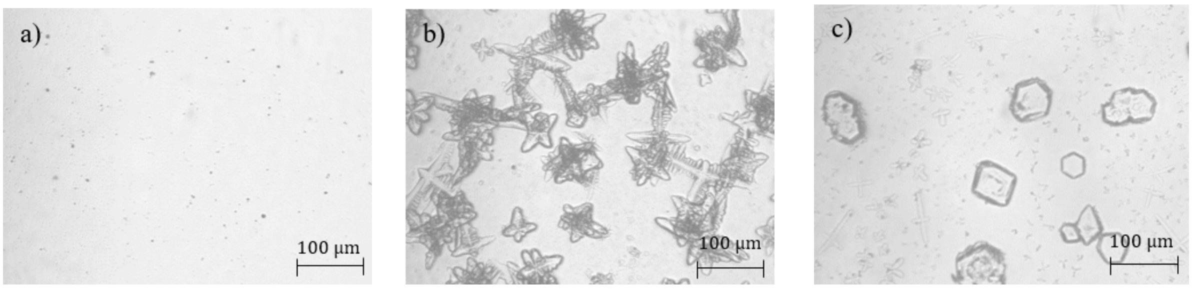

a) solution with acidity pH=1.40 b) solution with acidity pH=1.46 c) solution with acidity pH=1.49
Figure 2 – The structure of the surface of the films after production

Figure 2 shows that at pH 1.40 the film-forming system has a relatively even surface (Figure 2a). At a pH of the film-forming system of 1.46, cruciform structures are formed (Figure 2b). At a system pH of 1.49, pronounced crystals of the cubic syngony formed (Figure 2c). Since HCl and an aqueous solution of ammonia are present in the film-forming system, these are presumably NH4Cl crystals. The interaction goes according to the reaction:

$$NH_4OH + HCl \quad NH_4Cl + H_2O \qquad (1)$$

Weak structural elements in the form of small cruciform structures, presumably composed of tin hydroxide and/or dioxide. Tin hydroxide, at the time of formation, has an amorphous structure. Tin dioxide is formed from tin hydroxide by the reaction:

$$Sn(OH)_4 \overset{heating}{\quad} SnO_2 + 2H_2O \qquad (2)$$

Figure 3 shows the surface structure of the films after annealing at 250^{0}C for 3 hours.

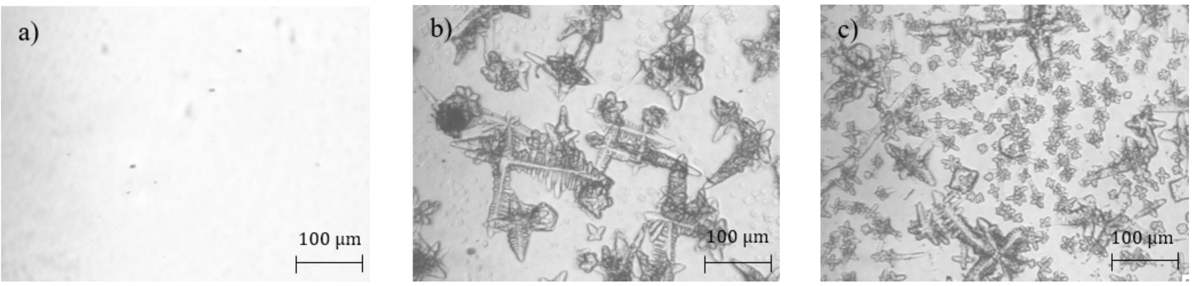

a) solution with acidity pH=1.40 b) solution with acidity pH=1.46 c) solution with acidity pH=1.49

Figure 3 – Surface structure of films after annealing at 250^{0}C for 3 hours.

As can be seen from Figure 3a, no noticeable changes are observed in the structure of the films obtained from a film-forming system with pH=1.40 after annealing at 250^{0}C for three hours. In the films obtained from a film-forming system with pH = 1.46, an increase in structural formations is observed (Figure 3b). In the films obtained from a film-forming system with pH = 1.49, both cubic syngony crystals and many large and small four- to six-petaled structures are observed (Figure 3c).

Figure 4 shows the surface structure of the films after annealing at 250^{0}C for 6 hours. Six hours of annealing at 250^{0}C did not lead to a change in the structure of the films obtained from the film-forming system with pH=1.40 (Figure 4a). In the films obtained from a film-forming system with pH=1.46 (Figure 4b), an increase in size of structural formations is observed. After six hours of annealing at 250^{0}C, no cubic crystals are observed in the structure of the films obtained from the film-forming system with pH=1.49 (Figure 4c). The four- to six- petaled structures increased in size.

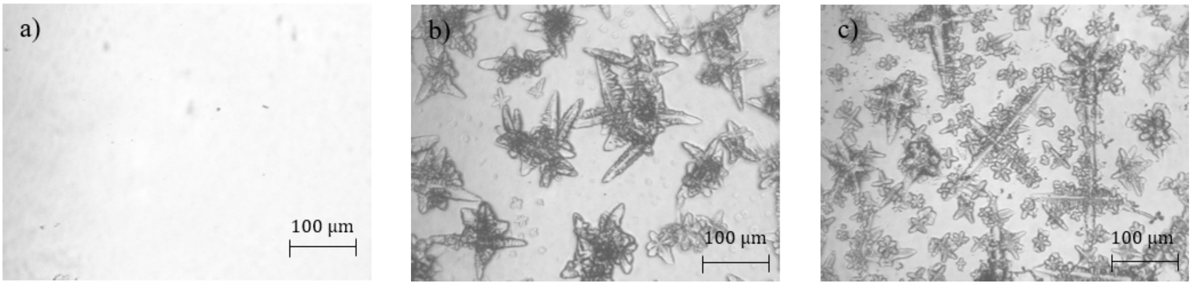

a) solution with acidity pH=1.40 b) solution with acidity pH=1.46 c) solution with acidity pH=1.49

Figure 4 – Surface structure of films after annealing at 250^{0}C for 6 hours

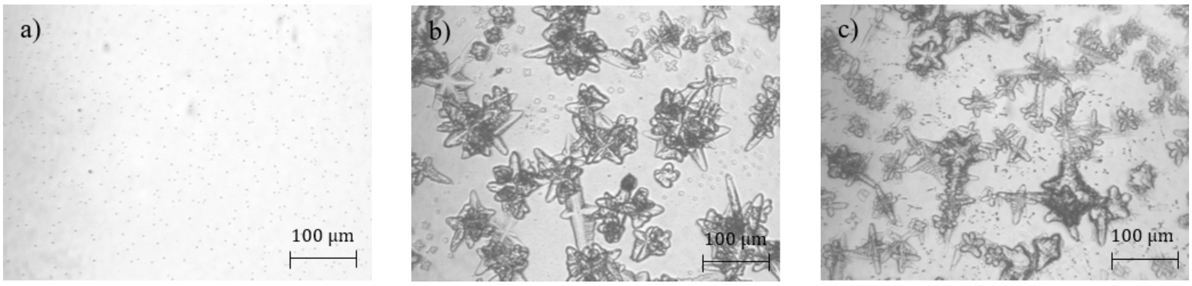

a) solution with acidity pH=1.40 b) solution with acidity pH=1.46 c) solution with acidity pH=1.49

Figure 5 – Surface structure of films after annealing at 250^{0}C for 9 hours

Figure 5 shows the surface structure of the films after annealing for 9 hours at 250^{0}C. As can be seen from Figure 5a, a lot of point structural elements appeared in the film obtained from the film-forming system with pH=1.40. Nine hours of annealing at 250^{0}C leads to the growth of structures in films obtained from a film-forming system with pH=1.49. There are no cubic crystals.

The cubic modification of NH_4Cl is stable below 184.3^{0}C. Prolonged annealing at a temperature of 250^{0}C leads to the gradual decomposition of NH_4Cl into volatile compounds according to the reaction:

$$\begin{array}{c} T > 184{,}3^0C \\ NH_4Cl\ NH_3 + HCl \end{array} \qquad (3)$$

At 337.6^{0}C, ammonium chloride sublimes with decomposition (according to reaction 3).

4 Conclusions

A decrease in the transparency of films obtained from the SnCl4/EtOH system with a concentration of tin ions of 0.16 mol/l (pH=1.40) with an increase in the duration of annealing was found. Transparency varies from 93% (λ=550nm) to 88% with an annealing time of 6 hours at 2500C. Increasing the annealing time to 9 hours does not lead to a further decrease in transparency. The transparency of the samples obtained from the SnCl4/EtOH system with pH=1.46 and 1.49, with an increase in the duration of annealing up to 9 hours at 2500C, changes within the measurement accuracy. The surface structure of the films changes with increasing annealing time. Additional structural formations are formed.

References

1. I. H. Kadhim, H. Аю Hassan, Q. N. Abdullah. Hydrogen gas sensor based on nanocrystalline SnO_2 thin film grown on bare Si substrates // Nano-Micro Lett. – 2016. – Vol. 8. – №.1. – P. 20–28. https://doi.org/10.1007/s40820-015-0057-1
2. G. Fedorenko, L. Oleksenko, N. Maksymovych, G. Skolyar, O. Ripko. Semiconductor gas sensors based on Pd/SnO_2 nanomaterials for methane detection in air // Nanoscale Research Letters. – 2017. – Vol. 12. – P. 329. https://doi.org/10.1186/s11671-017-2102-0
3. E.V. Sokovykh, L.P. Oleksenko, N.P. Maksymovych, I.P. Matushko. Influence of conditions of Pd/SnO_2 nanomaterial formation on properties of hydrogen sensors // Nanoscale Research Letters. – 2017. – Vol. 12 – P. 383. https://doi.org/10.1186/s11671-017-2152-3
4. G. Korotcenkov, V. Brinzari, B.K. Cho. In_2O_3- and SnO_2-based thin film ozone sensors: fundamentals // Journal of Sensors. – 2016. – Vol. 2016. – P. 3816094. https://doi.org/10.1155/2016/3816094
5. M.A. Gordillo, D.K. Panda, S. Saha. Efficient MOF-sensitized solar cells featuring solvothermally grown [100]-oriented pillared porphyrin framework-11 films on ZnO/FTO surfaces // ACS Applied Materials & Interfaces. – 2019. – Vol.11. – No.3. – P. 3196-3206. https://doi.org/10.1021/acsami.8b17807
6. S.Q. Ren, H.Y. Li, C. Lei, C.Q. Li, X.H. Yin, L.L. Wu, W. Li, J.Q. Zhang, W.W. Wang, L.H. Feng. Interface modification to enhance electron extraction by deposition of a ZnMgO buffer on SnO_2-coated FTO in CdTe solar cells // Solar Energy. – 2019. – Vol.177. – P. 545-552. https://doi.org/10.1016/j.solener.2018.11.053
7. M.S. Hossain, K.S. Rahman, M.A. Islam, M. Akhtaruzzaman, H. Misran, M.A. Alghoul, N. Amin. Growth optimization of $Zn_xCd_{1-x}S$ films on ITO and FTO coated glass for alternative buffer application in CdTe thin film solar cells // Optical Materials. – 2018. – Vol. 86. – P. 270-277. https://doi.org/10.1016/j.optmat.2018.09.045
8. A. Cirocka, D. Zarzeczanska, A. Wcislo, J. Ryl, R. Bogdanowicz, B. Finke, T. Ossowski. Tuning of the electrochemical properties of transparent fluorine-doped tin oxide electrodes by microwave pulsed-plasma polymerized allylamine // Electrochimica Acta. – 2019. – Vol. 313. – P. 432-440. https://doi.org/10.1016/j.electacta.2019.05.046
9. M. Mohammadian, S. Rashid-Nadimi, Z. Peimanifard. Fluorine-doped tin oxide/ hematite/ $Ni(OH)_{(2)}$/ Prussian white photoelectrode for use in a visible-light-assisted pseudocapacitor // Journal of Power Sources. – 2019. – Vol. 426. – P. 40-46. https://doi.org/10.1016/j.jpowsour.2019.03.101
10. Van Bui-Thi-Tuyet, C. Cannizzo, C. Legros, M Andrieux., A. Chausse. Modification of fluorine-doped tin oxide surface: Optimization of the electrochemical grafting of diazonium salt // Surfaces and Interfaces. – 2019. – Vol. 15. – P.110-116. https://doi.org/10.1016/j.surfin.2019.01.012
11. H. Hajibabaei, D.J. Little, A. Pandey, D.W. Wang, Z. Mi, T.W. Hamann. Direct deposition of crystalline Ta_3N_5 thin films on FTO for PEC water splitting // ACS Applied Materials & Interfaces. – 2019. – Vol. 11. – No.17 – P. 15457-15466. https://doi.org/10.1021/acsami.8b21194

12. A. Korjenic, K.S. Raja. Electrochemical stability of fluorine doped tin oxide (FTO) coating at different pH conditions // Journal of the Electrochemical Society. – 2019. – Vol. 166. – No.6. – P. 169-184. https://doi.org/10.1149/2.0811906jes

13. Y. Dong, S. Komarneni, N. Wang, W.C. Hu, W.Y. Huang. An in situ anion exchange induced high-performance oxygen evolution reaction catalyst for the pH-near-neutral potassium borate electrolyte // Journal of Materials Chemistry A. – 2019. – V. 7. – No.12. – P. 6995-7005. https://doi.org/10.1039/C8TA11734A

14. X. Zhang, R. Chen, P. Wang, J. Shu, H. Zhang, H. Song, J. Xu, P. Zhang, J. Xu. A soft chemistry-based route to enhanced photoluminescence of terbium ions and tin oxide nanocrystals codoped silica thin films // Applied surface science. – 2018. – Vol. 452. – P. 96-101. https://doi.org/10.1016/j.apsusc.2018.05.002

15. K. Lim, P. Choi, S. Kim, H. Kim, M. Kim, J. Lee, Yo. Hyeon, K. Koo, D. Choi. Optimization of the solution-based indium-zinc oxide/zinc-tin oxide channel layer for thin-film transistors // Journal of nanoscience and nanotechnology. – 2018. – Vol.18. – No.9. – P. 5913-5918. https://doi.org/10.1166/jnn.2018.15596

16. T.K. Kim, Y. J. Yoon, S. K. Oh, Yu.-J.Cha, I.Ye. Hong, M. U. Cho, Ch.-H. Hong, H. K. Choi, J. S. Kwak. Opposite behavior of multilayer graphene/indium-tin-oxide p-electrode for gallium nitride based-light emitting diodes depending on thickness of indium-tin-oxide layer // Journal of nanoscience and nanotechnology. – 2018. – Vol.18. – No.9. – P. 6106-6111. https://doi.org/10.1166/jnn.2018.15603

17. K. Nomura. Magnetic properties and oxygen defects of dilute metal doped tin oxide based semiconductor // Croat. Chem. Acta. – 2015. – Vol. 88. – № 4. – P. 579–590. https://doi.org/10.5562/cca2784

18. E.A. Dmitrieva, D.M. Mukhamedshina, K.A. Mit', N.B. Beisenkhanov. The effect of NH_4F and NH_4OH on the structure and physical properties of thin SnO_2 films synthesized by the sol-gel method //Glass physics and chemistry. – 2014. – Vol.40. – P. 31-36. https://doi.org/10.1134/S1087659614010076

19. B.N. Mukashev, S.Zh. Tokmoldin, N.B. Beisenkhanov, S.M. Kikkarin, I.V. Valitova, V.B. Glazman, A.B. Aimagambetov, E.A. Dmitriyeva, B.M. Veremenithev. Influence of structure changes of oxide films on their physical properties // Materials Science and Engineering. – 2005. – Vol. 118. – P. 164-169. https://doi.org/10.1016/j.mseb.2004.12.074

20. D.M. Mukhamedshina, N.B. Beisenkhanov, K.A. Mit, V.A. Botvin, I.V. Valitova, E.A. Dmitrieva. Influence of plasma treatments on the properties in SnO_x thin films // Journal of High Temperature Material Processes, An International Quarterly of High Technology Plasma Processes. – 2006. – Vol.10. – No.4. – P. 603-616. https://doi.org/10.1615/HighTempMatProc.v10.i4.110

21. R. Gheonea, C. Mak, E. C. Crasmareanu, V. Simulescu, N. Plesu, G. Ilia. Surface modification of SnO_2 with phosphonic acids // Journal of Chemistry. – 2017. – Vol. 2017. – P. 2105938. https://doi.org/10.1155/2017/2105938

Funded by Al-Farabi KazNU

Physical Sciences and Technology. Vol. 9 (No. 3-4), 2022: 45-58

IRSTI 58.35.06 https://doi.org/10.26577/phst.2022.v9.i2.07

Standard model and predictions for the Higgs boson

E. Boos[1], V. Bunichev[1], G. Nurbakova[2*], N. Khabyl[2],
S. Rustembayeva[2] and S. Imanova[2]

[1] Skobeltsyn Institute of nuclear physics, Lomonosov Moscow State University, Moscow, Russia
[2] Al-Farabi Kazakh National University, Almaty, Kazakhstan
*e-mail: g.nurbakova@gmail.com,

(Received 10 August 2022; received in revised form 22 September; accepted 5 November 2022)

This article describes the electroweak interactions of the Standard Model (SM) with Brout-Englert-Higgs (BEH) mechanism, the appearance and properties of the Higgs boson. Braut-Engler-Higgs mechanism plays an important role in the Standard Model, which introduce a scalar Higgs field with a non-zero vacuum expectation results from spontaneous symmetry breaking. So, due to the interaction with this field, elementary particles become massive. Here arise electrically neutral quanta associated with the Higgs field, so called Higgs boson, in the same way that there is a quantum associated with the electromagnetic field, i.e., photons. The strong part of the Standard Model, Quantum Chromodynamics, quark mixing Cabibbo–Kobayashi–Maskawa matrix, physics of the neutrino and many other issues were not mentioned in the article. Brout-Englert-Higgs mechanism and associated Higgs boson are important parts of the Standard Model of elementary particles. In this paper we present the full Lagrangian of the Standard Model and a set of theoretical predictions about the Higgs boson before its detection, as well as the current status of the Higgs boson problem.

Keywords: Standard Model, High Energy, Large Hadron Collider, Higgs boson, Higgs mechanism, Spontaneous symmetry breaking.
PACS number: 14.65.–q

1 Introduction

In 2013, a year after the discovery of the Higgs boson [1, 2] at the Large Hadron Collider, the Nobel Prize was awarded. This was an important stage in elementary particle physics. This was an experimentally confirmation of the Braut – Engler – Higgs mechanism of spontaneous symmetry breaking, which was theoretically predicted about half century ago [3, 4]. The Standard Model (SM) of fundamental interactions between elementary particles was finally completed and acquired the status of a standard theory.

SM describes strong, weak and electromagnetic interactions between elementary particles on the basis of gauge theory with SU(3)×SU(2)×U(1) symmetry and by using quantum field theory. According to the SM, there are six quarks and six leptons, which are divided into three generations. They interact with each other by three types of interactions, such as strong interaction, weak interaction and electromagnetic interaction. The forces between interacting particles are described by exchange of corresponding quantum fields such as, gluons, W-and Z-bosons and a photon.

Strong interactions are responsible for the attraction of protons and neutrons and provide the stability of the nuclei themselves. These interactions are short-range with a characteristic radius of action of the order of $10^{-12} - 10^{-13}$ cm, which is the size of the nucleus. Electromagnetic interaction is responsible for the stability of atoms and molecules due to the interaction of positively charged atomic nuclei and negatively charged electrons. The radius of these forces can be very large. We cannot feel it directly, because atoms and molecules as a whole are electrically neutral. Weak interactions are responsible for the decay of a free neutron and the instability of a number of atomic nuclei. This interaction provides nuclear cycles due to which occurs the release of energy on the Sun.

The huge world surrounding us is built only from leptons and quarks of the first generation. Quarks and leptons of other two generations manifest themselves in high-energy cosmic rays or in laboratory conditions at accelerators, colliders. Six quarks and six leptons (and their corresponding antiparticles), as well as vector bosons (photon, gluon, W and Z boson) and the recently discovered Higgs boson construct a set of fundamental particles of the SM.

2 Standard Model

The SM of particle physics provides a successful description of all current experimental data and shows a unified picture of the elementary particles, and the interactions between them. In the SM electromagnetic interaction between quarks and leptons are carried out by the exchange of photons, weak interaction between fundamental particles are carried out by the exchange of W and Z bosons, and the strong interaction between quarks are carried out by the exchange of gluons. The standard theory of particle physics with local gauge invariance defined by the $SU_c(3) \times SU_L(2) \times U(1)_Y$ symmetry groups has been experimentally confirmed with high accuracy in lots of experiments. Withal the problem of the origin of all particle masses remained unclear. The exact gauge symmetry $SU_L(2) \times U(1)_Y$ requires the particles be massless. But it is known, for example, that the masses of the W and Z bosons exceed the mass of the proton by almost a hundred times. The elementary particles could be massive only when the gauge symmetry $SU_L(2) \times U(1)_Y$ is broken. From here, scientists have suggested the existence of a self-acting scalar field that fills the entire universe, the so-called Higgs field. Interacting with the vacuum condensate of the Higgs field, the particles become massive. This mechanism of the origin of masses is called “spontaneous” symmetry breaking, all field interactions preserve the gauge symmetry and the Higgs field breaks it. The quanta of the new scalar field, so called Higgs bosons, would be produced in the collision of electron-positron or high-energy proton-antiproton beams.

The SM must satisfy the following requirements:

1. The reproducibility of electromagnetic interactions of leptons and quarks which is invariant under the group of $U(1)_{em}$ transformations.
2. The reproducibility of the axial-vector structure (V-A) of the charged currents of leptons and quarks.
3. The independence of the Lagrangian from the phase of the fields which means the gauge character of the interactions.
4. Renormalizability and unitarity which means that the mass dimension of the operators used in the Lagrangian should be not exceed four.
5. The absence of the chiral anomalies.
6. The possibility of considering all generations of leptons and quarks.
7. The possibility to describe massive fermions and gauge bosons without violation of the local gauge invariance. All fermions (possibly except for one of the neutrinos) and electroweak gauge bosons W, Z are massive particles. To describe the massive fields it was introduced the hypothesis of spontaneous symmetry breaking in which the gauge symmetry of the Lagrangian remains exact while the vacuum of the theory violates this gauge symmetry.

Let take the SM Lagrangian composed of the gauge invariant operators of dimension no higher than 4 as a starting point:

$$L = -\frac{1}{4} W^i_{\mu\nu} (W^{\mu\nu})^i - \frac{1}{4} B_{\mu\nu} B^{\mu\nu} -$$
$$-\frac{1}{4} G^a_{\mu\nu} (G^{\mu\nu})^a + \sum_{f=1,q} \overline{\Psi}^f_L \left(i D^L_\mu \gamma^\mu \right) \Psi^\dagger_L +$$
$$+ \textstyle\sum_{f=1,q} \overline{\Psi}^f_R \left(i D^R_\mu \gamma^\mu \right) \Psi^\dagger_R . \qquad (1)$$

where,

$$W^i_{\mu\nu} = \partial_\mu W^i_\nu - \partial_\nu W^i_\mu + g_2 \varepsilon^{ijk} W^j_\mu W^k_\nu ,$$
$$B_{\mu\nu} = \partial_\mu B_\nu - \partial_\nu B_\mu ,$$

$$G^a_{\mu\nu} = \partial_\mu A^a_\nu - \partial_\nu A^a_\mu + g_s f^{abc} A^b_\mu A^c_\nu , \qquad (2)$$

$$D^L_\mu = \partial_\mu - i g_2 W^i_\mu \tau^i - i g_1 B_\mu \left(\frac{Y^f_L}{2} \right) - i g_s A^a_\mu t^a ,$$
$$D^R_\mu = \partial_\mu - i g_1 B_\mu \left(\frac{Y^f_R}{2} \right) - i g_s A^a_\mu t^a , \qquad (3)$$

here the each indices of *i, j, k* have the values 1, 2, 3 and the indices *a, b, c* have the values 1,...8; $Y^f_{L,R}$ is a weak hypercharge for the left and right fields of the quarks and leptons.

Further, we rewrite the Lagrangian (1) in terms of charged vector fields $W^\pm_\mu = \left(W^1_\mu \mp i W^2_\mu \right) / \sqrt{2}$ and neutral fields W^3_μ and B_μ, which are mixtures of other fields, A_μ and Z_μ with some mixing angle θ_W (Weinberg mixing angle):

$$W_\mu^3 = Z_\mu cos\theta_W + A_\mu sin\theta_W,$$

$$B_\mu = -Z_\mu sin\theta_W + A_\mu cos\theta_W \qquad (4)$$

The interaction Lagrangian for the charged currents (CC) is immediately obtained from (1) and has the desired form (V-A):

$$L_{CC}^l = \frac{g_2}{\sqrt{2}}\bar{\nu}_{e_L}\gamma_\mu W_\mu^+ e_L + h.c. =$$
$$= \frac{g_2}{2\sqrt{2}}\bar{\nu}_e\gamma_\mu(1-\gamma_5)W_\mu^+ e + h.c.,0 \qquad (5)$$

$$L_{CC}^q = \frac{g_2}{2\sqrt{2}}\bar{u}\gamma_\mu(1-\gamma_5)W_\mu^+ d +$$
$$+\frac{g_2}{2\sqrt{2}}\bar{d}\gamma_\mu(1-\gamma_5)W_\mu^- u \qquad (6)$$

For the interaction of neutral currents (NC) according to the requirement 1, it is necessary that one of the fields, let's say A_μ, have the correct electromagnetic interaction like the photon field. This leads to a set of equations for hypercharges that have solutions of the form: $Y_R^e = 2Y_L^e, Y_R^u = \frac{-4}{3}Y_L^e, Y_R^d = \frac{2}{3}Y_L^e$, where the hypercharges are expressed in terms of one independent parameter, for example, the left lepton doublet hypercharge Y_L^e [5]. One of these equations gives the relation between the charges and the mixing angle: $g_2 sin\theta_W = -g_l Y_L^e cos\theta_W$. In this case, the Lagrangian of neutral currents with the fields A_μ and Z_μ takes the following form:

$$L_{NC} = e\sum_f Q_f J_{f\mu}^{em} A^\mu + \frac{e}{4sin\theta_W cos\theta_W}\sum_f J_{f\mu}^Z Z^\mu \qquad (7)$$

where, $J_{f\mu}^{em} = \bar{f}\gamma_\mu f, Q_\nu = 0, Q_e = -1, Q_u = \frac{2}{3}, Q_d = -\frac{1}{3}, J_{f\mu}^Z = \bar{f}\gamma_\mu(\vartheta_f - a_f\gamma_5)f$. As a result, the Lagrangians (5) and (7), which are obtained from the Lagrangian (1), have a structure that demonstrates the next "good" properties of the theory:

1) correct charged currents (V – A);
2) correct electromagnetic interactions;
3) reduction of chiral anomalies;
4) prediction of new neutral currents and new Z_u boson interacting with them.

These currents and the boson are detected experimentally.

However this constructed theory cannot correctly describe the properties of nature. All fields in this theory must be massless. But in nature all charged leptons and quarks, W and Z bosons have nonzero masses. The introduction of the masses into the theory lead to the serious problems. The mass terms for bosons $M_V^2 V_\mu V^{\mu *}$ and the Dirac mass terms for fermions $m_\Psi\bar{\Psi}\Psi = m_\Psi(\bar{\Psi}_L\Psi_R + \bar{\Psi}_R\Psi_L)$ do not satisfy the main requirement of gauge invariance: the mass term for a vector field is not invariant when $V_\mu \rightarrow V_\mu + \partial_\mu\alpha$, and in the mass term of the fermions the left doublet Ψ_L and the right singlet Ψ_R are transform differently on phase rotation.

3 The Brout-Englert-Higgs mechanism of spontaneous symmetry breaking

The Higgs mechanism is used in the framework of the SM to introduce massive vector and fermion fields without violating the basic principle of gauge invariance in field interactions. Let's add to the expression (1) the Lagrangian of a complex scalar field

$$L_\Phi = D_\mu\Phi^\dagger D^\mu\Phi - \mu^2\Phi^\dagger\Phi - \lambda^4(\Phi^\dagger\Phi) \quad (8)$$

which is gauge-invariant for the same group $SU_L(2) \times U_Y(1)$. Here Φ is a complex doublet. Covariant derivative has the following form

$$D_\mu = \partial_\mu - ig_2 W_\mu^i\tau^i - ig_1\frac{Y_h}{2}B_\mu.$$

Here Y_h is hypercharge of the scalar so called Higgs field. The potential of this field shown in Figure 1 has a minimum for negative μ^2:

$$|\varphi_0| = \sqrt{\frac{|\mu^2|}{2\lambda}} = \frac{\vartheta}{\sqrt{2}} > 0.$$

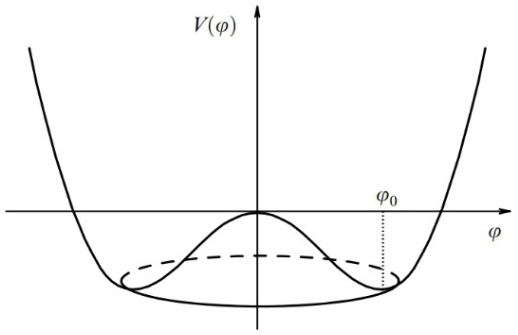

Figure 1 – Potential of the Higgs field

Any particular vacuum solution breaks the symmetry for the phase shift. An arbitrary complex scalar field, which is a doublet of the group $SU_L(2)$, can be parameterized by four real fields:

Since the Lagrangian (8) is invariant under the gauge transformation

$$\Phi(x) \rightarrow \Phi'(x) = \exp\,(ig_2\alpha^i\tau^i)\Phi(x),$$

we write as $g_2\alpha^i(x)$=$\xi^i(x)/\vartheta$, so that all fields $\xi^i(x)$ with the corresponding gauge field transformation disappear from the Lagrangian and only physical degrees of freedom remain in it. In this so called unitary gauge transformation, after substituting the fields $W_\mu^1, W_\mu^2, W_\mu^3$ and B_μ expressed in terms of the fields $W_\mu^\pm, A_\mu, Z_\mu$ and $\Phi(x) = \begin{pmatrix} 0 \\ \frac{\vartheta+h(x)}{\sqrt{2}} \end{pmatrix}$, the Lagrangian L_Φ takes the form

$$L = \frac{1}{2}(\partial_\mu h)^2 - \frac{1}{2}(2\lambda\vartheta^2)h^2 - \lambda\vartheta h^3 - \frac{\lambda}{4}h^4 + \\ + M_W^2 W_\mu^+ W^{\mu-}\left(1+\frac{h}{\vartheta}\right)^2 + \\ + \frac{1}{2}M_Z^2 Z_\mu Z^\mu (1+\frac{h}{\vartheta})^2. \qquad (10)$$

Here we introduce a new field of the new scalar boson (Higgs boson) h(x) with mass $M_h^2 = 2\lambda\vartheta^2$. Also it is included mass terms $M_W = \frac{1}{2}g_2\vartheta$, $M_Z = \frac{1}{2}(g_2 cos\theta_W + g_1 Y_h sin\theta_W)\vartheta$ for the $W_\mu^\pm$ and Z_μ boson fields respectively, as well as the interaction term of the W, Z fields with the Higgs boson and the self-interaction terms of the Higgs boson: h^3 and h^4.

Note that the fields $\xi^i(x)$ in expression (9) are extracted from the Lagrangian by the unitary gauge transformation. However, according to the Goldstone theorem, there must be the existence of 4-1=3 massless bosons. In the gauge theory, these three bosons become the longitudinal components of the vector fields $W^\pm$, Z which from massless with two degrees of freedom become massive with three degrees of freedom. This mechanism of mass production is called the Brout-Englert-Higgs mechanism [3,4]. The Brout-Englert-Higgs mechanism makes it possible to give masses not only to gauge bosons, but also to fermions.

Note the one significant problem of the simplest Higgs SM mechanism: it is unstable for quantum loop corrections to the mass of the Higgs boson itself (the problem of the hierarchy). In Figure 2 it is shown the diagrams contributing to the correction to the mass of the Higgs boson

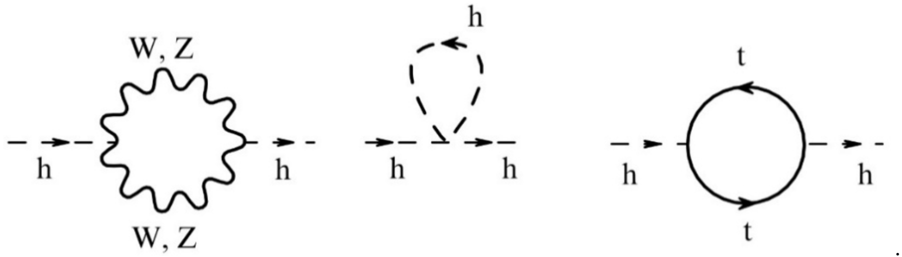

Figure 2 – The diagrams contributing to the mass of the Higgs boson

The correction $\delta M_h^2 = \frac{3G_F}{4\sqrt{2}\pi^2}\left(2M_W^2 + M_Z^2 + M_h^2 - 4M_t^2\right)\Lambda^2 \approx -(0.2\Lambda)^2$ corresponding to these diagrams has square dependence on the scale Λ. The scale Λ related to any "new physics", i.e. any new objects that can contribute to the mass parameter of the Higgs boson. The corrections to the masses of all other SM particles depend on parameter Λ weakly. There is no such symmetry that would forbid such a strong dependence of mass on scale in the case of the scalar Higgs boson. If we require that the corrections to the Higgs boson mass do not exceed the mass itself, $\delta M_h < M_h$, then the limit for Λ would be less than 1 TeV, which is in the contradiction with the data, since none "new physics" has been found on this scale. This difficulty, possibly technical, is called the "problems of small hierarchies." To solve it, something is needed in addition to SM.

4 The Higgs boson predictions.

What did we know about the Higgs boson before its detection? Let's present the Lagrangian of the Higgs sector in the SM where the corresponding boson and fermion parts are present:

$$L_h = \frac{1}{2}(\partial^\mu h)(\partial_\mu h) + \frac{M_h^2}{2}h^2 - \frac{M_h^2}{2\vartheta}h^3 - \\ - \frac{M_h^2}{8\vartheta^2}h^4 + \\ + \left(M_W^2 W_\mu^+ W^{-\mu} + \frac{1}{2}M_Z^2 Z_\mu Z^\mu\right)\left(1 + \frac{h^2}{\vartheta}\right) - \\ - \sum_f m_f \bar{f} f \left(1 + \frac{h}{\vartheta}\right) \qquad (11)$$

In this formula all coupling constants are also expressed in terms of the Higgs boson mass parameter. The values of the masses of W, Z bosons, leptons and quarks are known from experimental data.

In the Lagrangian (11) all parameters were known from the experiment before the Higgs boson discovery, except the mass of the Higgs boson. This circumstance made it possible to carry out various calculations for different mass regions of the Higgs boson and to obtain several quantitative predictions and experimental limitations.

Assumptions for the decay width and production cross sections for various modes. From the Lagrangian (11) it follows the Feynman rules for the interaction of the Higgs boson with $W^\pm$ and Z bosons and fermions, as well as the self-interaction h^3 and h^4 vertices of the Higgs boson. We can calculate the main decay widths and production cross-sections for the Higgs boson by using the Feynman rules and taking into account the higher order strong, and in some cases electroweak corrections [6].

Further we introduce the Feynman diagrams for the main Higgs boson decay modes:

- decays into a fermion and antifermion, $f = \acute{b}, \acute{c}, \tau, \mu$

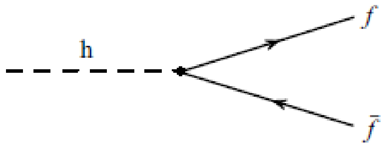

- decays into a real vector bosons W, Z $(M_h > 2M_V)$

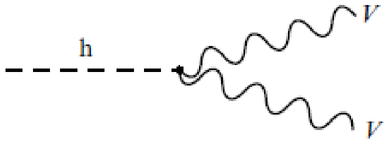

- decays into a real and virtual bosons $(M_V < M_h < 2M_V)$

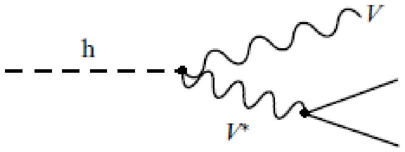

- decays into two virtual bosons $(M_V > M_h)$

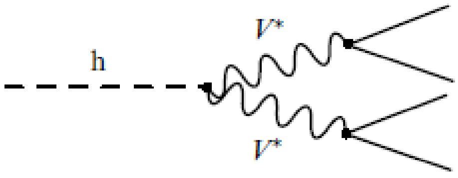

- two gluons decays

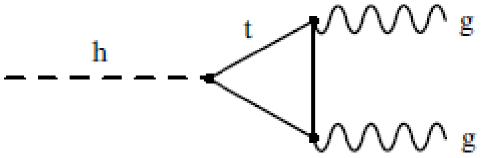

- decays into two photons, photon and Z-boson

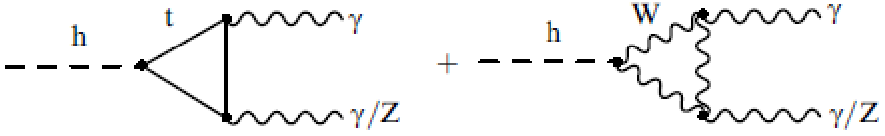

The behaviour of the total width for Higgs boson decays and the partial widths for different modes depending on Higgs boson mass are shown in Figures 3, 4 [6].

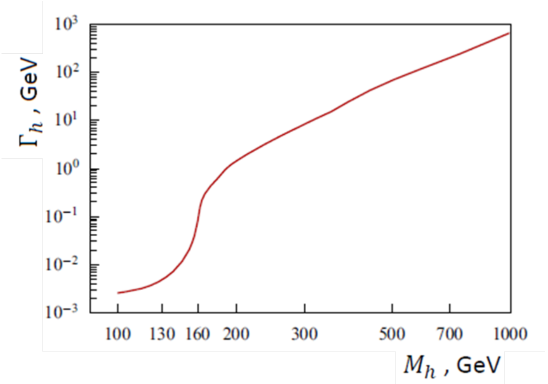

Figure 3 – Dependence of the total Higgs boson decay width Γ_h on its mass M_h [6]

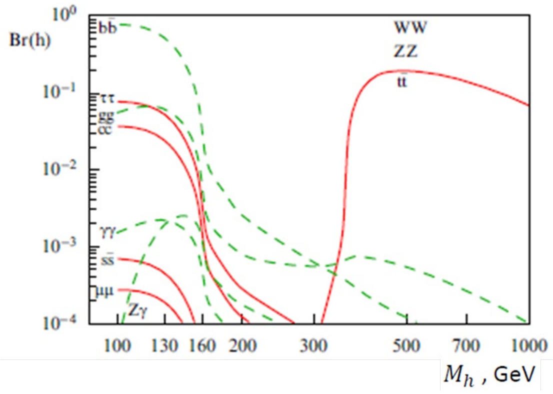

Figure 4 – Partial probabilities of the decay of the Higgs boson through various channels depending on its mass [6]

Limitations from the conditions of unitarity of the SM. The most "dangerous" in terms of energy growth are the amplitudes with participation of the longitudinal components of the W and Z bosons. According to the Brout-Englert-Higgs mechanism these longitudinal components occur from the corresponding Goldstone bosons. Then the scattering amplitudes of two longitudinal components of the W boson can be found from the goldstone boson scattering diagrams:

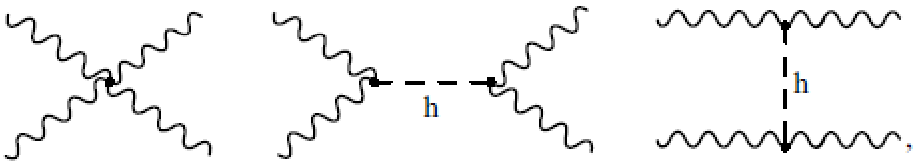

Figure 5 – The goldstone boson scattering diagrams

$$A(W^+W^- \to W^+W^-) =$$
$$= -\left[2\frac{M_h^2}{\vartheta^2} + \left(\frac{M_h^2}{\vartheta}\right)^2 \frac{1}{s-M_h^2} + \left(\frac{M_h^2}{\vartheta}\right)^2 \frac{1}{t-M_h^2}\right]. \quad (12)$$

Hence for the amplitude of the zero partial wave we get

$$a_0 = \frac{1}{16\pi s}\int_s^0 dt|A| = -\frac{M_h^2}{16\pi\vartheta^2}\left[2 + \frac{M_h^2}{s-M_h^2} - \right.$$
$$\left. -\frac{M_h^2}{s}\log\left(1 + \frac{s}{M_h^2}\right)\right]. \quad (13)$$

Then the condition $|Rea_l| < 1/2$ will lead to two possible consequences:

$$a_0 \to -\frac{M_h^2}{8\pi\vartheta^2}, M_h \leq 870GeV$$
$$a_0 \to -\frac{s}{32\pi\vartheta^2}, \sqrt{s} \leq 1.7GeV \quad (14)$$

Therefore, to produce unitarity there should be a Higgs boson with a mass of less than 870 GeV (710 GeV, taking into account all $V_L V_L$ scattering channels), otherwise if $\sqrt{s} \leq 1.7TeV$ $(1.2TeV)$ the SM does not working and something outside the CM must manifest itself to ensure unitarity.

Limitations from the condition of self-consistency of the SM.

Limitations arise from consideration of the equation of the renormalization group for the evolution of the self-interaction constant of the Higgs boson

$$\frac{d\lambda}{dlnQ^2} \simeq \frac{1}{16\pi^2}\left\{12\lambda^2 + 6\lambda\lambda_t^2 - 3\lambda_t^4 - \frac{3}{2}\lambda(3g_2^2 + g_1^2) + \right.$$
$$\left. + \frac{3}{16}[2g_2^4 + (g_2^2 + g_1^2)^2]\right\}$$

where $\lambda_t = m_t/v$ is Yukawa coupling constant for top quark and the relation between λ and M_h is $M_h^2 = 2\lambda v^2$ [7].

Limitations from direct searches on colliders. Direct limitations for the Higgs boson mass M_h were obtained on colliders Tevatron and LEP, before the start of the LHC. The LEP studied the process with the Higgs boson emission (the process is called Higgs strahlung):

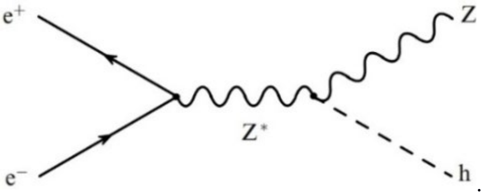

Figure 6 – The Higgs emission process

and obtained the value $M_h > 114.4$ GeV for lower limit at 95% Confidence Level (CL).

At the Tevatron the Higgs boson mass was excluded in the mass interval $M_h = 160 \div 170GeV$ when studying the process of gluon fusion with the Higgs boson decay into two W-bosons.

Limitations from comparing the loop corrections of the mass with precision measurements. At the Tevatron and LEP colliders a very important limitations are associated with precision measurements of the W boson mass and the top quark mass: $M_W = 80385 \pm 15MeV, M_t = 173.18 \pm 0.56(stat) \pm 0.75(syst)GeV$.

It should be noted that there are loop corrections to the boson masses, which depend (logarithmically) on the Higgs boson mass, as shown in the following diagram

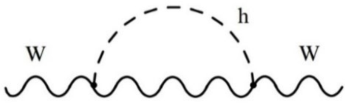

and (quadratically) on the top quark mass, as shown in the next diagram

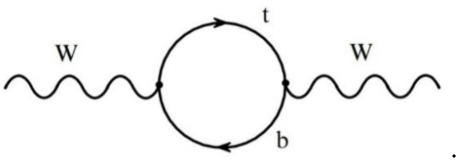

Comparison of these mass shifts and measurement accuracies allows us to establish limitations from above: $M_h < 155GeV, 95\%$ CL.

It should be noted that the comparison of this precision measurements from the Tevatron, LEP and SLC colliders with the results of the SM (taking into account the quantum corrections to the leading approximation) allowed us to demonstrate how well the data were described. These comparisons are shown in Figure 7.

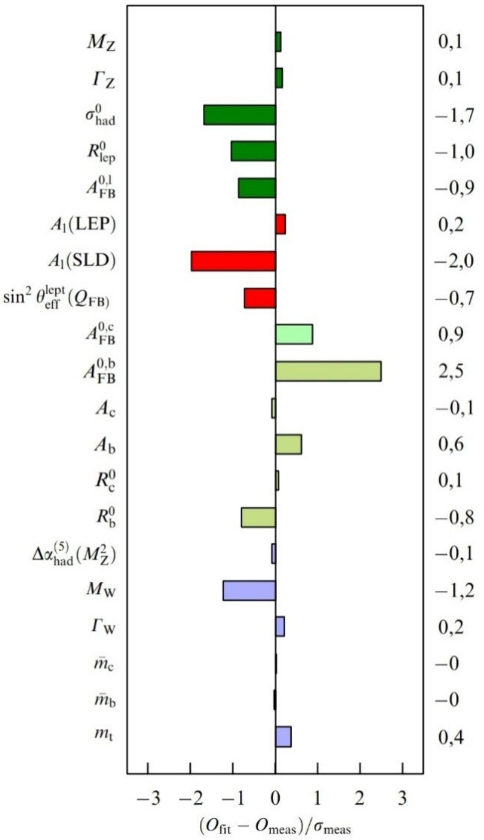

Figure 7 – Global approximation of the precision experimental data for the measurement of some quantities which indicated in the left column of the figure, with the results of calculations of these quantities in the SM taking into account the contribution of loop corrections [8]

5 Higgs boson results

The discovery of the Higgs boson in 2012 completed the SM of elementary particle physics. After that, in the ten years following the discovery, the great progress has been made in painting a clearer portrait of the Higgs boson. The decay rates and production of the Higgs boson were measured using the dataset collected by the CMS and ATLAS experiments during Run 2 of the LHC from 2015 to 2018 [9,10]. The obtained results were in excellent agreement with the Standard Model predictions. All measurements made so far are found to be consistent with the expectations of the SM. In particular, the overall signal-strength parameter has been measured to be $\mu = 1.002 \pm 0.057$ [9]. It has been shown that the Higgs boson directly couples to bottom quarks, tau leptons and muons, which had not been observed at the time of the discovery, and also proven that it is indeed a scalar particle. The CMS experiment is approaching the sensitivity that necessary to probe Higgs boson couplings to charm quarks [11]. The observed (expected) 95% CL value for κ_c is found to be $1.1 < \kappa_c < 5.5$ ($\kappa_c < 3.40$), the most stringent result so far.

In different scenarios, the couplings of the Higgs boson to the three heaviest fermions, the top quark, the *b* quark and the *τ* lepton, were measured with uncertainties ranging from about 7% to 12% and the couplings to the weak bosons (Z and W) were measured with uncertainties of about 5% [10]. A comprehensive study of Higgs boson production kinematics was performed and the results were also was in good agreement with the Standard Model predictions.

With the Run 2 data, CMS has observed the decay of the Higgs boson into a pair of τ leptons with a significance of 5.9 s.d. [12], the ttH production mode at 5.2 s.d. [13]. The Higgs boson has also been seen in its decays into muons with a significance of 3 s.d. [14]. In the analyses of the decay channels H → γγ and H→ZZ→4*l* the Higgs boson mass had been measured to be 125.38 ± 0.14 GeV [15]. The width of the Higgs boson had been extracted and was found to be $\Gamma_H = 3.2^{+2.4}_{-1.7}$ MeV by using off-mass-shell and on-mass-shell Higgs boson production [16]. On-mass-shell refers to a particle with its physical mass, and off-mass-shell refers to a virtual particle.

Studies of on-shell and off-shell Higgs boson production in the four-lepton final state are presented in Ref. [17], using data from the CMS experiment (LHC) with the integrated luminosity of 80.2 fb^{-1} and center-of-mass energy of 13 TeV. Kinematic information from the decay particles and the associated jets are combined using matrix element techniques to identify the production mechanism and increase sensitivity to the H boson couplings in both production and decay. The constraints on anomalous HVV couplings were found to be consistent with the Standard Model expectation in both on-shell and off-shell regions. Under the assumption of a coupling structure similar to that in the Standard Model, the H boson width is constrained to be $3.2^{+2.8}_{-2.2}$ MeV while the expected constraint based on simulation is $4.1^{+5.0}_{-4.0}$ MeV.

Measurements of the Higgs boson mass in the diphoton decay mode at the LHC, with the 35.9 fb^{-1} and $\sqrt{s} = 13$ TeV data collected in 2016 was described in Ref. [18]. Although the branching fraction of the diphoton $H \to \gamma\gamma$ decay channel is significantly small (≈0.23%), it provides a clean final state topology in which the diphoton invariant mass can be reconstructed with high precision.

A new method for estimating the systematic uncertainty associated with changes in the transparency of crystals in an electromagnetic calorimeter during radiation damage was also used. The value of the mass of the Higgs boson in the diphoton decay mode was found to be $m_H = 125.78 \pm 0.26$ GeV. This measurement had been combined with a recent result of the CMS of the same magnitude in $H \to ZZ \to 4l$ decay channel [19] to yield $m_H = 125.46 \pm 0.16$ GeV. Currently this is the most precise measurement of the mass of the Higgs boson.

The conclusions from the work done are the following: during Run 2 of the LHC the experimental collaborations started to employ the combined data for precision measurements of Higgs properties, such as mass, width, couplings, CP. All main production mechanisms are observed, including $H \to b\bar{b}H$, $t\bar{t}H$, VH and etc. Higgs boson mass m_h was measured with an accuracy of 0.1%. Precisions of cross section and branching ratio measurements in combined channel were down to 8.5% level and had ~6-30% accuracy for measurements of couplings. The absolute value of a width was getting closer to the SM expectations (4.1 MeV). Scientists still need to improve the measurement accuracy. It should be noted that spin, parity, differential distributions were not contradict the SM.

There are strong theoretical motivations to search for CP-violating effects in couplings of the Higgs boson to fermions rather than V bosons. As is well known, the amount of CP violation in the SM encoded in the CP violating phase in the CKM matrix is not enough by about an order of magnitude to explain the matter-antimatter asymmetry in the Universe. In couplings to V bosons, CP-odd contributions may enter via nonrenormalisable higher-order operators that are suppressed by powers of $1/\Lambda^2$ [20-22]. Here Λ is considered as a physics scale beyond the SM. Therefore, we can assume that they will only make a small contribution to the coupling. A renormalisable Higgs-to-fermion coupling that violates the CP-symmetry may occur at tree level. The Yukawa couplings for τ lepton $H\tau\tau$ and t quark Htt are therefore the optimal couplings to study the CP in *pp* collisions [23], and measurements of these two interactions complement each other. Recently, both ATLAS [25] and the CMS [24] collaborations presented first measurements of the CP structure of the Higgs-to-top quarks coupling. The CMS results reject the purely CP-odd hypothesis with a significance of 3.2σ standard deviations, while the ATLAS results reject it with a significance of 3.9σ standard deviations.

The CP-properties of the $H \to \tau\tau$ decay is described in terms of an effective mixing angle $\alpha^{H\tau\tau}$, which is actually equal to 0° in the Standard Model [26]. It turns out that the study of the nonzero parameter $\alpha^{H\tau\tau}$ would directly contradict the SM predictions, and led to models beyond the SM: two-Higgs-doublet model [27], supersymmetry. For instance, according to the minimal supersymmetric model CP violation between the Higgs and fermion is expected to be small. Therefore the measurement of a sizeable mixing angle would be unfavorable for such scenarios. In contrast, the parameter $\alpha^{H\tau\tau}$ can be as large as 27° in the next-to-minimal supersymmetric model [28].

Parameterisation of the Lagrangian for the Yukawa *t* coupling in terms of the coupling strength modifiers k_τ and $\tilde{k}_\tau$ which parameterise the CP-even and CP-odd contributions, respectively [23]:

$$L_Y = \frac{-m_\tau}{v} H\left(k_\tau \bar{\tau}\tau + \tilde{k}_\tau \bar{\tau} i \gamma_5 \tau\right).$$

In this equation, m_τ is the τ lepton mass, τ is the Dirac spinor for the τ lepton fields. The vacuum expectation value of the Higgs field v is taken as 246 GeV. The effective mixing angle $\alpha^{H\tau\tau}$ for the $H\tau\tau$ coupling is defined by the coupling strengths as

$$tan(\alpha^{H\tau\tau}) = \frac{\widetilde{k_\tau}}{k_\tau}$$

while the fractional contribution of the CP-odd coupling $f_{H\tau\tau}^{CP}$ could be obtained from the mixing angle as $f_{H\tau\tau}^{CP} = sin^2(\alpha^{H\tau\tau})$. A mixing angle of $\alpha^{H\tau\tau} = 0\ (90)°$ corresponds to a pure scalar (pseudoscalar) coupling. For any other value of the parameter $\alpha^{H\tau\tau}$, the Higgs boson has a mixed coupling with CP-even and CP-odd components, where the maximum mixing occurs at ±45°.

ϕ_{CP} denotes the angle between two planes, where occur two τ-lepton decays in the rest frame of the Higgs boson. An illustration of the decay planes is shown in Figure 8. The relation between $\alpha^{H\tau\tau}$ and ϕ_{CP} can be derived as follows

$$\frac{d\Gamma}{d\phi_{CP}}(H \to \tau^+\tau^-) \sim 1 - b(E^+)b(E^-)\frac{\pi^2}{16}\cos\left(\phi_{CP} + 2\alpha^{H\tau\tau}\right).$$

In this equation, the energies of outgoing charged particles denoted by E^- and E^+ in their respective rest frames. The b functions are spectral functions that account the correlation between the τ-lepton spin and the momentum of the emitted charged particle.

In Figure 9 it is illustrated the normalized distribution of ϕ_{CP} for the pseudoscalar, scalar and maximally mixed values of $\alpha^{H\tau\tau}$, as well as the ϕ_{CP} distribution from Drell–Yan processes. Calculations was done in the rest frame of the Higgs boson.

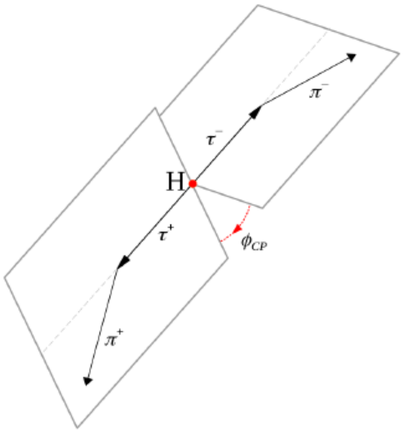

Figure 8 – The illustration of two τ lepton decay planes in the H rest frame.
ϕ_{CP} denote the angle between this decay planes

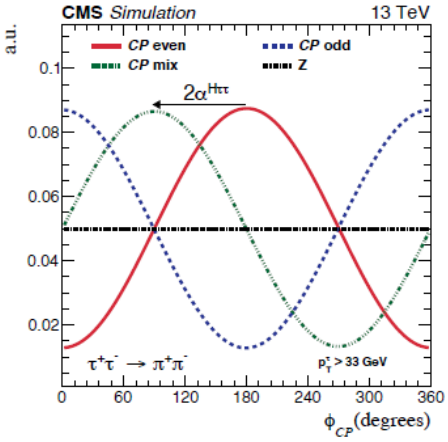

Figure 9 – The normalised distribution of ϕ_{CP} between the τ lepton decay planes in the rest frame of the Higgs boson at the generator level, for both τ leptons decaying to a charged pion and a neutrino. The distributions are for a decaying scalar (CP-even, solid red), pseudoscalar (CP-odd, dash blue), a maximal mixing angle of 45° (CP-mix, dash-dot-dot green), and a Z vector boson (black dashdot). The transverse momentum of the visible *t* decay products p*t* T was required to be larger than 33 GeV during the event generation

Results for the $\alpha^{H\tau\tau}$ mixing angle: the observed and expected negative log-likelihood scan for the combination of channels $\tau_e\tau_h$, $\tau_\mu\tau_h$, and $\tau_h\tau_h$ was presented in Figure 10. The results disfavoured the pure CP-odd scenario at 3.0σ and expected exception assuming the SM Higgs boson is 2.6σ.

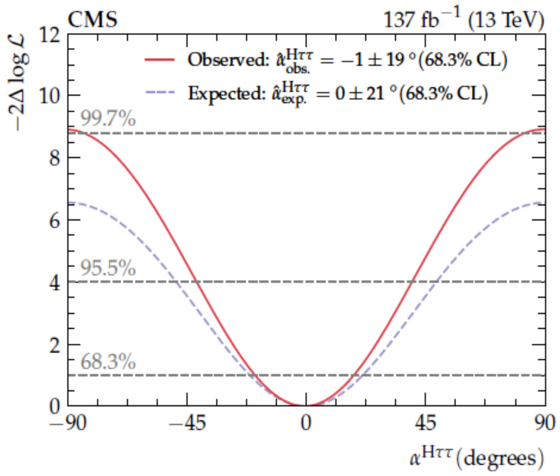

Figure 10 – Negative log-likelihood scan for the combination of the $\tau_e\tau_h$, $\tau_\mu\tau_h$, and $\tau_h\tau_h$ channels. The observed (expected) sensitivity to distinguish between the scalar and pseudoscalar hypotheses, determined at $\alpha^{H\tau\tau} = 0$ and ±90°, respectively is 3.0*s* (2.6*s*). The observed (expected) value for $\alpha^{H\tau\tau}$ is -1±19° (0±21°) at the 68.3% CL. The observed range is ±41° (±49°) at 95.5% CL and ±84°at the 99.7% CL

The first measurement of the CP structure of the Yukawa coupling between the Higgs boson and τ lepton is presented In Ref. [29]. The measurement was based on data collected in $p\bar{p}$ collisions at $\sqrt{s}$ = 13 TeV by the CMS experiment at the LHC, with the integrated luminosity of 137 fb^{-1}. The analysis uses the angular correlation between the decay planes of τ leptons produced in Higgs boson decay. It is found that the observed effective mixing angle is -1±19°, while the expected value is 0±21° at a confidence level of 68.3%. The observed uncertainty found to be ±41° and expected uncertainty is ±49° at the 95.5% CL, and the observed sensitivity at the 99.7% confidence level is ±84°. The main uncertainty in the measurement is statistical, which means that the accuracy of the measurement will increase as more collision data is accumulated. The result is consistent with the predictions of the SM and reduces the allowed parameter space for its extensions.

In Ref. [30] it was studied the decay of the Higgs boson into four leptons via a virtual W-boson or Z-boson pair. This decay channel is one of the most important decay modes in the search for the Higgs boson at the LHC. Partial decay widths of the *H* ⟶ *4 leptons* decays are given in Table 1 for various Higgs masses and various decay channels. The data includes the O(α) and O($G^2_\mu M^4_H$) corrections and the corresponding relative corrections. The channel $\nu_e e^+\mu^-\tilde{\nu}_\mu$ results from the decay *H* ⟶ *WW* ⟶ *4 leptons*, while the last channel $\nu_l l^+ l \tilde{\nu}_l$ receives contributions from both the decay into *W* and into *Z* bosons. The larger the Higgs mass, the larger is the decay width.

Table 1 – Descriptions of the distribution of the Higgs boson [30]

	M_H(GeV)	140		170		200	
	Γ_W(GeV)	2.09052…		2.09054…		2.09055…	
	Γ_Z(GeV)	2.50278…		2.50287…		2.50292…	
H⟶		Γ[MeV]	δ[%]	Γ[MeV]	δ[%]	Γ[MeV]	δ[%]
$e^-e^+\mu^-\mu^+$	corrected lowest order	0.0012628(5) 0.0012349(4)	2.1	0.020162(7) 0.019624(5)	2.7	0.8202(2) 0.78547(8)	4.4
$l^-l^+l^-l^+$ l=e,μ	corrected lowest order	0.0006692(2) 0.0006555(2)	2.3	0.010346(3) 0.010074(2)	2.7	0.41019(8) 0.39286(4)	4.4
$\nu_e e^+\mu^-\tilde{\nu}_\mu$	corrected lowest order	0.04807(2) 0.04638(1)	3.7	4.3109(9) 4.0610(7)	6.2	12.499(3) 11.907(2)	5.0
$\nu_l l^+ l \tilde{\nu}_l$ l=e,μ	corrected lowest order	0.04914(2) 0.04738(2)	3.7	4.344(1) 4.0926(8)	6.1	14.133(3) 13.458(2)	5.0

because the available phase space grows. The corrections to partial decay widths typically amount to some per cent and increase with growing Higgs mass M_H, reaching about 8% at $M_H \sim 500$GeV. For not too large Higgs masses ($M_H \lesssim 400$GeV) the corrections to the partial decay widths can be reproduced within ≲2% by simple approximations. The decays of the Higgs boson into 4 leptons via a W-boson or Z-boson pair lead to experimental signatures at the LHC that are important for studying the Higgs boson and its properties.

6 Conclusion

The SM predictions for different observables, such as widths and partial decay probabilities, various asymmetries, kinematic distributions, cross-sections of processes are in excellent agreement with experimental data. There are 18 free parameters in the SM:

- four parameters in the electroweak and Higgs sector: g_1, g_2, μ^2, λ. This parameters are expressed in terms of parameters $\alpha_{em} = \frac{e^2}{4\pi}, sin\theta_W, M_Z, M_h$, which are measured in high accuracy;
- six quark masses and three charged lepton masses;
- in the Cabibbo-Kobayashi-Maskawa mixing matrix there are three angles and one phase;
- $\alpha_{QCD} = \frac{g_s^2}{4\pi}$ is the coupling constant of strong interactions.

The Higgs boson has been discovered and significant differences from the predictions of the Standard Model are not yet visible, but the physical characteristics of the Higgs boson is still to be studied in great detail. This is what physicists will continue to do at the LHC and at future high-energy colliders. In the new Run at LHC, a beam of protons appeared with a collision energy of up to 13.6 TeV, in addition, the luminosity, i.e. number of collisions have been increased. As expected, detectors will be able to see significantly more Higgs boson production events, which means physicists will be able to study its properties in more detail and subject the Standard Model to even more rigorous tests. Run 3 will last approximately 3 years, after which the Large Hadron Collider will be radically upgraded to become the HL-LHC (High Luminosity Large Hadron Collider).

Also in the coming years, physicists must decide in which direction to develop particle physics in the near future. The LHC will be replaced by a new generation collider, and most likely it will be one of the variants of the Higgs factory – the electron-positron collider (FCC), optimized for the study of the Higgs boson. As a result of the work of the LHC and the Higgs factory, the measurement accuracy of many decays of the Higgs boson will improve to a few percent. If the properties of the Higgs boson differ from the Standard Model by even a few percent, this will be noticeable, and thus a new chapter in the study of the micro-world will open.

Let us note one more new generation project for further study of the Higgs sector and search for new physics beyond the SM. Such a project is the International Linear Collider (ILC), which proposes to collide e^+e^- at energies of 250 GeV and higher. The fundamental difference from the LHC is that leptons collide in the ILC, which makes the events cleaner to interpret. It is planned to install two conceptually different detectors at the ILC collider: ILD (International Large Detector) and SiD (Silicon Detector). Both detectors will have record-breaking accuracy in measuring the jet momentum and energies.

Acknowledgements

This work was supported by the Ministry of Education and Science of the Republic of Kazakhstan, Grant IRN AP09058640 “Physics beyond the Standard Model in processes involving the top quark and Higgs boson”.

The article is dedicated to the tenth anniversary of the discovery of the Higgs boson.

References

1. G.Aad, T.Abajyan, B.Abbott, J.Abdallah, S.Abdel Khalek, A.A.Abdelalim, O.Abdinov, R.Aben, B.Abi, M.Abolins, O.S.Abou Zeid, H.Abramowicz, H.Abreu, B.S.Acharya, L.Adamczyk, D.L.Adams, T.N.Addy, L.Zwalinski. Observation of a new particle in the search for the Standard Model Higgs boson with the ATLAS detector at the LHC // Physics Letters B. – 2012. –V.716. – P.29 https://doi.org/10.1016/j.physletb.2012.08.020

2. S.Chatrchyan, V.Khachatryan, A.M.Sirunyan, A.Tumasyan, W.Adam, E.Aguilo, T.Bergauer, M.Dragicevic, J.Erö, C.Fabjan, M.Friedl, R.Frühwirth, V.M.Ghete, J.Hammer, M.Hoch, N.Hörmann, J.Hrubec, D.Wenman. Observation of a new boson at a mass of 125 GeV with the CMS experiment at the LHC // Physics Letters B. – 2012. –V.716. – P. 31

https://doi.org/10.1016/j.physletb.2012.08.021

3. F.Englert, R.Brout. Broken Symmetry and the Mass of Gauge Vector Mesons // Phys. Rev. Lett. – 1964. – V. 13. No.321 https://doi.org/10.1103/PhysRevLett.13.321

4. Peter W. Higgs. Broken Symmetries and the Masses of Gauge Bosons // Phys. Rev. Lett. – 1964. –V. 13. No.508 https://doi.org/10.1103/PhysRevLett.13.508

5. E.Boos. Field theory and the electro-weak Standard Model // European School of High-Energy Physics. – 2013. – V. 5. – P.64 10.5170/CERN-2015-004.1

6. A. Djouadi. The Anatomy of Electro-Weak Symmetry Breaking. I: The Higgs boson in the Standard Model // Phys. Rep. – 2008 –V.457. No.1
https://doi.org/10.48550/arXiv.hep-ph/0503172

7. L.Basso, O.Fischer, J.J. van der Bij. A renormalization group analysis of the Hill model and its HEIDI extension // Physics Letters B. – 2014 – V. 730. – P.5 doi.org/10.1016/j.physletb.2014.01.06

8. M. Baak. Study of the inclusive production of charged pions, kaons, and protons in pp collisions at sqrt(s) = 0.9, 2.76, and 7 TeV // Eur. Phys. C. – 2012. – V. 72. – P.42
https://doi.org/10.1140/epjc/s10052-012-2164-1

9. The CMS Collaboration. A portrait of the Higgs boson by the CMS experiment ten years after the discovery // Nature. – 2022 . –V. 607. – P. 8 https://doi.org/10.1038/s41586-022-04892-x

10. The ATLAS Collaboration. A detailed map of Higgs boson interactions by the ATLAS experiment ten years after the discovery. // Nature. – 2022. –V. 607. – P. 7.
https://doi.org/10.17182/hepdata.130266

11. The CMS Collaboration. Search for Higgs boson decay to a charm quark–antiquark pair in proton–proton collisions at s = 13 TeV // Preprint at arXiv:2205.05550. – 2022. –V. 1. – P.16
https://doi.org/10.48550/arXiv.2205.05550

12. The CMS Collaboration. Observation of the Higgs boson decay to a pair of τ leptons with the CMS detector // Phys. Lett. B. – 2018. –V.779. – P.33
https://doi.org/10.1016/j.physletb.2018.02.004

13. A. M. Sirunyan et al. Observation of production ttH // Phys. Rev. Let. – 2018. – V.120. –P.231801 https://doi.org/10.1103/PhysRevLett.120.231801

14. The CMS Collaboration. Evidence for Higgs boson decay to a pair of muons // J. High Energy Phys. – 2021. – V. 01.148. –P.62 https://doi.org/10.1007/JHEP01%282021%29148

15. The CMS Collaboration. A measurement of the Higgs boson mass in the diphoton decay channel // Phys. Lett. B. – 2020. – V.805. – P. 135425
https://doi.org/10.1016/j.physletb.2020.135425

16. The CMS Collaboration. Measurement of the Higgs boson width and evidence of its off-shell contributions to ZZ production // Nat. Phys. – 2022. – V. 1050. – No.20
https://doi.org/10.1038/s41567-022-01682-0

17. The CMS Collaboration. Measurements of the Higgs boson width and anomalous HVV couplings from on-shell and off-shell production in the four-lepton final state // Phys. Rev. D –2019. – V.99. – P.51 https://doi.org/10.1103/PhysRevD.99.112003

18. The CMS Collaboration. A measurement of the Higgs boson mass in the diphoton decay channel // Phys. Lett. B. – 2020. – V.805. – P.35 https://doi.org/10.1016/j.physletb.2020.135425

19. CMS Collaboration. Measurements of properties of the Higgs boson decaying into the four-lepton final state in pp collisions at $\sqrt{s}$ = 13 TeV // JHEP – 2017 – V.11. – P.51 https://doi.org/10.1007/JHEP11%282017%29047

20. C. Zhang and S.Willenbrock. Effective-field-theory approach to top-quark production and decay // Phys. Rev. D – 2011 – V.83. – P.24 https://doi.org/10.1103/PhysRevD.83.034006

21. R. Harnik et al. Measuring CP violation in $H \to \tau^+ \tau^-$ at colliders // Phys. Rev. D – 2013. – V.88. – P.12 https://doi.org/10.1103/PhysRevD.88.076009

22. T. Ghosh, R. Godbole, X. Tata. Determining the spacetime structure of bottom-quark couplings to spin-zero particles // Phys. Rev. D – 2019. – V.100. – P.12
https://doi.org/10.1103/PhysRevD.100.015026

23. A. V. Gritsan, R. Rontsch, M. Schulze, M. Xiao. Constraining anomalous Higgs boson couplings to the heavy-flavor fermions using matrix element techniques // Phys. Rev. D – 2016 – V.94 – P.21 https://doi.org/10.1103/PhysRevD.94.055023

24. The CMS Collaboration. Measurements of ttH production and the CP structure of the Yukawa interaction between the Higgs boson and top quark in the diphoton decay channel // Phys. Rev. Lett. – 2020 – V.125. – P.31 https://doi.org/10.1103/PhysRevLett.125.061801

25. The ATLAS Collaboration. CP properties of Higgs boson interactions with top quarks in the ttH and tH processes using H → gg with the ATLAS detector // Phys. Rev. Lett. – 2020 – V.125. – P. 21 https://doi.org/10.1103/PhysRevLett.125.061802

26. The ATLAS Collaboration. Constraints on Higgs boson properties using $WW^{*}(\rightarrow e\nu\mu\nu)jj$ production in 36.1 fb−1 of s√=13 TeV pp collisions with the ATLAS detector // Eur. Phys. J. C. – 2022 – V.82. – P.46 https://doi.org/10.1140/epjc/s10052-022-10366-1

27. D. Fontes, J. C. Romao, R. Santos, J. P. Silva. Large pseudoscalar Yukawa couplings in the complex 2HDM // JHEP –2015 – V.06. – P.21 https://doi.org/10.48550/arXiv.1502.01720

28. S. F. King, M. Muhlleitner, R. Nevzorov, K.Walz. Exploring the CP-violating NMSSM: EDM constraints and phenomenology // Nucl. Phys. B – 2015 – V.901. – P.32

https://doi.org/10.1016/j.nuclphysb.2015.11.003

29. The CMS Collaboration. Analysis of the CP structure of the Yukawa coupling between the Higgs boson and τ leptons in proton-proton collisions at √ s = 13 TeV // –2022 –V.06. – P.64

https://doi.org/10.1007/JHEP06%282022%29012

30. A. Bredenstein, A. Denner, S. Dittmaier, M.M. Weber. Precise predictions for the Higgs-boson decay H → W W/Z Z →4 leptons // Phys.Rev. D –2006 –V.74. – P.42

https://doi.org/10.1103/PhysRevD.74.013004

Funded by Al-Farabi KazNU

Physical Sciences and Technology. Vol. 9 (No. 3-4), 2022: 59-68

IRSTI 67.09.45 https://doi.org/10.26577/phst.2022.v9.i2.08

The impact of technological parameters of the torch to physical and chemical properties of a gas-thermal burner for spraying ultra-high molecular weight polyethylene

M.K. Skakov[1], I. A. Ocheredko[2],
M. B. Bayandinova[2,*] and B.T. Tuyakbaev[2]

[1]The Republican State Enterprise «National Nuclear Center of the Republic of Kazakhstan»
of the Ministry of Energy of the Republic of Kazakhstan, Kurchatov, Kazakhstan
[2]Sarsen Amanzholov East Kazakhstan University, Ust-kamenogorsk, Kazakhstan
*e-mail:shohmanova_m@mail.ru

(Received 28 June 2022; received in revised form 24 September; accepted 18 October 2022)

The values of the heat flux density, transverse and longitudinal temperature gradients of the gas-thermal burner torch, the type of reaction during the combustion in various modes (reducing, neutral, oxidizing) depending on the mass fractions of the fuel and oxidizer burning have been determined in this paper. The significant role of the torch temperature as one of the most important parameters determining the quality of polymer coatings obtained by the gas-thermal method has been established. A spatial model of a gas-thermal burner has been designed, which allows to obtain thermal modes at specified technological parameters. A physical model of the interactions "torch-polymer particle", "thermal jet – base" has been developed. The necessary density of the torch heat flux for the complete melting of ultrahigh molecular weight polyethylene (UHMWPE) particles not exceeding the temperature threshold of destruction has been determined. The required rate of introduction the UHMWPE powders into the burner flame has been also determined. Based on the calculations of the "torch-polymer particle interaction", the optimal geometry of the torch, the particles trajectory in the torch and the spraying distances have been determined.

Keywords: gas-thermal spraying, ultra-high molecular weight polyethylene, High-Velocity Air-Fuel technology, finite element method, destruction.
PACS numbers: 07.20.−n, 44.90.+c.

1 Introduction

A method of applying polymer coatings to the surface of metal products by gas-thermal spraying in protection purposes is proposed in a number of works [1-5]. The method eliminates the necessity of using volatile organic solvents under hazardous production conditions. However, the proposed method and equipment for the gas thermal spraying has significant drawbacks including low productivity; the heat transfer in the "torch – polymer particle", "thermal jet-base" systems have not been investigated. In our opinion, the systematic studies have also not been carried out to determine the efficient composition of the combustible mixture and granulation of the applied polymer material. In addition, the method is not optimized for the criteria of industrial applicability.

In the result, there are still no unifired recommendations for choosing the optimal value of the heat flow density of the thermal sprayer torch, modes of melting polymer coatings on long-length parts. Moreover, from a technological point of view, the problems of controlling the geometric dimensions of the applied coatings which in turn depends on the accurate modeling of the spraying process have not been solved.

The unstable technological modes adversely affect, respectively, the practically important properties of the obtained coatings.

The polymer processing has been carried out using plasma energy [6-8]. However, the high temperature developed in the plasma flow results in the polymer destruction. Besides this, the mechanical properties and chemical resistance of coatings are lower than those of the coatings made by other methods.

This greatly limits the scope of the flame spraying method. In addition, a significant disadvantage of the polymer plasma spraying method is the low values of the thermal efficiency, high energy intensity, and the impossibility of its implementation under non-stationary conditions. The plasma method seems to be appropriate only for the processing of refractory polymers, such as fluorolones.

Thus, the purpose of this work is to determine the degree of the parameters of the High-Velocity Air-Fuel (HVAF) method the impact to the physical and chemical properties of the burner torch during the UHMWPE processing.

2 Material and research methods

In order to apply UHMWPE coating in practice, we need to develop and design an experimental high-rate gas-air spraying unit. However, it is necessary to determine beforehand the influence of the technological parameters of the gas-thermal equipment on the physical and chemical properties of the burner torch during the UHMWPE processing. We used 3D modeling methods to solve this problem. Propane was used as a fuel gas, and air was used as an oxidizer (high velocity coating technology – High Velocity Air-Fuel (HVAF). The object of the UHMWPE study, manufactured by Nantong Yangba Polyethylene Co., Ltd., China, the density is 930 kg/m^3, with a molecular weight of $2 \cdot 10^6$ mol^{-1}, is a white powder with an average particle size of 150 microns (Figure 1 a, b), T_{pl} = 135 °C, bulk density >0.4 g/cm^3, $p \geq 0.933$ g/cm^3. The shape and size of UHMWPE particles were determined by optical microscopy on Altami Met 5C. The powder mixing was carried out in a Pulverisette 23 ball mill, rotation speed 1500 rpm, grinding time in the range from 6.5 to 15 minutes.

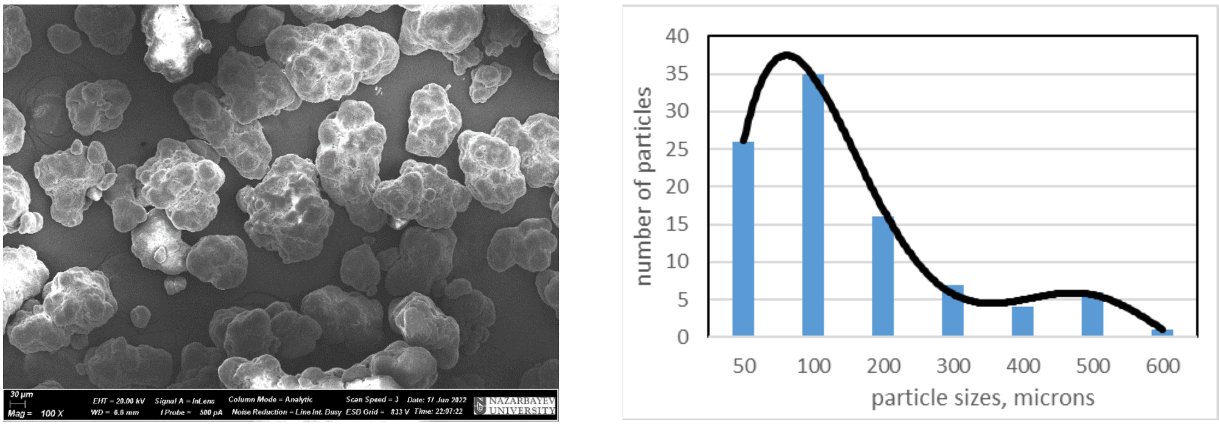

a

b

Figure 1 – Optical image of UHMWPE particles (a), particle size distribution (b)

To study the process of the UHMWPE gas-thermal processing, we have designed a physical model of the system and found optimal solutions by the finite element method (FEM) in accordance with [9,10]. FEM is a numerical method for solving partial differential equations, as well as integral equations arising in solving problems of applied physics. As it is known, FEM is widely used to solve problems of deformable solid mechanics, heat transfer, hydrodynamics, electrodynamics and topological optimization. The domain in which the solution of differential equations is sought is divided into a finite number of subdomains (elements). The type of approximating function is arbitrarily selected in each of the elements.

A spatial model that makes it possible to obtain the thermal modes of the burner torch at the specified technological modes has been designed. The model was designed in the SolidWorks 3D modeling software package according to [11]. The boundary conditions are: heating time of a powder particle is 0.2 s, an average heat flow density is 38 kW/m^2.

3 Results and discussions

3.1 Dependence of the physical and chemical properties of the gas-thermal burner torch on the geometry of the nozzles and the mass fractions of fuel and oxidizer

To determine the dependence of the physical and chemical properties of a gas–thermal burner torch on the geometry of the burner nozzles and the mass fractions of fuel and oxidizer, we designed a 3D model of High-Velocity Air Fuel (HVAF) spraying technology (Figure 2).

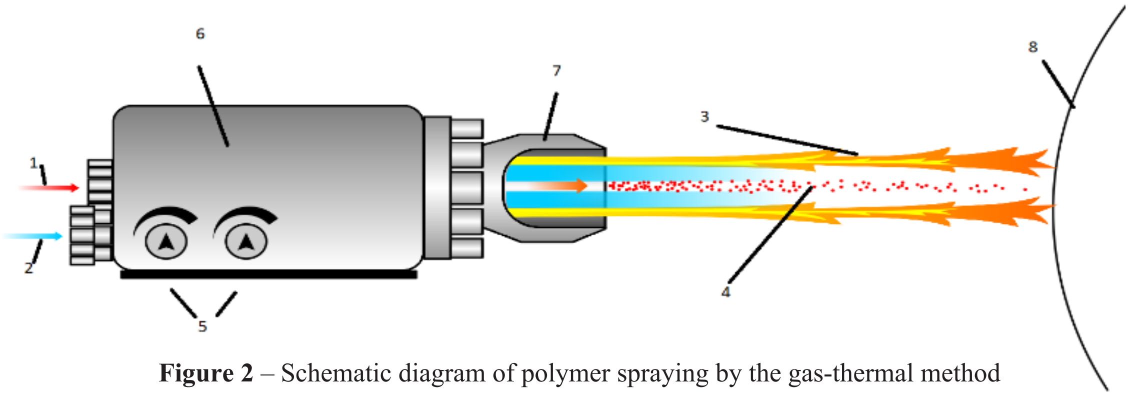

Figure 2 – Schematic diagram of polymer spraying by the gas-thermal method

According to Figure 2, there is a brief description of the technological process: propane 1 enters the gas distribution unit 6, and sprayed through nozzle 7, ignites under the impact of a heat source and forms torch 3; mixture of air and composite charge 2 enters the gas distribution unit and then enters the torch zone through nozzle 7; UHMWPE powders 4 melt under the impact of the temperature and collide with base 8 to form a coating. The ratio of the fuel, oxidizer and working raw materials, i.e. variable technological parameters, are regulated respectively by valves 5. The burner torch must provide the necessary technological mode for the processing of UHMWPE particles. To obtain coatings with the possibility of varying their properties, it is necessary to provide an adjustable temperature gradient of the torch, which can be achieved by changing the geometry of the nozzle and the ratio of fuel and oxidizer.

The most important problem of optimizing the torch burning process is the efficient use of the energy released during the combustion of the combustible mixture. In addition, special attention is paid to the compliance with the spraying temperature mode during the spraying polymer coatings.

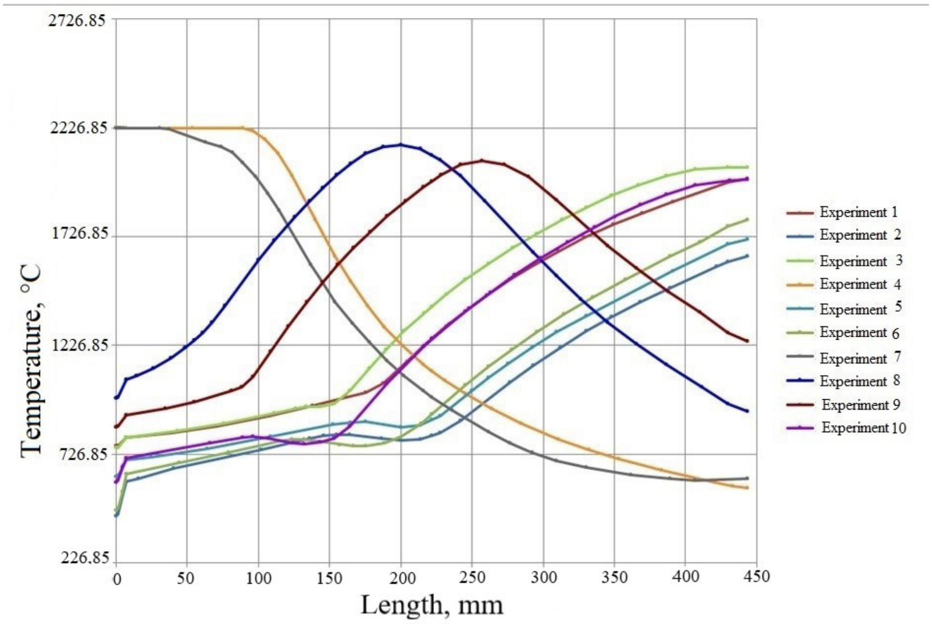

Figure 3 – Dependence of the physical and chemical properties of the torch on the geometry of the nozzles and the mass fractions of the fuel and oxidizer

Figure 3 shows the changes in the physical and chemical properties of the torch depending on the geometry of the nozzles and the mass fractions of the fuel and oxidizer.

Table 1 shows boundary conditions.

It can be seen from the above data, that the temperature distribution along the axes of the torch is sensitive to the ratio of the diameter of the nozzle and the gas flow velocity.

Table 1 – Boundary conditions of the experiment

	Experiment 1	Experiment 2	Experiment 3	Experiment 4	Experiment 5
Jet diameter, mm	0,9	1	1,1	1,2	0,9
Gas consumption (propane)	0,01	0,03	0,05	0,04	0,035
	Experiment 6	Experiment 7	Experiment 8	Experiment 9	Experiment 10
Jet diameter, mm	1	1,1	1,2	0,9	1
Gas consumption (propane)	0,001	0,03	0,01	0,001	0,005

3.2 The dependence of the heat flow density, the temperature gradient of the burner torch, the type of reaction during combustion in various modes on the mass fractions of fuel and oxidizer

According to Figure 2, the ratio of fuel, oxidizer, raw materials (variable technological parameters) is regulated by valves 5

Figure 4 shows the calculated data of the temperature gradient of the gas-thermal burner torch. As can be seen from the diagram, the designed finite element model allows receiving the data at any point in the torch space. Depending on the ratio of the combustible substance and oxygen, the gas flame is divided into [12-14]:

- oxidative – with oxygen excess;
- regular – with a parity ratio of combustible matter and oxygen;
- recovery – with an excess of combustible gas.

The torch flame consists of three components: the neutral zone (red), the recovery zone (green) and oxidizing (light blue color) (Figure 5).

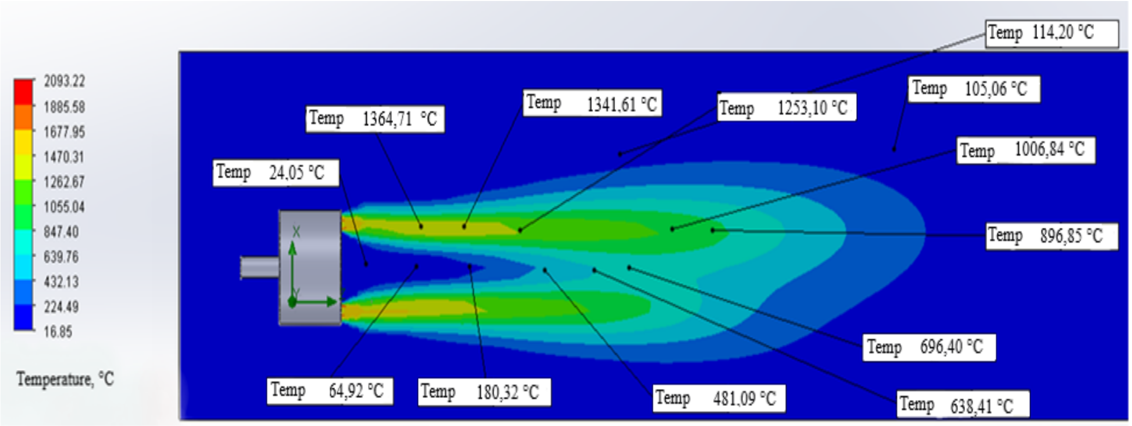

Figure 4 – The torch temperature gradient

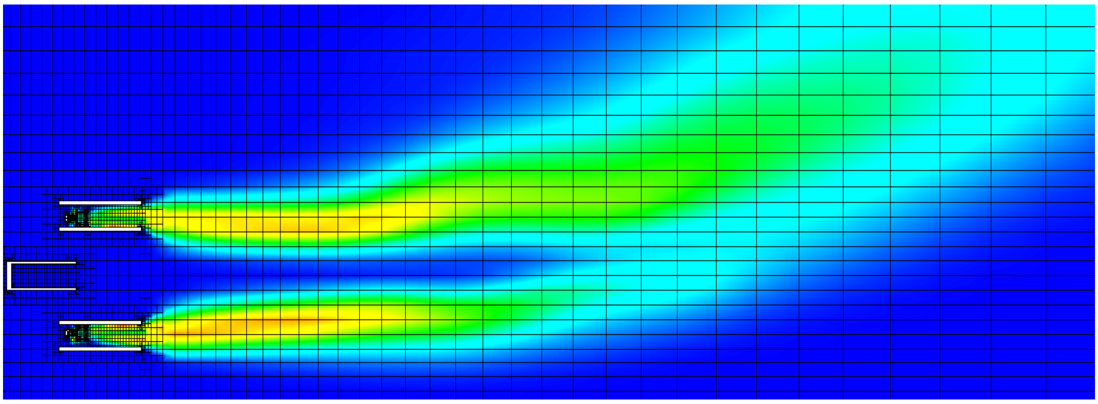

Figure 5 – Colored zones, which show the type of combustion reaction

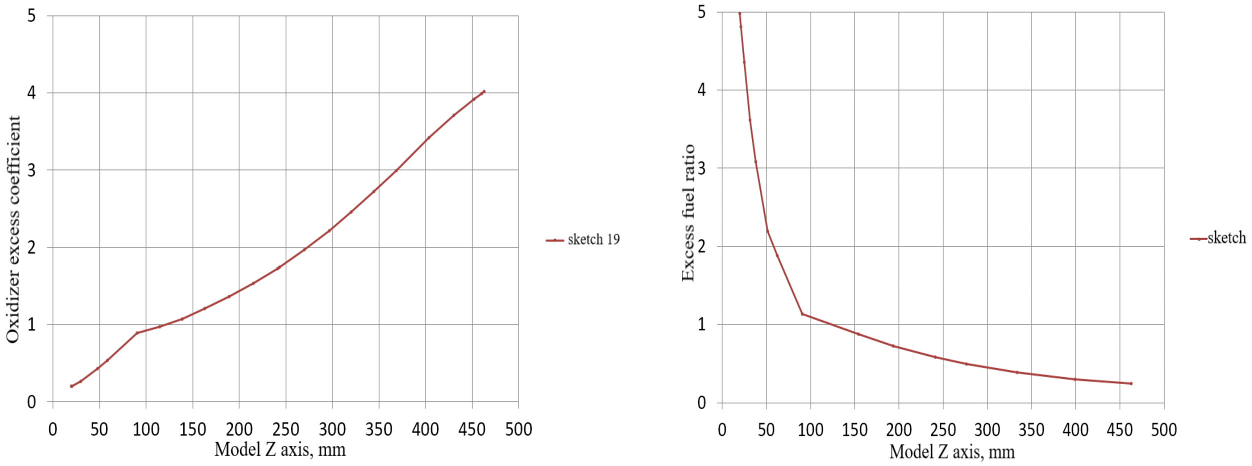

a) b)

Figure 6 – Change in the excess coefficient of oxidizer (a) and fuel (b) along the flame axis

From the data in Figures 5 and 6, it can be seen that the powder is in the area of the oxidizing flame in the melting zone. In [15,16] it is noted that due to thermal oxidation processes, the coatings even from inert polymers, such as polyethylene, have good adhesion. However, too high flame temperature (up to 1500 ° C) in an unstable mode adversely affects the other, practically important properties of coatings. For example, the mechanical properties and chemical resistance of the coatings are lower than that of the coatings made by other methods [17-19].

The heat flow density is an important technological parameter. The determining of the heat flow density is necessary to determine the optimal trajectories of powder particles in the torch. Figure 6 shows a general picture of the distribution of heat flow density along the torch longitudinal axis.

Figure 8 shows the calculated gradient of the heat flow in the particle deposition area. Figures 7 and 8 show the dependence of the heat flow density on the deposition distance. It can be seen that at a distance of 0.8 m the average value of the flow density is 38 kW/m^2. The heat flow density corresponds to the modes that are calculated when modeling the heat exchange process in the "torch – polymer particle" and "thermal jet-base" systems.It is necessary to study the "torch – polymer particle interaction" because of the low thermal conductivity of the UHMWPE, thermal destruction. Powder losses in this technological process may be caused by:

- the amount of powder that did not melt in the flame,
- the amount of powder that has been destructed due to a high temperature.

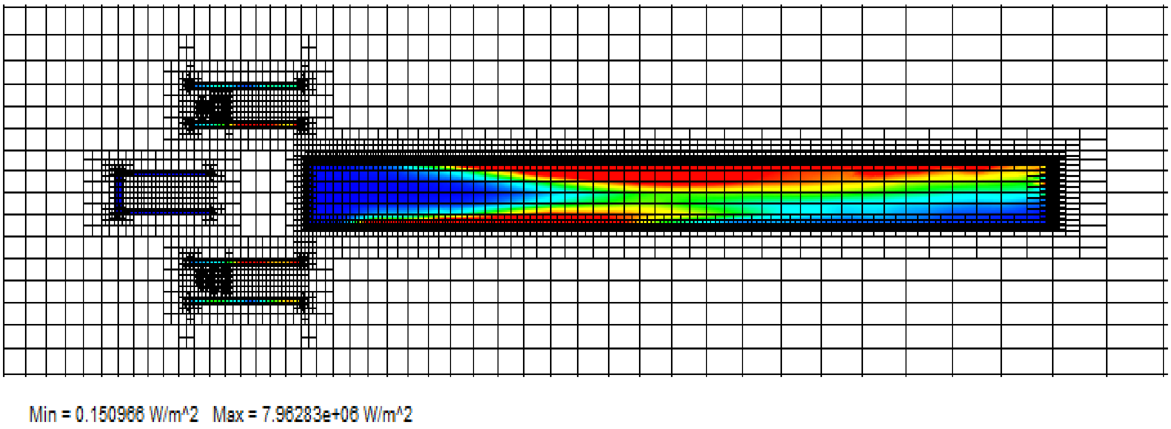

Figure 7 – Picture of heat flow density

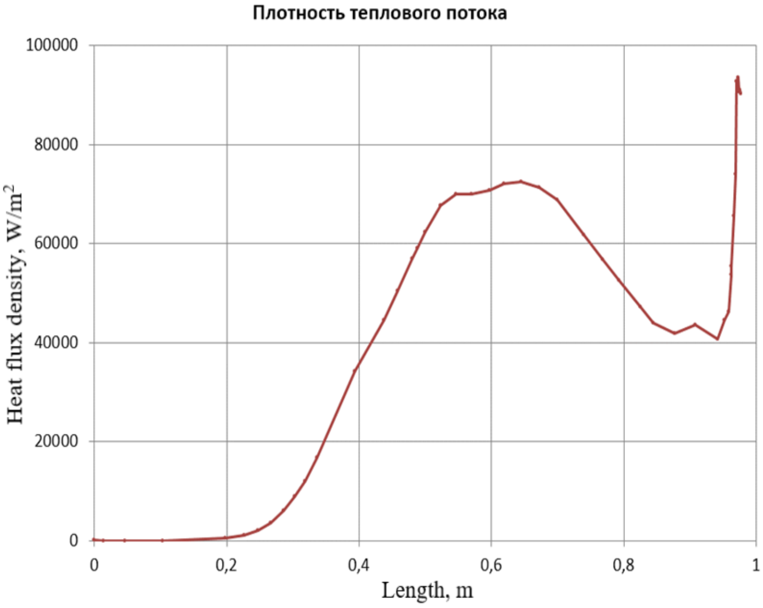

Figure 8 – Change in heat flow density along the torch central axis

This may occur with non-optimal trajectories of the powder particles in the torch. Namely, a particle has a path in the torch that does not correspond to its physical and chemical properties. The particle does not fall into the torch. The thermal power of the torch is less than necessary to melt the entire amount of particles arriving per a unit of time.

3.3 Modeling of heat transfer processes in the "torch – polymer particle", "thermal jet-base" systems

In the result of the calculated work, the trajectories of a particle motion in the torch have been obtained (Figure 9). It can be seen that the powder particles are placed along the cylinder axis and move in the calculated central axis of the flame, the powder heating is uniform and lies within the specified limits of the temperature and destruction.

Picture 10 shows the change in the heating temperature of UHMWPE particles along the trajectory of their movement at a powder feed velocity of 1 kg/min.

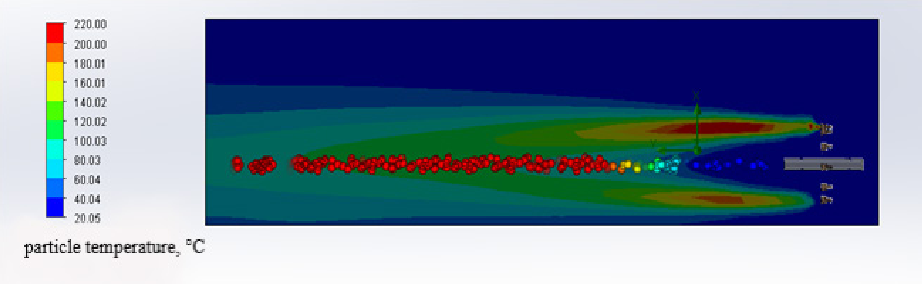

Figure 9 – Picture of the of UHMWPE particles trajectory in the torch

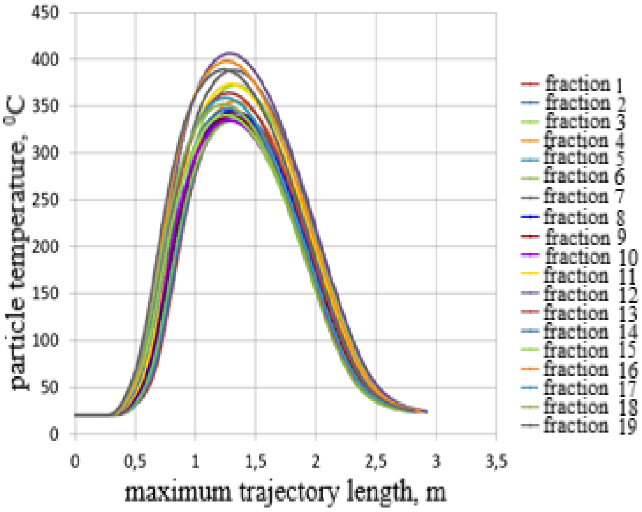

Figure 10 – Particle temperature distribution along the torch length

Figure 10 shows that the particles reach the required temperature at a distance of 0.8 *m*. At the same time, the temperature of the particles is almost the same, which should ensure a uniform structure of the coatings obtained from UHMWPE. The melting point of UHMWPE is 135 – 150^0C. Theoretically, the short-term temperature limit without destruction is 1.5 T_{pl}. The values obtained by us satisfy the specified interval. It also follows from the data obtained that it is necessary to choose a spraying distance of 800 *mm*, which ensures the exposure of a given temperature range.

Figure 11 shows the change in the temperature gradient along the particle cross-section depending on its diameter. The boundary conditions are: the heating time of a powder particle is 0.2 *s*, the average heat flow density is 38 kW/m^2.

It can be seen that, the particle core has a temperature below melting point by 120 C^0 for a UHMWPE particle larger than 0.2 *mm* at a given heat flow density, which will result in incomplete powder melting. Therefore, it is advisable to use powders with a particle size of about 0.05-0.2 *mm*, which corresponds to the physical and chemical properties of the particles during the spraying [20-21].

Figure 12 shows the "thermal jet-base" interaction. The temperature distribution fields are visible depending on the geometry of the bases. It can be seen from the diagrams that the optimal spraying distance is 0.8-1 *m*, since then the torch is less stable and the particles fall into the turbulent flow.

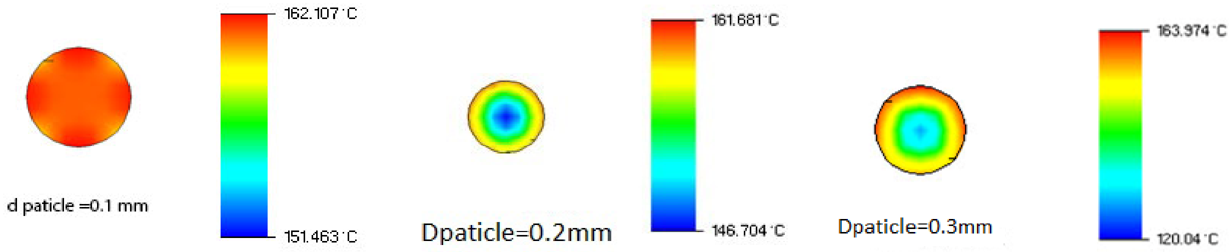

a) b) c)

Figure 11- Temperature gradient along the cross-section of the particle, depending on its diameter: a) d= 0.1 *mm*; b) d=0.2 *mm*; c) d=0.3 *mm*

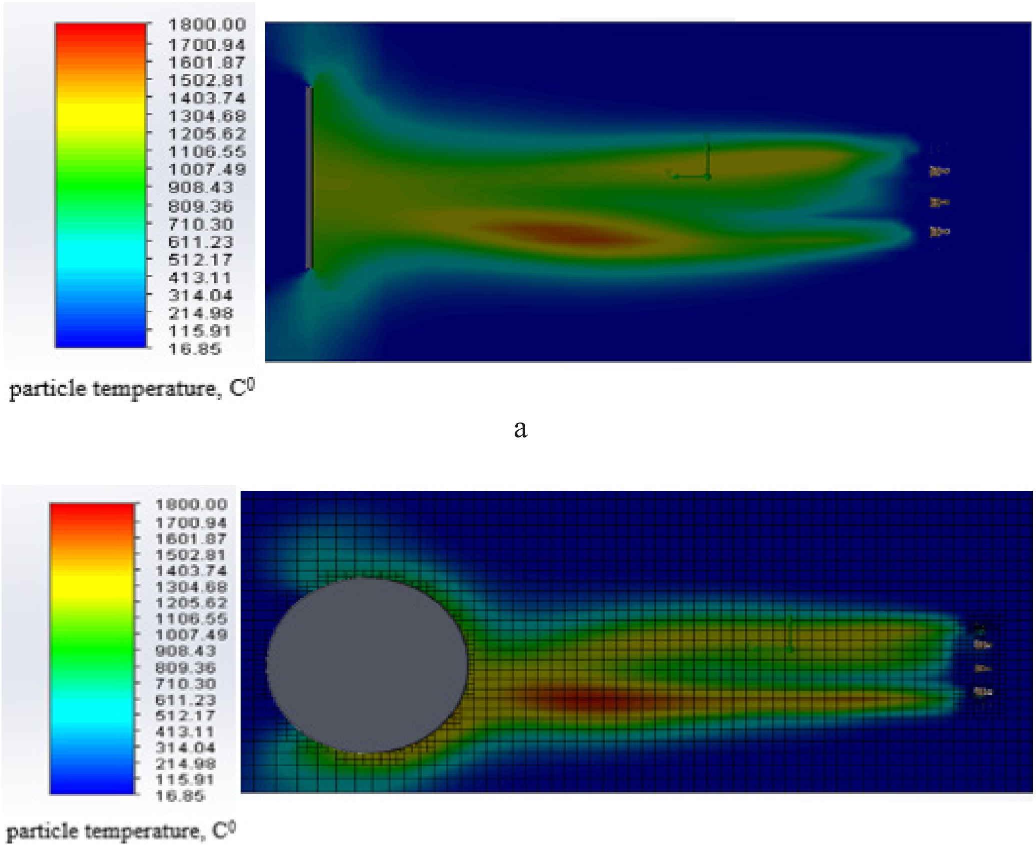

a

b

Figure 12 – Temperature gradient in the interaction of a thermal jet with a flat (a) and cylindrical (b) geometry of bases

4 Conclusions

Thus, in the result of the conducted research, a significant impact of the technological parameters of the gas-thermal equipment to the physical and chemical properties of the burner torch during the processing of SMPE (HVAF method) has been established. The values of the heat flow density and the temperature gradient of the torch, the type of a reaction during the combustion in various modes (recovery, neutral, oxidizing), depending on the mass fractions of the fuel and oxidizer, have been determined. The significant role of the torch temperature as one of the most important factors determining the quality of the polymer obtained coatings has been established. A spatial model of a gas-thermal burner which makes it possible to obtain the thermal modes at a specified technological parameter.has been designed. A physical model of the interaction "torch-polymer particle", "thermal jet –base" has been developed. The necessary heat flow density for the complete melting of the UHMWPE particles which does not exceed the destruction threshold has been determined. The required rate of the UHMWPE powders input into the burner flame has been determined. The optimal geometry of the torch, the trajectory of particles in the torch and the spraying distances have been determined based on the calculations of the "torch-polymer particle interaction". The obtained results of 3D modeling will make it possible to design an experimental installation of UHMWPE high-velocity spraying.

The work has been carried out within the framework of the grant project of the Science Committee of the Ministry of Education and Science of the Republic of Kazakhstan No. AP09259925 "Development and Implementation of a Highly Effective Technology for Applying an Anticorrosive Coating Based on Ultra-High Molecular Weight Polyethylene", 2021-2023.

References

1. Gonzalez R., Ashrafizadeh H., Lopera A., Mertiny P., and McDonald A. A Review of Thermal Spray Metallization of Polymer- Based Structures // Journal of Thermal Spray Technology. – 2016. – Vol. 25(5). – P. 897-919. https://doi.org/10.1007/s11666-016-0415-7
2. Heli Koivuluoto. A Review of Thermally Sprayed Polymer Coatings // Therm Spray Tech. – 2022. – Vol. 31. – Published online. – P. 1750–1764. https://doi.org/10.1007/s11666-022-01404-1
3. Gavrilova R.R., Baldaev L.H., Ilinkova T.A., Baldaev S.L., Mankovsky S.A. Development of a Technique for Applying Protective Coatings to PCM Products by Gas Thermal Spraying // New Technologies, Materials and Equipment of the Russian Aerospace Industry, – 2018. – Conference materials. – P. 149–154.
4. Jing Han, Siyue Ding, Wenge Zheng, Wenya Li and Hua Li. Microstructure and anti- wear and corrosion performances of novel HMWPE/grapheme-nanosheet composite coatings deposited by flame spraying // Polymers advanced technologies. – 2013, Published online in Wiley Online Library. https://doi:10.1002/pat.3161
5. B. Fotovvati, N. Namdari, A. Dehghanghadikolaei. On Coating Techniques for Surface Protection // Journal of Manufacturing and materials processing. – 2019. – Vol. 3(1). https://doi.org/10.3390/jmmp3010028
6. Levchenko I., Shuyan Xu, Baranov O.,Olha Bazaka O., Ivanova E.P., Bazaka K. Plasma and Polymers: Recent Progress and Trends // *Molecules*. A – 2021. – Vol. *26*(13). – P. 4091. https://doi.org/10.3390/molecules 26134091
7. Gatiyatullina R. F., Badrutdinova A. N. Application of Low-Temperature Plasma for the Application of Polymer-Powder Coatings // Bulletin of Kazan Technological University. – 2014. – Vol. 17(20). – P. 45–48.
8. I. Levchenko, S.Xu, O. Baranov, O. Bazaka, E.P. Ivanova and K.Bazaka. Plasma and Polymers: Recent Progress and Trends // Molecules. – 2021. – Vol. 26(13): 4091 https://doi.: 10.3390/molecules26134091
9. Frey P.J. Mesh Generation. Application to Finite Elements // 2nd ed. – London: ISTE Publishing Company. – 2008. – 814 p.
10. Singiresu S. Rao. The Finite Element Method in Engineering // – Butterworth-Heinemann. – 2018. https://doi.org/10.1016/C2016-0-01493-6
11. Alyamovsky A., Sobachkin A., Odintsov E., Kharitonovich A., Ponomarev N. SolidWorks. Computer Modeling in Engineering Practice // BHV-Petersburg, 2008. 1040 p. (in Russian)
12. Hu Xua, Yuqing Bao, David T, Gawne, Tao Zhang. Process control for thermal-spray deposition of thermoset coatings using computer simulation // Progress in Organic Coatings. – 2016. – Vol. 101. – P. 407-415.
13. Baldaev L.H. Gas thermal spraying // Market DS, 2007. 344 p. (in Russian)
14. G.Mauer, C. Moreau. Process diagnostics and control in thermal spray // Journal of thermal spray technology. – 2022. – Vol. 31. – P. 818-828.
15. Ovchinnikov V.V. "Technology of gas welding and metal cutting": Publishing Center "Academy". – 2016. 240 p. (in Russian)
16. F. Awaja, M. Gilbert, G. Kelly, B. Fox, P.J. Pigram. Adhesion of polymers // Progress in Polymer Science. – 2009. – Vol. 34. – P. 948–968.
17. Podzorova M. V., Tertyshnaya Yu. V., Popov A. A., Nikolaeva S. G. Kinetics of thermo-oxidative degradation of polymer blends based on polylactide // AIP Conference Proceedings. – 2019. –Vol. 2167. – P. 020280. https://doi.org/10.1063/1.5132147

18. T. Dayyoub, A.V. Maksimkin, S. Kaloshkin, E. Kolesnikov, D. Chukov, T.P. Dyachkova, and I. Gutnik. The structure and mechanical properties of the UHMWPE // Polymers (Basel). – 2019. – Vol.11(1), Published online https://doi:10.3390/polym11010023

19. Z. Du, J. Wang, S. Wen, P. Wang, D. Zhang, C. Yin. Study on the Properties of UHMW-PE Film // Advances in Materials Physics and Chemistry, – 2015. –Vol. 5. – P. 337-343. https://doi:10.4236/ampc.2015.58033

20. Sutyagin V. M., Kukurina O. S., Bondaletov V. G. "Basic properties of polymers: National Research Tomsk Polytechnic University": Tomsk Polytechnic University. Tomsk, 2010. – 96 p. (in Russian)

21. Y. Bao, T. Zhang, D.T.Gawne. Influence of composition and process parameters on the thermal spray deposition of UHMWPE coatings // Journal of materials science, – 2005. – Vol. 40. – P. 77-85.

Physical Sciences and Technology. Vol. 9 (No. 3-4), 2022: 69-82

IRSTI 28.17.23

https://doi.org/10.26577/phst.2022.v9.i2.09

Statistical modeling of spray formation, combustion, and evaporation of liquid fuel droplets

S. Bolegenova[1], A. Askarova[1], N. Slavinskaya[2], Sh. Ospanova[1*],
A. Maxutkhanova[1], A. Aldiyarova[1] and D. Yerbosynov[1]

[1]Al-Farabi Kazakh National University, Almaty, Kazakhstan
[2] German Aerospace Centre (DLR), Stuttgart, Germany
[*]e-mail: Shynar.Ospanova@kaznu.edu.kz

(Received 4 October 2022; received in revised form 8 November; accepted 21 December 2022)

This article is devoted to computer simulation of the atomization, combustion, and evaporation processes of liquid fuel drops (heptane) at high turbulence. The paper describes the main characteristics and methods of atomization of liquid fuels and shows the types of special devices used in fuel supply injection systems. As proposed in the paper mathematical model of the combustion of liquid fuel injections at high turbulence consists of the laws of conservation of mass, momentum, transfer of kinetic energy, and conservation concentration of the mixture components. Also, when setting up computational experiments, the chemical model of reacting systems, the turbulence model, and the equations describing evaporation, heat transfer, and interaction with the gaseous medium were taken into account. As a result of the computational experiments performed to study the liquid fuel droplets' injection rate influence on the processes of its spraying and combustion, the optimal combustion mode was established. The obtained data that determine the optimal mode are confirmed by a graphical interpretation of the distribution of temperature fields, the number of combustion products, and particles along the height of the model combustion chamber. These results will contribute to a deep study and construction of the liquid fuels' combustion theory, and an understanding of complex thermal and physical phenomena in combustion chambers.

Keywords: atomization, heptane, injection rate, computational experiment, combustion, evaporation.
PACS number: 07.05.Tp.

1 Introduction

Energy is one of the key sectors of the modern global economy, ensuring economic growth is associated with an increase in energy consumption, while the cost of energy production largely determines the availability of goods and services. The high cost of widely used energy carriers, such as natural gas and high-quality petroleum products, is associated with the depletion of primary energy resources and the insufficient level of their beneficial use. This explains the interest in the use of cheap, low-quality fuels that are not currently in demand by the energy industry. The main reason for the low share of such fuels in the fuel and energy balance is the lack of technologies that meet modern efficiency and environmental safety requirements.

For the thermal power industry, the tasks associated with increasing the efficiency of the use of energy resources are of particular importance. Currently, an urgent task is the disposal of huge amounts of liquid hydrocarbon waste accumulated in industrial enterprises: used motor and transmission oils, lubricating fluids, oil sludge, waste from oil production, and oil refining. Known liquid fuel combustion technologies do not always provide high combustion efficiency and compliance with environmental standards when using low-grade fuels. Such fuels ignite poorly and emit a significant amount of soot. For their combustion, special designs of burners are required to ensure combustion stability and high completeness of fuel combustion without violating the standards for harmful emissions. The solution to this problem is important both in terms of improving the environmental situation and in order to expand the fuel and raw material base of the energy sector through the use of substandard liquid hydrocarbon fuels.

Of particular relevance are studies aimed at developing the scientific background and substantiating the development of new devices and technologies that provide high technical and environmental performance in the production of energy using low-quality hydrocarbon fuels, including solving problems of autonomous heat supply for industrial and residential facilities.

Systematic research shows that transport generates about 25-30% of the total CO_2 emissions in the European Union per year. Electromobility projects aim to significantly reduce the carbon footprint of the sector. Strategies to reduce emissions related to the transport sector are about modes of movement and modernization of the transport system. The amount of CO_2 produced by a specific car depends on many factors.

However, when considering the entire transport sector, passenger cars emit the largest amount of carbon dioxide. Road transport accounts for 72% of total emissions, while passenger cars account for up to 60.7%, which is 43.7% of the total [1, 2]. This is significantly more than in maritime (13.6% of the total) or air transport (13.4%). In the coming decades, statistics on emissions from passenger transport are not optimistic: it is expected to remain at the same level or even increase, rather than decrease.

In 2020, the global carbon ratio (CO_2 emissions per tonne of oil equivalent consumed) decreased by 0.9%, significantly more than between 2010 and 2019 (-0.3%/year) [3-5]. This improvement is due both to a significant decrease in oil consumption, which is associated with pandemic-induced quarantine measures and restrictions in the transport sector, and an acceleration in the electricity's decarbonization generation process: a decline in electricity production at "flexible", usually thermal, power plants because of a reduction in energy consumption. Decreasing energy consumption and steady growth in electricity generation from renewable resources have contributed to a reduction in heat generation and reduced consumption of fossil fuels in the energy sector.

The carbon ratio declined in the EU (-4.4%), the US (-3.4%), Canada (-9.5%), Latin America and Africa (-4.4%). In Asia, the situation has changed to a lesser extent (-0.6%), as in China the carbon coefficient has decreased by only 0.5%, since coal consumption is still growing [4, 5]. This indicator went down in India because of declining coal-fired power generation and in South Korea because of increased nuclear power generation but rose slightly higher in Japan and Indonesia. In addition, the carbon ratio decreased in Russia and Australia due to lower coal consumption, as also in the Middle East (Figure 1) [6].

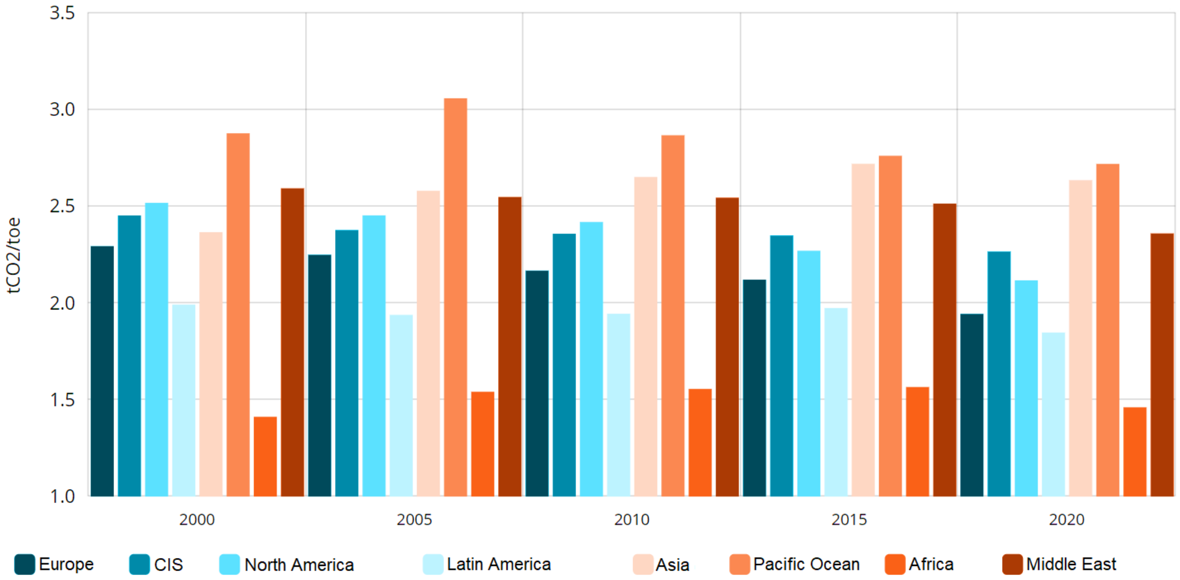

Figure 1 – Evolution trend of the carbon coefficient over the period 1990-2020

When regulating carbon emissions from road transport, it is worth following the European Commission's directives, which are a set of guidelines aimed at reducing carbon dioxide emissions into the atmosphere, including improving the efficiency of the transport system. Improving internal combustion engines and optimizing hydrocarbon fuel combustion processes makes it possible to reduce carbon dioxide emissions.

The concept of convective heat and mass transfer in turbulent currents with chemical reactions is widespread and plays a major role in natural processes as well as in various industries. Knowing the laws of such flows is important in building a theory of combustion physics, in creating new physical and chemical technologies, as a solution to the problems of thermal energy and ecology. In this research, the complex combustion process must be analyzed depending on the influence of numerous physical and chemical parameters of the combustion reaction.

The progress of the formation of liquid droplets theory under high turbulence has a special interest in the study of phenomena in multiphase systems. Research in this area is motivated primarily by environmental problems, in part by problems of atmospheric pollution formation containing toxic heavy metals, sulfuric acid, nitric acid, and other harmful substances.

Reacting systems involve the interaction between several processes occurring simultaneously over a wide range of time and space scales. The release of chemical energy during combustion generates pressure, temperature, and density gradients, which are sources of processes in gases, leading to the transfer of droplets' mass, medium momentum, and the system's internal energy. The strong and ambiguous interaction between the dynamics of liquids and gases and the chemical reactions in them seriously complicates both the experimental study of reacting flows and the development of any more or less rigorous theory. Therefore, numerical simulation can successfully predict and study the behavior of such complex systems. Experimental observations and approximate theoretical models provide laws that an open physical system is supposed to obey. With the help of numerical experiments, it is possible to check the fulfillment of these laws [7].

Methods of mathematical modeling are widely used in various fields of science and technology. These methods include the development of physical and mathematical models, numerical methods and software, and numerical experiments involving computer technology. Its results are analyzed and used for practical purposes. In science and technology, the advantages of the computer simulation method are obvious: design optimization, reduction of development costs, product quality improvement, operating costs reduction, etc. Numerical modeling also significantly transforms the very nature of scientific research, establishing new forms of the relationship between experimental and mathematical methods.

In this way, the study of spray, dispersion, and evaporation of liquid droplets under high turbulence is an urgent problem that can be solved by computer numerical simulation methods.

2 Mathematical model of the problem

The mathematical model of liquid fuels' atomization and combustion processes in the combustion chamber is based on the equations of motion for the liquid phase accompanied by droplets evaporation, as well as on the equations of energy and mass transfer with appropriate initial and boundary conditions.

The continuity equation for the m component is written as follows [8, 9]:

$$\frac{\partial \rho_m}{\partial t} + \vec{\nabla}(\rho_m \vec{u}) = \\ = \vec{\nabla}\left[\rho D \vec{\nabla}\left(\frac{\rho_m}{\rho}\right)\right] + \dot{\rho}_m^c + \dot{\rho}^s \delta_{m1}, \qquad (1)$$

where ρ_m is m component's mass density, ρ is the density of total mass, and u is liquid velocity. After summing equation (l) overall phases, the continuity equation for the liquid is obtained:

$$\frac{\partial \rho}{\partial t} + \vec{\nabla}(\rho \vec{u}) = \dot{\rho}^s. \qquad (2)$$

The momentum transfer equation for the liquid phase is written as [10]:

$$\frac{\partial (\rho \vec{u})}{\partial t} + \vec{\nabla}(\rho \vec{u} \vec{u}) = \\ = -\frac{1}{a^2}\vec{\nabla}\text{p-}A_0 \vec{\nabla}(2/_3\, \rho k) + \vec{\nabla}\vec{\sigma} + \vec{F}^s + \rho \vec{g}, \qquad (3)$$

where p is fluid pressure. The value of A_0 is zero for laminar flows and unity for turbulent flows.

The viscous stress tensor has the following form [11]:

$$\sigma = \mu\left[\vec{\nabla}\vec{u} + (\vec{\nabla}\vec{u})^T\right] + \lambda\vec{\nabla}\vec{u}\vec{I}. \quad (4)$$

The equation of internal energy is as follows [12]:

$$\frac{\partial(\rho\vec{I})}{\partial t} + \vec{\nabla}(\rho\vec{u}\vec{I}) = -\rho\vec{\nabla}\vec{u} + $$
$$+(1-A_0)\vec{\sigma}\vec{\nabla}\vec{u} - \vec{\nabla}\vec{J} + A_0\rho\varepsilon + \dot{Q}^c + \dot{Q}^s. \quad (5)$$

The heat flux vector J is determined by the relation:

$$\vec{J} = -K\vec{\nabla}T - \rho D\sum\nolimits_m h_m\vec{\nabla}(\rho_m/\rho), \quad (6)$$

where T is liquid temperature, h_m is the enthalpy of the m component, $\dot{Q}^c$is the source term due to heat released by a chemical reaction, and $\dot{Q}^s$ is heat brought by injected fuel.

The models with two differential equations are more versatile in engineering calculations of turbulent flows and are most commonly used in technical flows. It is a $\boldsymbol{k-\varepsilon}$ model where two equations are solved: for the kinetic energy of turbulence k and its dissipation rate ε [13-15]:

$$\rho\frac{\partial k}{\partial t} + \rho\frac{\partial \bar{u}_j k}{\partial x_j} = \frac{\partial}{\partial x_j}\left[\left(\mu + \frac{\mu_t}{\sigma_k}\right)\frac{\partial k}{\partial x_j}\right]\frac{\partial \bar{u}_i}{\partial x_j} + $$
$$+G - \frac{2}{3}\rho k\delta_{ij}\frac{\partial \bar{u}_i}{\partial x_j} - \rho\varepsilon, \quad (7)$$

$$\rho\frac{\partial \varepsilon}{\partial t} + \rho\frac{\partial \bar{u}_j \varepsilon}{\partial x_j} - \frac{\partial}{\partial x_j}\left[\left(\mu + \frac{\mu_t}{\sigma_\varepsilon}\right)\frac{\partial \varepsilon}{\partial x_j}\right] = $$
$$= c_{\varepsilon_1}\frac{\varepsilon}{k}G - \left[\left(\frac{2}{3}c_{\varepsilon_2} - c_{\varepsilon_3}\right)\rho\varepsilon\delta_{ij}\frac{\partial \bar{u}_i}{\partial x_j}\right] - $$
$$-c_{\varepsilon_2}\rho\frac{\varepsilon^2}{k}. \quad (8)$$

These are standard $k-\varepsilon$ equations. Simplicity, good convergence, and good accuracy of the $k-\varepsilon$ model allow it to remain the most used model for modeling a wide range of turbulent flows. This turbulence model is widely used because of its simplicity, savings in computational resources, and sufficient accuracy in predicting the properties of both non-reacting and burning flows. The model works well at high Reynolds numbers and high flow turbulence, which has been successfully applied in many works to calculate the characteristics of a reacting flow with chemical transformations. The values c_{ε_1}, c_{ε_2}, c_{ε_3}, σ_k, σ_ε are model constants that are determined empirically [16]. The standard values of these constants are often used in calculations of turbulent flows and are determined experimentally.

3 Statistical model of droplet dispersion and breakup under high turbulence

The turbulent flow affects the liquid jet injected into the cocurrent gas jet moving at a relatively high speed, causing liquid droplets to break up. In the case of droplet breakup upon interaction with a gaseous medium, such random processes as the collision of many droplets, turbulence in the liquid, changes in the cavitation inside flow, and promote the process of disintegration of liquid filaments into drops.

The droplets' breakup idea which is proposed by Kolmogorov obeys the cascading law. According to Kolmogorov's theory, the solid particle's breakup is a discrete random process in which the probability of each parent particle's breakup into a certain number of particles does not depend on the size of the original particle itself. From this generalized assumption follows the conclusion that the particles obey the lognormal distribution law. The discrete model of Kolmogorov was modified into the form of a distribution function evolution equation. This equation's asymptotic solution is used in the droplets' breakup and dispersion model along with the Lagrange model, which is also used to describe the spray dynamics [17-20].

We can consider the breakup of parent droplets into small secondary droplets as a temporal and spatial evolution of the particle distribution in approximation to the size of parent particles according to the Fokker-Planck equation [18]:

$$\frac{\partial T(x,t)}{\partial t} + \nu(\xi)\frac{\partial T(x,t)}{\partial x} = $$
$$= \frac{1}{2}\nu(\xi^2)\frac{\partial^2 T(x,t)}{\partial x^2}, \quad (9)$$

where ν is breakup frequency and t is breakup time. $T(x,t)$ is distribution function for $x = ln(r)$, here r is the particle radius.

Since, at high turbulence, the particle sizes far exceed the instantaneous value of the Kolmogorov length scale, and due to the large variety of turbulence kinetic energy spectra, the drops are deformed and destroyed. In this case, the ratio of destructive hydrodynamic and capillary forces determines the critical radius of drops:

$$r_{cr} = \left(\frac{9}{2}\frac{We_{cr}\sigma\nu_{lam}}{\varepsilon\rho_l}\right)^{\frac{1}{3}}. \tag{10}$$

During atomization, the liquid decomposes into a discrete number of particles, each of which is a group of droplets with an identical size, speed, and direction in space. These groups of droplets, dragging the motionless gas along with them, interact with each other and exchange momentum and energy with the surrounding gas. Liquid fuel is injected from the axial nozzle of the injector as discrete particles with characteristic dimensions equal to the radius of the nozzle outlet. The injection rate is determined by the f liquid fuel injection. When a particle moves in a turbulent gas flow with large-scale structures that are much larger than the particle diameter, the relative velocity between the particle and the gas flow is determined:

$$\frac{d\vec{v}_p}{dt} = \frac{(\vec{v}_g - \vec{v}_p)|\vec{v}_g - \vec{v}_p|}{\tau_{St}}, \tag{11}$$

where $\tau_{St} = \frac{\rho_p d_p^2}{18\rho_g \nu_g}$. When the particle size is larger than the Kolmogorov scale, the turbulent viscosity is governed through the energy spectrum of eddies with smaller sizes compared to the diameter of the particle itself. Figure 2 shows an illustration of this phenomenon.

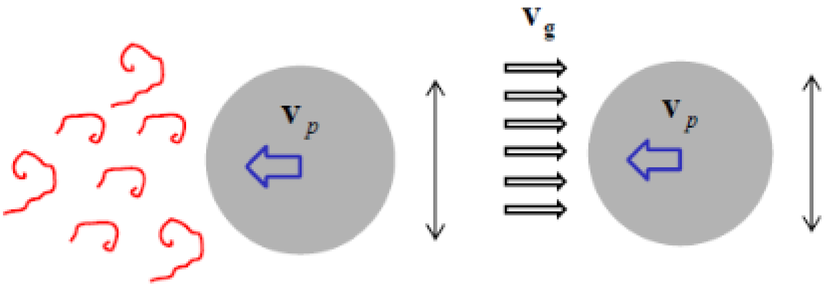

Figure 2 – Comparison of particle sizes with scales of turbulent structures

Now we find the change in particle velocity in a turbulent flow:

$$\frac{\bar{v}_g - v_p}{\tau_{St}} = \bar{\varepsilon}^{\frac{1}{3}}\frac{\rho_g}{\rho_p}\frac{\bar{v}_g - v_p}{d_p^{\frac{4}{3}}}. \tag{12}$$

A mixture of fuel and oxidizer is initially injected into the combustion chamber in the form of a continuous jet, which subsequently breaks up into filaments, which in turn into droplets due to interaction with the gas. Due to the mixing of vapors released by floating liquid fragments with a turbulent gas flow, a chemical combustion reaction occurs. If the spray produced does not break up into small droplets, then the mixing process will not be perfect and combustion will not be complete. As a result of this phenomenon, power is lost, additional fuel consumption occurs, and the emission of pollutants into the atmosphere increases. Comprehension of the complex spray formation process and predicting future processes interests engineers, and researchers in fluid mechanics.

4 Physical model of the problem

In this paper, computational experiments were carried out using liquid heptane fuel. The heptane oxidation process in the combustion chamber proceeds as follows:

$$C_7H_{16} + 11O_2 = 7CO_2 + 8H_2O.$$

Heptane is used as a rocket and reference fuel in determining the octane numbers of automobile and aviation types of gasoline and their components by motor and research methods, and the grade of aviation gasoline in a rich mixture. Heptane is a colorless flammable liquid with a flashpoint of minus 4°C and an autoignition temperature of 223°C. The ignition area of heptane vapor in the air is 1.1-6.7% by volume. Heptane refers to the 3rd hazard class and is a paraffinic hydrocarbon. A liquid jet is injected with a high-velocity gas flow into aircraft and rocket engines. This type of disintegration of the fuel into liquid droplets is called air-blast atomization. In this work, the main attention is paid to modeling the formation and dynamics of the injection during air-blast atomization.

A typical air-blast atomization pattern in aircraft engines is shown in Figure 3 [21, 22]. In such a nozzle, the liquid fuel is injected at low pressure in the form of a thin annular liquid sheet. Two high-speed air streams go along the fluid and transfer a large amount of kinetic energy. Due to this interaction with the gas stream, the liquid sheet separates from both sides. Thereby, the liquid sheets further break up into bundles, threads, and small droplets.

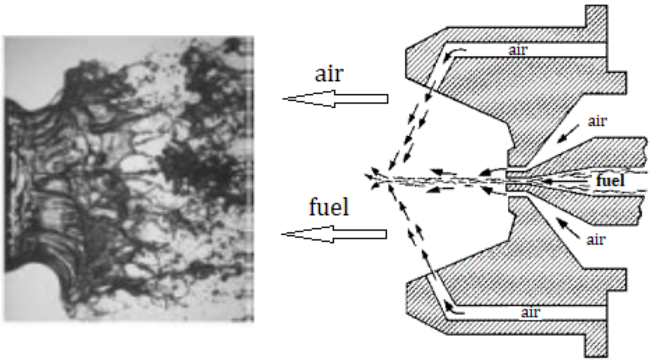

Figure 3 – Scheme of air-blast atomization in an aircraft engine

As can be seen from the figure, the liquid has not yet been fragmented in the nozzle area. This zone, called the liquid core, is a flow region in which the fraction of the mass of the liquid is equal to one, and the bulk of the liquid remains as intact as possible [23]. Many interaction complexes appear at the periphery of the liquid core, which leads to the formation of fibers and their detachment from the liquid core. This liquid core's depletion phase is called primary atomization.

Fragments detached from the liquid core collide with each other. Collisions between fragments can lead to their merging or disintegration. Fragments can also be separated by a fast gas flow that produces small droplets. The phase in which small droplets are produced from large liquid fragments is commonly referred to as secondary atomization. It is clear that the smaller the droplet size, the more intense the evaporation, the better the mixing between the gaseous reactants and, hence, the more efficient combustion. The schematic structure of an aircraft engine is shown in Figure 4.

Liquid fuels' combustion is divided into several stages [24, 25]. At the initial stage, the fuel is injected into the combustion chamber by means of a nozzle into small drops. Before ignition and combustion of the fuel-air mixture, the droplets evaporate and mix with the oxidizer. In the first part of the process, called fuel atomization, the efficiency of the subsequent thorough combustion of the fuel is determined. Since the speed of the processes of evaporation, mixing of fuel with an oxidizer and subsequent ignition directly depends on the size of the formed droplets. Thus, it becomes possible to realize fast (including supersonic) combustion over relatively short lengths.

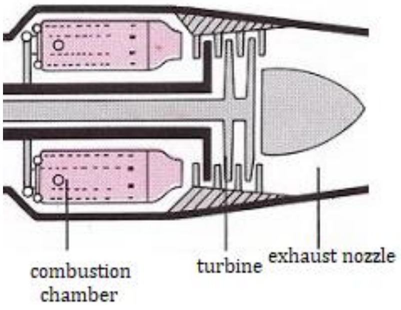

Figure 4 – Schematic structure of an aircraft engine

A combustion zone is established near the drop along a spherical surface, the diameter of which is 1-5 times larger than the droplet size (Figure 5). Droplet evaporation occurs due to the heat of radiation from the combustion zone. In the space between the droplet and the combustion zone, there are vapors of liquid fuel and combustion products. Air and combustion products are in the area outside the combustion zone. Diffusion of fuel vapors occurs inside the combustion zone, while oxygen is outside. Here, these components enter into a chemical reaction, which is accompanied by the release of heat and the formation of combustion products. Heat is transferred from the combustion zone to the outside and the droplet, while the combustion products diffuse into the surrounding space between the droplet and the combustion zone.

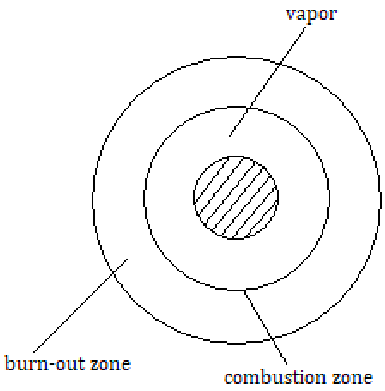

Figure 5 – The thickness of the combustion zone

In our work, when conducting computational experiments, we used a model of a cylindrical combustion chamber. The chamber height is 15 cm, diameter is 4 cm. Figure 6 shows an illustration of the general view of a model combustion chamber. The computational domain consists of 650 cells. Liquid fuel is injected through a nozzle located in the center of the bottom of the combustion chamber. The combustion chamber wall temperature is 353 K.

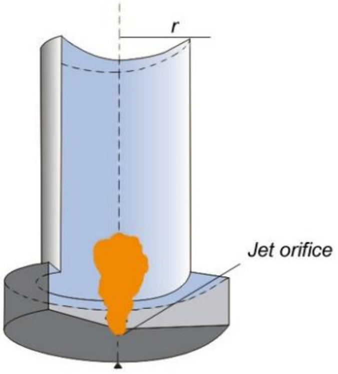

Figure 6 – General view of the combustion chamber

5 Results

This work represents the influence of the liquid fuel injection rate on its combustion using numerical simulation based on the solution of differential two-dimensional equations of a turbulent reacting flow. The injection speed of liquid fuel varied from 150 to 350 m/s. It was found that at low liquid fuel injection rates (less than 150 m/s), combustion does not occur, since in this case the injection rate does not start ignition and stabilize the combustion reaction [26, 27].

The figures below show the results of numerical experiments on the influence of the initial rate of heptane injection in the combustion chamber on the atomization and combustion processes.

Figure 7 shows the combustion temperature distribution in the chamber at different heptane injection rates. Apparently, at an initial speed of 200 m/s the combustion process proceeds slowly and has not become intense. Only at speeds above 250 m/s does the temperature rises along the height of the combustion chamber, the maximum value is 2218 K. Moreover, according to the graph the temperature increases along with the height of the chamber as the injection rate of heptane droplets increases.

The distribution of the temperature plume and the combustion chambers height for heptane is shown in Figure 8. Along with the increase in the droplet injection speed, the height of the plume core increases. For example, at a velocity value of 300 m/s, the maximum temperature propagation area corresponds to a chamber height of 1.7 cm. When particles penetrate the combustion zone along with the chamber height, no noticeable regularity is observed. At a speed value of 250 m/s, the particles rise to a minimum height of 0.56 cm. As a result, it can be said that the speed value at which fuel particles are well dispersed in space is 300 m/s, since at this speed the temperature of particles and intensity of their movements increase, and reach up to 0.81 cm as well as the height of the combustion chamber.

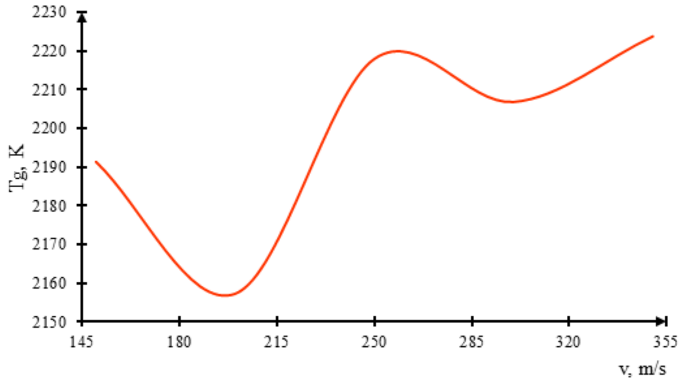

Figure 7 – Dependence of the maximum heptane temperature on the initial droplet injection rate

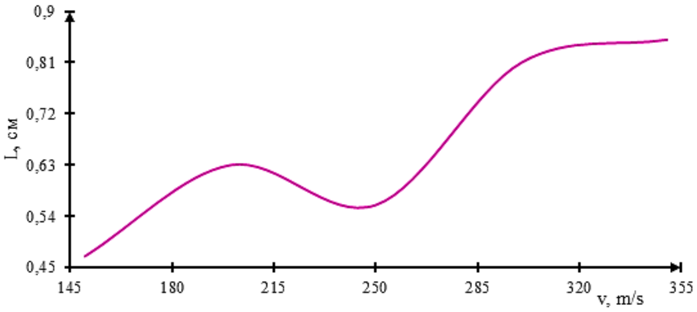

Figure 8 – Distribution of the temperature plume along with the height of the combustion chamber

The Figure 9 shows the concentration distribution of carbon dioxide released in the combustion chamber during the complete oxidation of fuel particles with air. According to the figure, at an initial velocity value of 150 m/s, the CO_2 value is minimal, i.e., 0.128466 g/g. However, as the dispersion rate inside the chamber increases, the intensity of carbon dioxide emission increases. At the speed of 250 m/s, the maximum concentration of carbon dioxide is 0.132253 g/g. The most effective spray velocity at which a moderate carbon dioxide concentration is observed is 300 m/s. At this rate, the CO_2 value is 0.131072 g/g.

Based on the results of the above numerical experiments, the optimal mode of combustion of heptane droplets in the combustion chamber is established at an injection velocity of 300 m/s. At this velocity value, the temperature inside the chamber reaches a relative maximum value, the intensity of particle breakup and collision increases, and the concentration of carbon dioxide released inside the chamber is relatively lower.

Figure 10 shows the evolution of heptane droplets along the radius in the combustion chamber. At the initial moment of the atomization process (2 ms), the radius of the heptane particles inside the chamber is 3.42 μm. The temperature of the particles increases, and their sizes also begin to change due to collision and breakup processes over time. Particles whose radii are equal to the maximum value (10.515 μm) get congregated at a chamber height of 0.68 cm. At the final moments of combustion, particles of a smaller radius predominate. The particle size value concentrated at the exit from the chamber was 5.355 μm.

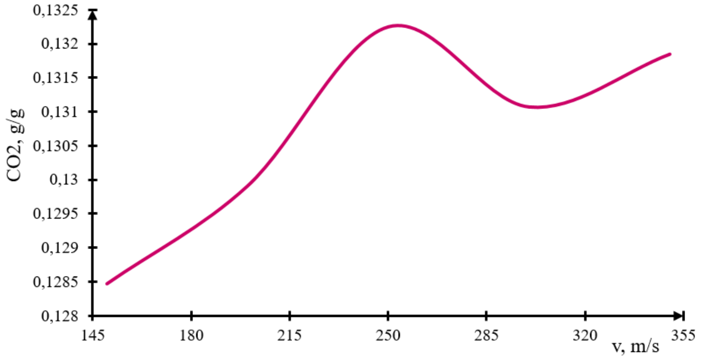

Figure 9 – Distribution of carbon dioxide concentration as a function of injection speed

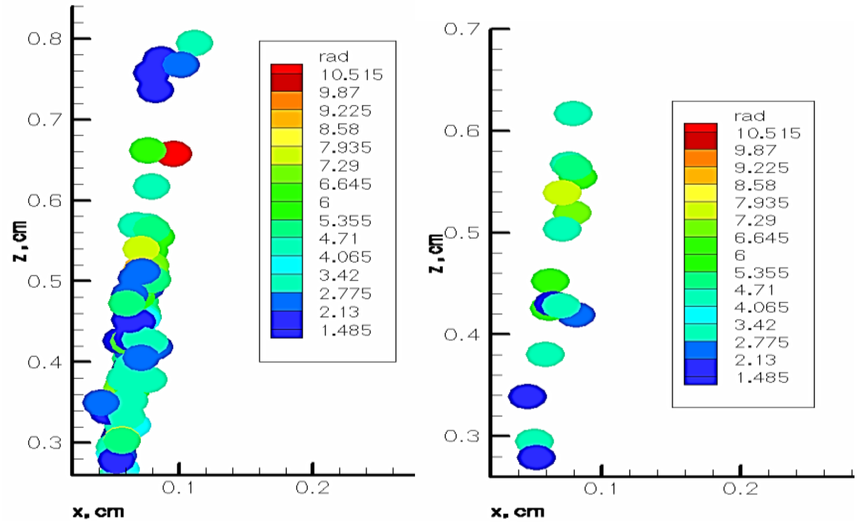

a) t=2 ms b) t=2,5 ms

Figure 10 – Dispersion of heptane droplets along with the height of the combustion chamber

Figure 11 shows the heptane's maximum temperature distribution in the combustion chamber. Liquid fuels maximum combustion temperature at an effective speed of 300 m/s was 2206.84 K. For the rest of the time, a temperature of 1030.39 K was established on the chamber's walls and throughout the combustion space.

The distribution of the concentration of carbon dioxide released in the combustion products is shown in Figure 12. During the combustion process, the concentration of carbon dioxide is allocated uniformly, and any remarkable change is not detected. The minimum concentration of CO_2 at the combustion chamber outlet is 0.0262 g/g.

The distribution of released moisture in the combustion chamber was studied at different times of the entire combustion process (Fig. 13). The moisture concentration at the initial moment of the combustion process increased to 2 cm along the height of the model combustion chamber. Due to the intensive mixing of the fuel with the oxidizer, as well as the combustion of the fuel, the released moisture in the combustion chamber gradually moves towards its outlet. As we can see from the figure, the maximum concentration of moisture is concentrated on the axis of the combustion chamber, the value of which is 0.057 g/g.

One can see in Figure 14 that by applying the statistical dispersion model, more droplets are heated to a temperature of 500 K than in the base model. Both injections also differ in height. With a statistical model, injection drops reach 1.8 cm in height and 0.5 cm in the radius of the combustion chamber. In the first case, the maximum height of heptane droplets is 1.1 cm.

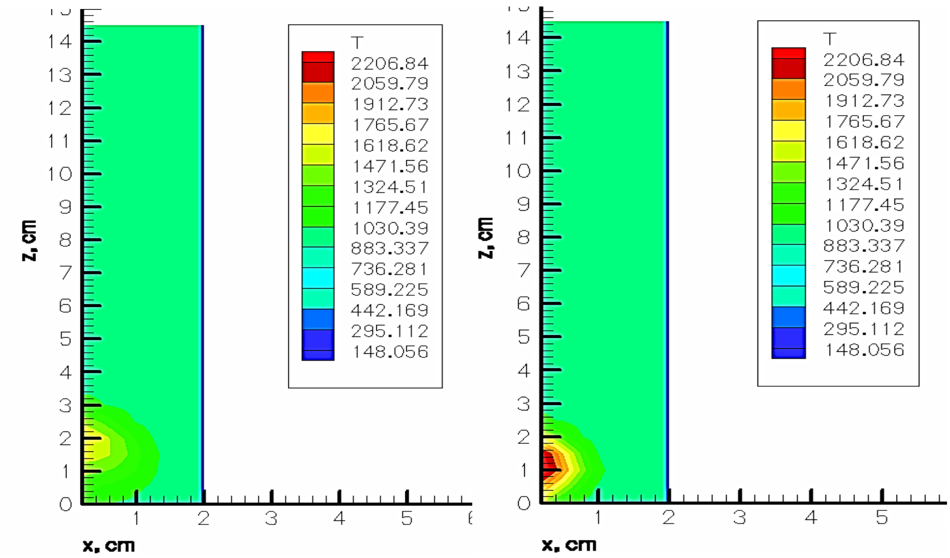

a) t=2 ms b) t=2,5 ms

Figure 11 – Distribution of the maximum combustion temperature of heptane along with the height of the chamber

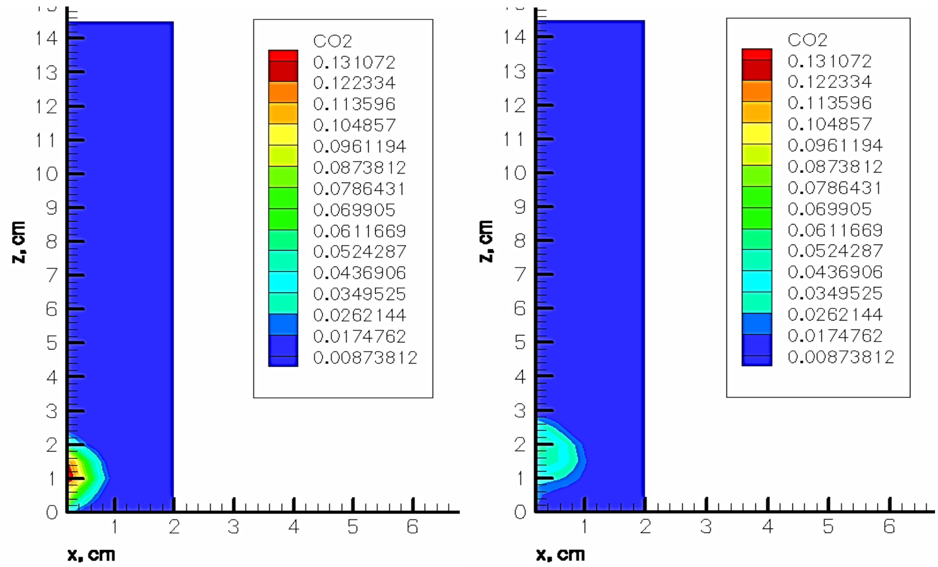

a) t=2 ms b) t=2,5 ms

Figure 12 – Concentration profiles of carbon dioxide at different time moments

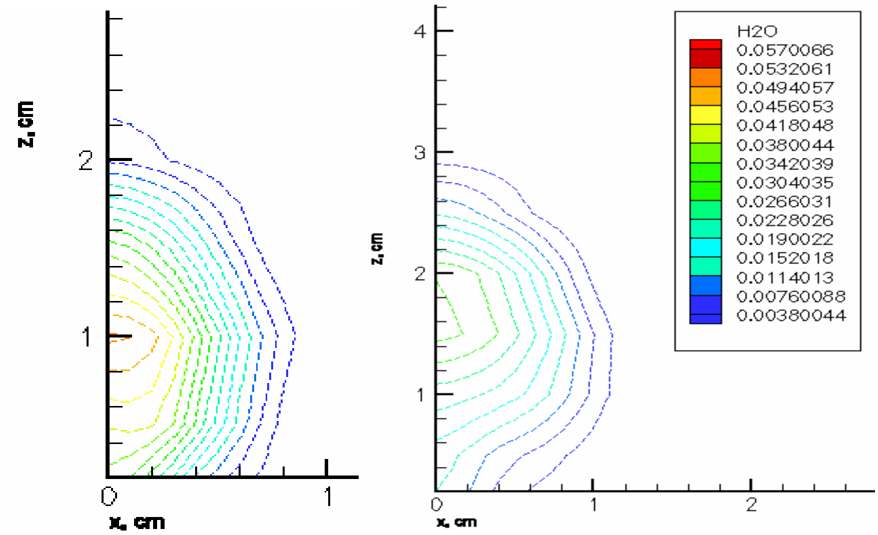

a) t=2 ms b) t=2,5 ms

Figure 13 – Water distribution in the combustion chamber

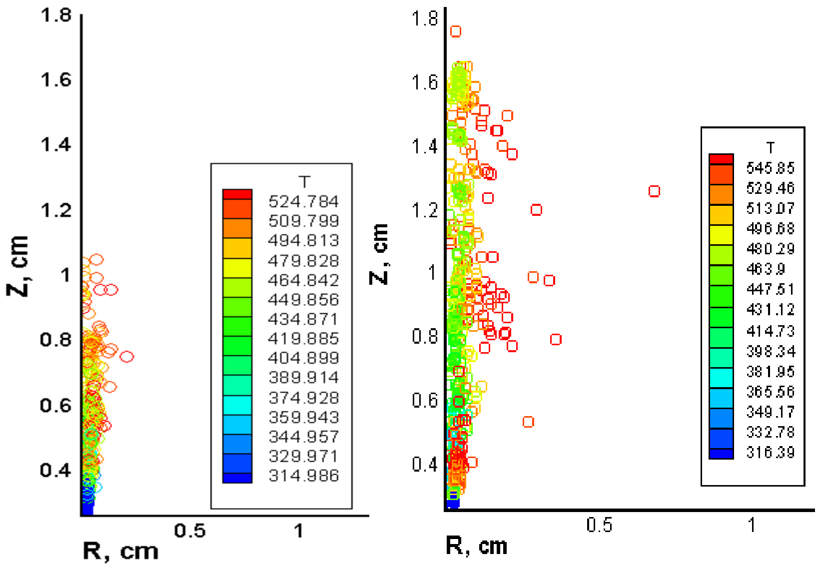

a) t=2 ms b) t=2,5 ms

Figure 14 – Dispersion of heptane droplets by specific temperature

Figure 15 shows the size distribution of heptane droplets in the space of the combustion chamber. Heptane particles, whose sizes have a maximum value at the initial time, are concentrated beneath of the chamber, but they evaporate and rise in height over time.

When performing computational experiments, we studied one of the main criteria for the similarity of thermal processes, the Nusselt number, which characterizes the ratio between the intensity of heat transfer due to convection and the intensity of heat transfer due to thermal conductivity. The Nusselt number is always greater than or equal to 1, the heat flux due to convection always exceeds the heat flux due to heat conduction (Figure 16).

As a result of applying the statistical model in the study of the dispersion and combustion of liquid fuel injections, the droplet distributions in the space of the combustion chamber for heptane were obtained. Taking into account the effect of turbulence on the dispersion of liquid particles using a statistical model of turbulence in liquid fuel combustion calculations, it was found that liquid fuel droplets are atomized over a larger volume, which intensifies the liquid fuel combustion process since the mixing of fuel and oxidizer vapors occurs on a more developed surface.

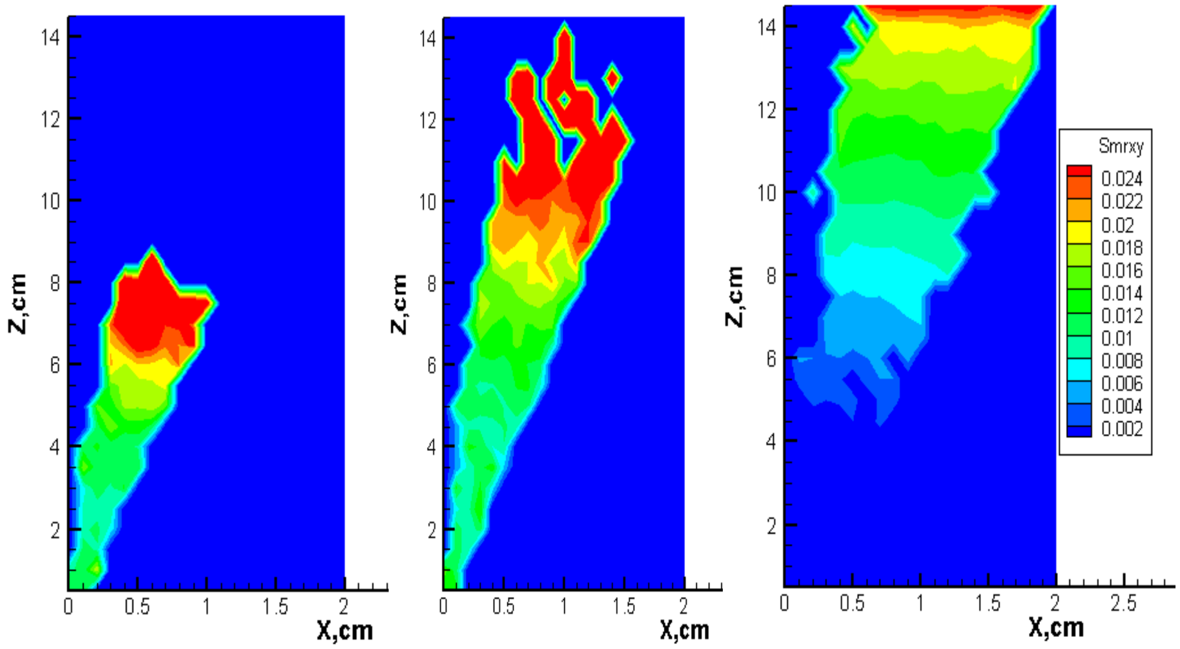

a) t=1.6 ms b) t=2 ms c) t=3 ms

Figure 15 – Dispersion of heptane particles at different time moments

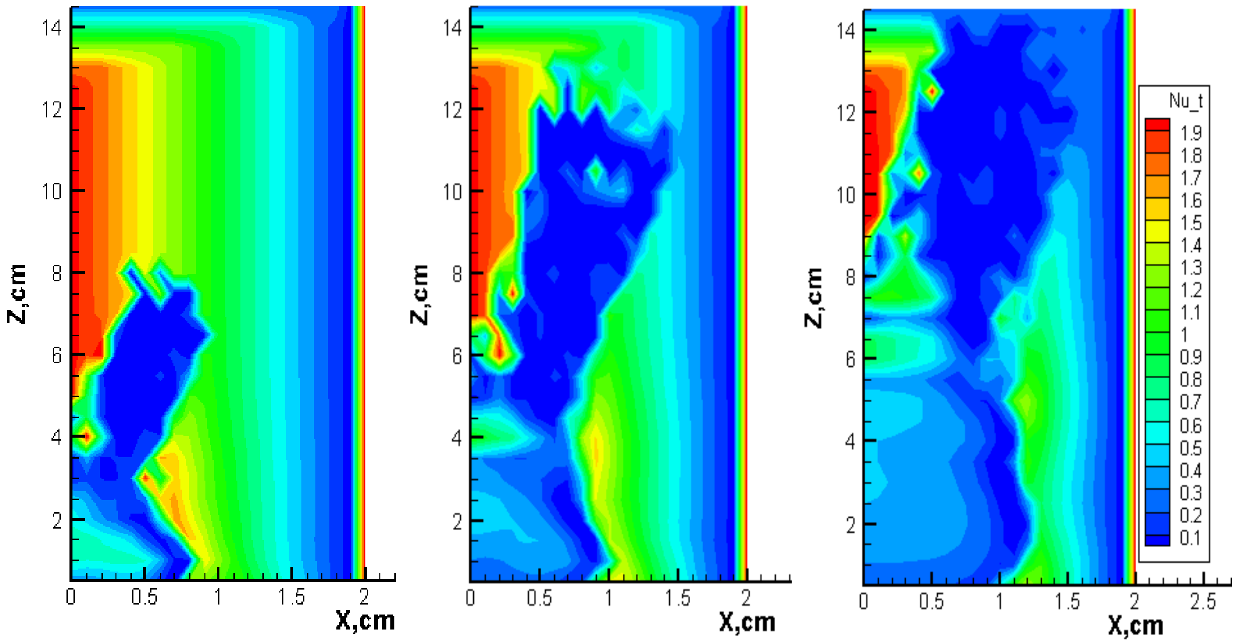

a) t=1.6 ms b) t=2 ms c) t=3 ms

Figure 16 – Nusselt number in the flow at different time moments

Thus, the injection rate influence on the combustion process of heptane in the combustion chamber has been modeled through numerical methods, considering the optimal parameters for the mass of fuel and the initial temperature in the combustion chamber, which were previously determined. The optimum speed for heptane is 300 m/s. The fundamental characteristics of the liquid fuel combustion process are obtained: temperature fields, concentration distributions of fuel and its combustion products, distribution of droplets over radii and temperatures, and velocity fields.

6 Conclusions

The principal features of the combustion of liquid fuel injections are described, and a mathematical model for the formation of dispersion and combustion of non-isothermal liquid injections at high turbulence is presented. The results of a computer experiment on the atomization and combustion of liquid injections using a statistical model are presented. The study of combustion processes depending on the different initial velocities of liquid fuel injection droplets was carried out.

A statistical approach has been proposed to model the dispersion and atomization of liquid fuels in a combustion chamber. The processes of atomization and combustion of heptane injections in a model combustion chamber were studied by means of computational experiments using a statistical model. The distributions of liquid fuel droplets and temperature over time in the space of combustion chamber are obtained.

Due to computational experiments on the injection rate influence on the atomization and combustion of liquid fuel (heptane) processes by using a statistical model, it was found that the optimal combustion mode for heptane occurs at a combustion rate of 300 m/s. At a given speed, the temperature rises, and fuel droplets with an oxidizer react faster and burn without residue.

The theoretical significance of the work is determined by the importance of the results obtained for the development of such branches of knowledge as thermal physics and mechanics of multiphase reacting media. These obtained results will promote to the development of ideas about the regularities of thermophysical processes under the liquid hydrocarbon fuels combustion with continuous supply and the creation of scientific foundations for the development of advanced heat and power technologies.

Using the obtained results in the design of various types of internal combustion engines will simultaneously solve the problems of optimizing the combustion process, increasing the efficiency of fuel combustion and minimizing emissions of harmful substances into the atmosphere. This shows the practical significance of the computational experiments performed in this work.

Acknowledgments

Education and Science Ministry of the Republic of Kazakhstan No. AP14870834 has supported financially this work.

References

1. P. Safarik, et al. Investigation of heat and mass transfer processes in the combustion chamber of industrial power plant boiler. Part 2. Distribution of concentrations of O_2, CO, CO_2, NO // Journal of Applied and Computational Mechanics. – 2018. – Vol. 12. – P. 127-138. http://dx.doi.org/10.24132/acm.2018.396

2. A. Georgiev, et al. The use of a new “clean” technology for burning low-grade coal in on boilers of Kazakhstan TPPs // Bulgarian Chemical Communications. – 2018. – Vol. 50. – P. 53-60.

3. E. Heierle, et al. CFD study of harmful substances production in coal-fired power plant of Kazakhstan // Bulgarian chemical communications. – 2016. – Vol. 48. – P. 260-265.

4. Z Liu, P. Ciais, Z. Deng, et al. Near-real-time monitoring of global CO2 emissions reveals the effects of the COVID-19 pandemic // Nature Communications. – 2020. – Vol. 11. – P. 5172. https://doi.org/10.1038/s41467-020-18922-7

5. G. Janssens-Maenhout, et al. EDGAR v4.3.2 Global Atlas of the three major Greenhouse Gas Emissions for the period 1970–2012 // Earth System Science Data. 2019. – Vol. 11. – P. 959 1002. https://doi.org/10.5194/essd-2017-79

6. International Energy Agency (IEA). Global Energy Review 2020. (IEA, Paris, 2020). https://www.iea.org/reports/global-energy-review-2020.

7. K. Bedikhan, et.al. Application of 3D modelling for solving the problem of combustion coal-dust flame // Bulgarian Chemical Communications. – 2016. – Vol. 48. – P. 236-241.

8. A. Askarova, N. Slavinskaya, et al. Simulation of non-isothermal liquid sprays under large-scale turbulence // Physical Sciences and Technology. – 2021. – Vol. 8, No. 3-4. – P. 28-40. https://doi.org/10.26577/phst.2021.v8.i2.04

9. M. Gorokhovski, S.K. Oruganti Stochastic models for the droplet motion and evaporation in under-resolved turbulent flows at a large Reynolds number // Journal of Fluid Mechanics. – Cambridge University Press, 2022. – Vol. 932. https://doi.org/10.1017/jfm.2021.916

10. P. Safarik, V. Maksimov, et al. 3-D modeling of heat and mass transfer process during the combustion of solid fuel in a swirl furnace // Acta Polytechnica. – 2019. – Vol. 59. – P. 543-553. https://doi.org/10.14311/AP.2019.59.0543

11. R. Leithner, H. Muller, A. Askarova CFD code FLOREAN for industrial boilers simulations // WSEAS Transactions on Heat and Mass Transfer. – 2009. – Vol. 4. – P. 98-107.

12. A. Askarova, et al. Modeling of heat mass transfer in high-temperature reacting flows with combustion // High Temperature. – 2018. – Vol. 56. – P. 738-743. https://doi.org/10.1134/S0018151X1805005X

13. P. Safarik, A. Nugymanova, et al. Simulation of low-grade coal combustion in real chambers of energy objects // Acta Polytechnica. – 2019. – Vol. 59. – P. 98-108. https://doi.org/10.14311/AP.2019.59.0098

14. Sh. Ospanova, et al. 3D modelling of heat and mass transfer processes during the combustion of liquid fuel // Bulgarian Chemical Communications. – 2016. – Vol. 48. – P. 229-235.

15. V. Maksimov, S. Bolegenova, et al. Mathematical simulation of pulverized coal in combustion chamber // Procedia Engineering. – 2012. – Vol. 42. – P. 1150-1156. https://doi.org/10.1016/j.proeng.2012.07.507

16. D.C. Amsden, A.A. Amsden The KIVA Story: A Paradigm of Technology Transfer // IEEE Transactions on Professional Communication Journal. – 1993. – Vol. 36, Issue 4. – P. 190-195. https://doi.org/10.1109/47.259956

17. M. Gorokhovski, V. Saveliev Analyses of Kolmogorov's model of breakup and its application into Lagrangian computation of liquid sprays under air-blast atomization // Physics of Fluids. – 2003. – Vol. 15. – P. 184-192. https://doi.org/10.1063/1.1527914

18. M. Gorokhovski, R. Zamansky Modeling the effects of small turbulent scales on the drag force for particles below and above the Kolmogorov scale // Physical Review Fluids. – 2018. – Vol. 3. – P. 1-23. https://doi.org/10.1103/PhysRevFluids.3.034602

19. M. Gorokhovski, A. Barge Effects of regenerating cycle on Lagrangian acceleration in homogeneous shear flow // Turbulent Cascades II. – 2019. – Vol. 26. – P. 51-58. https://doi.org/10.1007/978-3-030-12547-9_7

20. M. Beketayeva, et al. Influence of boundary conditions to heat and mass transfer processes // International Journal of Mechanics. – 2016. – Vol. 10. – P. 320-325.

21. J. Lasheras, E. Hopfinger Liquid jet instability and atomization in a coaxial gas stream // Annual Review of Fluid Mechanics. – 2000. – Vol. 32. – P. 275-308. https://doi.org/10.1146/annurev.fluid.32.1.275

22. D. Gao, N. Morley, V. Dhir Numerical simulation of wavy falling film flow using VOF method // Journal of Computational Physics. – 2003. – Vol. 192. – P. 624-642. https://doi.org/10.1016/j.jcp.2003.07.013

23. J. Helie, M. Gorokhovski, et al. Air entrainment in high pressure multihole gasoline direct injection sprays // Journal of Applied Fluid Mechanics. – 2017. – Vol.10. – P. 1223-1234. http://dx.doi.org/10.18869/acadpub.jafm.73.241.27628

24. S. Bolegenova, N. Slavinskaya, et al. Investigation of the droplet dispersion influence on the atomization of liquid fuel processes in view of large-scale structures formation // Recent contributions to physics. – 2022. – Vol. 80, No. 1. – P. 75-86. https://doi.org/10.26577/RCPh.2022.v80.i1.09

26. S. Bolegenova, et al. Investigation of the different Reynolds numbers influence on the atomization and combustion processes of liquid fuel // Bulgarian Chemical Communications. – 2018. – 2018. – Vol. 50, Issue G. – P. 68-87.

27. A. Askarova, I. Berezovskaya, et al. Investigation of various types of liquid fuel atomization and combustion processes at high turbulence // Journal of Engineering and Applied Sciences. – 2018.- Vol. 13. – P. 4054-4064. http://dx.doi.org/10.36478/jeasci.2018.4054.4064

Funded by Al-Farabi KazNU

Physical Sciences and Technology. Vol. 9 (No. 3-4), 2022: 83-88

IRSTI 55.03.11 https://doi.org/10.26577/phst.2022.v9.i2.010

Thermophysical characteristics of friction materials based on bronze with 12% tin with the addition of GK-1 graphite powder and foundry coke

A.V. Asach[1*], I.V. Baranov[1], A.A. Kiliashov[1],
V.A. Krylov[1] and A.V. Liashok[2]

[1]ITMO University, St. Petersburg, Russian Federation.
[2]Institute of Powder Metallurgy named after Academician O. V. Roman, Minsk, Republic of Belarus
*e-mail: aakiliashov@itmo.ru

(Received 2 December 2022; received in revised form 22 December; accepted 29 December 2022)

The results of measurements of thermal properties in the temperature range from 20 °C to 100 °C of bronze with 12% tin obtained by powder metallurgy and 30 vol. % carbon-containing additive in the form of powders of graphite grade GK-1 (7-10 microns), foundry coke (less than 63 microns). The specific heat capacity of the samples was measured using the differential scanning calorimetry method. Thermal diffusivity and thermal conductivity were studied by two different methods. In the first case, the thermal diffusivity is determined by the laser flash method and the thermal conductivity by the calculation method. In the second case, the coefficients of thermal diffusivity and thermal conductivity were measured by the flat heat source method. It has been established that 30 vol.% of graphite powder GK-1 in the composition of bronze with 12% tin makes it possible to obtain the value of the thermal conductivity coefficient equal to 23,97 W/(m·K) at 20 °C with its further increase to 25,65 W/(m·K) at 100 °C. The specific heat capacity is 376,71 J/(kg·K) at 20°C and 399,26 J/(kg·K) at 100 °C. The addition of 30 vol.% coke powder makes it possible to obtain a thermal conductivity coefficient equal to 9,03 W/(m·K) at 20 ° C and 10,76 W/(m·K) at 100 °C. The specific heat capacity ranges from 391,80 J/(kg·K) at 20 °C to 413,57 J/(kg·K) at 100 °C.

Keywords: differential scanning calorimetry, laser flash method, hot disk method, heat capacity, thermal diffusivity, thermal conductivity, friction materials, powder metallurgy.
PACS number: 66.70.Df.

1 Introduction

One of the main directions in the development of mechanical engineering is the creation of elements with high performance, reliability and service life. Modern industry puts forward new requirements for the creation of new materials and minimization of the dimensions of units and mechanisms of machines, as well as the improvement of their manufacturing technologies. Powder metallurgy is one of the advanced technologies that makes it possible to implement efficient production, reduce labor costs, re-duce the number of technological operations and create materials with unique properties. Such products, due to their performance indicators, are widely used in automotive and tractor mechanism and special-purpose equipment [1-7].

Friction powder materials based on tin bronze are often used for lubricated friction conditions. They have high wear resistance, thermal conductivity, corrosion resistance, however, during operation they do not provide a high and stable value of the friction coefficient, which is necessary for efficient and stable operation of the friction assembly. Thermo-physical characteristics also affect the efficiency of the friction material, determine its ability to remove heat and work under increased load-speed conditions, the duration of slipping [8-13].

The improvement of properties is possible due to the creation of a heterogeneous structure, through the use of additives of various compositions [14, 15]. The purpose of this study is to determine the temperature dependences of the coefficients of thermal diffusivity, thermal conductivity and specific heat capacity of a friction material based on bronze with 12% tin and 30 vol.% of carbon-containing additives in the form of graphite powder of the GC-1 brand with a fraction of 7-10 microns (composition 1), and foundry coke powder with a fraction of less than 63 microns (composition 2).

2 Experimental part

2.1 Manufacturing technology and sample preparation

The charge of the friction material was obtained by mixing in a paddle mixer powders of copper grade PMS-1 with an average particle size of 80 μm (Fig. 1, a), tin grade PO 1 with an average particle size of 30 μm (Fig. 1, b), graphite grade GK-1 (Fig. 1, c), foundry coke (Fig. 1, d). Mixing time was 45 min. Then the mixture of initial powders was pressed in technological equipment, which made it possible to obtain samples in the form of a disk with a diameter of 25 ± 0,5 mm and a thickness of 2,5 ± 0,5 mm. The resulting samples were sintered in a protectively reducing atmosphere of dissociated ammonia at a temperature of 840 °C for 50 min. The appearance of the samples is shown in Fig. 2, a.

Similarly, samples were prepared for measuring the heat capacity by differential scanning calorimetry. The geometric dimensions of the samples did not exceed 4 mm, the masses of the samples were m_{comp1} = 25,81 mg, m_{comp2} = 47,22 mg (Fig. 2b).

A sample of bronze (CuSn12) was also prepared without the addition of a carbonaceous additive. It was used to assess the influence of alloying components on the values of thermophysical characteristics.

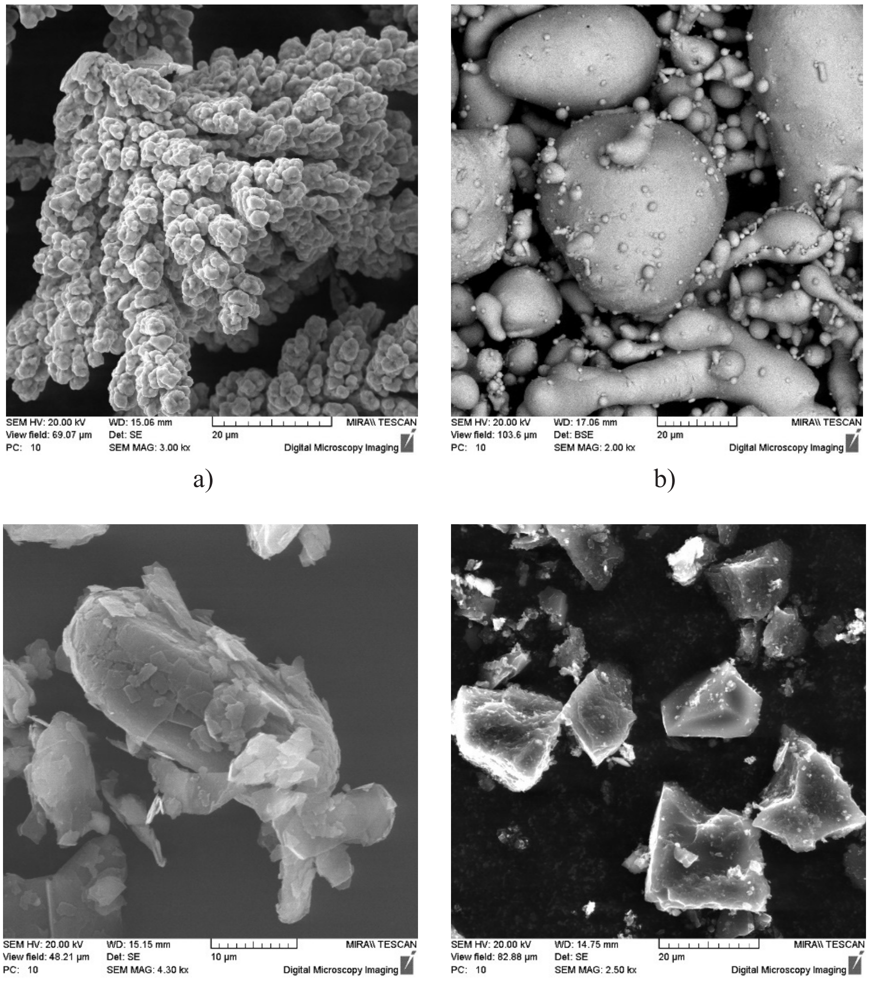

a) b)

c) d)

Figure 1 – The shape of the particles of the initial powders used to obtain the friction material: a) PMS-1; b) PO-1; c) GK-1; d) foundry coke

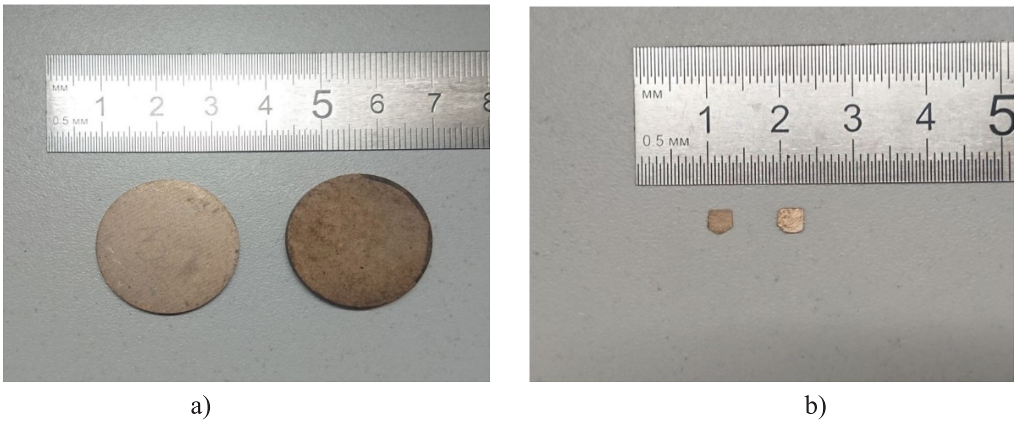

Figure 2 – Appearance of samples for thermophysical testing: a) samples after manufacturing; b) samples for DSC method

2.2 Experimental technique

The thermophysical characteristics of the samples were measured by two methods.

In the first case, the thermal conductivity coefficient λ of the samples was determined by calculation via the ratio:

$$\lambda = \alpha \cdot c \cdot \rho \qquad (1)$$

where *a* is the coefficient of thermal diffusivity; *c* is the specific heat capacity; ρ is the density.

The thermal diffusivity was determined by the laser flash method on an LFA 457 Microflash installation (Netzsch, Germany). The essence of the method is heating one side of the sample with a laser pulse and recording the temperature change on its opposite surface [16]. The measurements were carried out in the temperature range from 20 °C to 100 °C with a step of 20 °C. To increase the absorbency of the material, a thin layer of graphite was deposited on the end surfaces of the samples.

The specific heat capacity was measured on a DSC 204 Phoenix F1 (Netzsch, Germany) installation using differential scanning calorimetry (DSC), which is based on determining the difference in heat fluxes between the test sample and a thermally inert substance (standard) at the same time [17, 18]. The experiment was carried out in the temperature range from 20 °C to 100 °C with a step of 1 °C in the mode of monotonous heating. The heating rate was 10 K/min. Nitrogen gas was used as purge and shield gas at a flow rate of 20 and 50 ml/min, respectively.

The density of the samples was determined by hydrostatic weighing and amounted to ρ_{comp1} = 6142 kg/m^3 and ρ_{comp2} = 5259 kg/m^3.

In the second case, to determine the thermophysical characteristics of the samples, a Hot Disk TPS 2500S thermal constant analyzer (Sweden) was used, which is based on the nonstationary method of a flat heat source (hot disk method) [19, 20]. In this method, a sensor in the form of a double helix was located between the two samples under study, which simultaneously performed the function of both a temperature recording sensor (resistance thermometer) and a source of heat flow. During the experiment, 200 measurements of the electrical resistance of the sensor were performed, and then a function of the change in the temperature of the test sample was built. Based on the analysis of the constructed function, the thermal conductivity and thermal diffusivity of the test sample were determined.

Sensor 7577 F1 with a radius of 2 mm was used in the experiment. Electric power from 200 mW to 300 mW was supplied to it (depending on the material of the samples and their temperature). The time of the experiment was 1 s. Measurements were made in the temperature range from 20 °C to 100 °C with a step of 20 °C.

3 Results and discussion

CuSn12 bronze sample without a carbon-containing additive was studied only at room temperature. Its density was 7106 kg/m^3, and its thermal conductivity was 28 W/(m·K). This value of thermal conductivity corresponds to earlier studies of porous bronze materials [21].

Figures 3-5 show the dependences of the thermophysical characteristics of the materials under study on temperature.

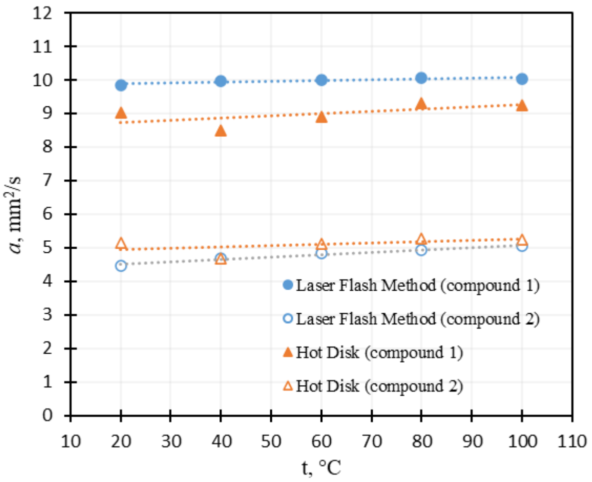

Figure 3 – Dependence of the thermal diffusivity of samples on temperature

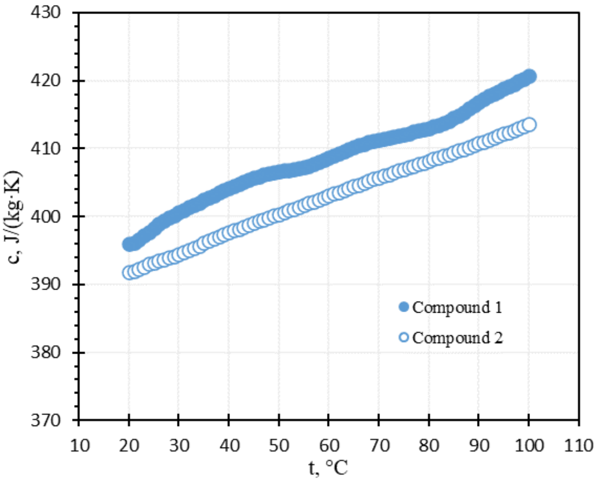

Figure 4 – Dependence of specific heat capacity of samples on temperature

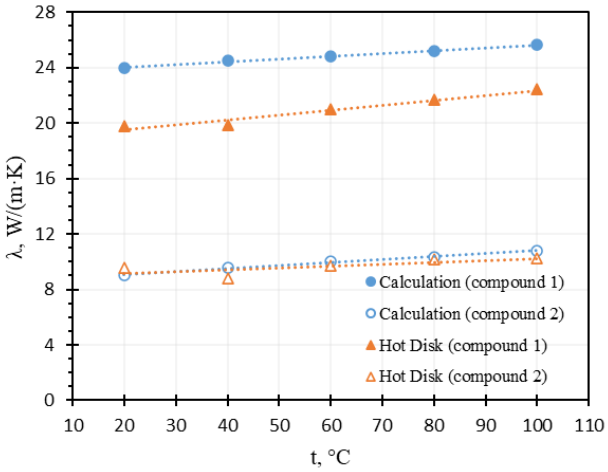

Figure 5 – Dependence of thermal conductivity coefficient of samples on temperature

It can be seen from the graphs that for the studied materials, with increasing temperature, there is a slight increase in thermophysical characteristics, which is typical for metal alloys of bronze. However, the high value of the thermal conductivity of the introduced component did not lead to an increase in the thermal conductivity of the final composition. The thermal conductivity of samples with a carbon-containing additive is lower than the thermal conductivity of pure bronze, the value of which at room temperature is ~28 W/(m·K). This is due to a significant decrease in the density of the material, due to the introduction of a lighter component as an additive. The content of 30 vol.% carbon-containing additive led to a decrease in the density of the final composition by 13% with the addition of GK-1 grade graphite and by 25% with the addition of foundry coke. It is possible that a decrease in the percentage of graphite will lead to an increase in the thermal characteristics of the final composition. This issue requires further research.

In addition to the density of materials, the difference in the values of the thermal conductivity coefficient between the studied materials is explained by the difference in the properties of their additives. The graphite with a crystalline structure used in composition 1 has a higher thermal conductivity value compared to foundry coke powder having an amorphous structure.

4 Conclusions

The paper presents the results of measurements of the thermophysical characteristics of bronze with 12% tin, obtained by powder metallurgy, and 30 vol. % carbon-containing additive in the form of powders of graphite grade GK 1 with a fraction of 7-10 microns, foundry coke with a fraction of less than 63 microns.

It has been established that 30 vol.% of GK-1 graphite powder in the composition of bronze with 12% tin makes it possible to obtain a thermal conductivity value equal to 23,97 W/(m·K) at 20 °C with its further increase to 25,65 W /(m·K) at 100 °C. The specific heat capacity value is 376,71 J/(kg·K) at 20°C and 399,26 J/(kg·K) at 100°C.

The addition of 30 vol.% coke powder makes it possible to obtain a thermal conductivity coefficient of 9,03 W/(m·K) at 20 °C and 10,76 W/(m·K) at 100 °C. The specific heat capacity ranges from 391,80 J/(kg·K) at 20°C to 413,57 J/(kg·K) at 100°C.

References

1. W. B. James. Powder metallurgy methods and applications. In Editted by P. Samal, J. Newkirk. Power Metallurgy. ASM handbook of powder metallurgy. Volume 7. 2015. https://doi.org/10.31399/asm.hb.v07.9781627081757
2. X. Xiao, Y. Yin, J. Bao, L. Lu, X. Feng. Review on the friction and wear of brake materials // Advances in Mechanical Engineering. – 2016. – Vol. 8(5). – P.1-10. https://doi.org/10.1177/1687814016647300
3. A. V. Leshok, L. N. Dyachkova, A. F. Ilyushchenko, A. N. Rogovoy, A. N. Alekseenko. Influence of copper frictional material composition on structure and tribotechnical properties // Journal of Friction and Wear. – 2019. – Vol. 40(6). – P. 495-500. http://dx.doi.org/10.3103/S1068366619060151
4. A. V. Chichinadze. Theoretical and applied problems of thermal dynamics and modeling of friction and wear of friction pairs // Friction and wear. – 2009. – Vol. 30. – No. 3. – P. 275-295.
5. P. A. Vityaz, A. F. Ilyushchenko, V. V. Savich. Powder metallurgy and metallurgical additive technologies. Based on the materials of the European Congress of Powder Metallurgy EuroPM2017 // Powder metallurgy: a collection of scientific papers. – 2017. – Vol. 40. – P. 5-14.
6. A. Lawley, Thomas F. Murphy. Metallography of powder metallurgy materials // Materials Characterization. – 2003. – Vol. 51. – p. 315-327. https://doi.org/10.1016/j.matchar.2004.01.006
7. H. Kuhn, A. Lowley. Powder metallurgy processing: the techniques and analyses. Academic Press: New York, USA, 1978, 222 p.
8. A. F. Ilyushchenko. Modern developments in the field of powder metallurgy for mechanical engineering // Mechanics of machines, mechanisms and materials. – 2012. – Vol. 3-4 (20-21). – P. 113-120.
9. Akhtar S., Saad M., Misbah M.R., Sati M.C. Recent Advancements in Powder Metallurgy: A Review // Materials Today: Proceedings. – 2018. – Vol. 5. – p. 18649-18655. https://doi.org/10.1016/j.matpr.2018.06.210
10. Kurt A., Ates H. Effect of porosty on thermal conductivity of powder metal materials // Materials and Design. – 2007. – Vol. 28. – P. 230-233. https://doi.org/10.1016/j.matdes.2005.06.020
11. Y. Xiao, P. Yao, K. Fan. Powder metallurgy processed metal-matrix friction materials for space applications // Friction. – 2018. – Vol. 6. – P. 219–229. https://doi.org/10.1007/s40544-017-0171-9
12. H. Danninger, R. D. O. Calderon, C. Gierl-Mayer. Powder metallurgy and sintered materials // Additive Manufacturing. – 2017. – Vol. 19. – No. 4. – P. 1-57. https://doi.org/10.1002/14356007.a22_105.pub2
13. K.S Narasimhan. Sintering of powder mixtures and the growth of ferrous powder metallurgy // Materials Chemistry and Physics. – 2001. – Vol. 67. – P. 56-65. https://doi.org/10.1016/S0254-0584(00)00420-X
14. A.P. Ilyushchanka, A.V. Liashok, L.N. Dyachkova, V.P. Biryukov. Effect of iron addition on the structure and properties of copper-based friction powder material used under friction conditions with lubrication // Powder Metallurgy and Functional Coatings. – 2022. – Vol. (1). – P. 76-87.
15. Sutikno M., Marwoto P., Sustad S. The mechanical properties of carbonized coconut char powder-based friction materials // Carbon. – 2010. – Vol. 48. – P. 3616-3620. https://doi.org/10.1016/j.carbon.2010.06.015
16. W. J. Parker, R. J. Jenkins, C. P. Butler, G. L. Abbott. Flash method of determining thermal diffusivity, heat capacity, and thermal conductivity // Journal of applied physics. – 1961. – Vol. 32(9). – P.253-264. https://doi.org/10.1068/htjr119
17. E.S. Watson, M. J. O'neill, J. Justin, N. Brenner. A differential scanning calorimeter for quantitative differential thermal analysis // Analytical Chemistry. – 1964, – Vol. 36. – P.1233-1238.
18. A. V. Fedorov, I. V. Baranov, E. V. Tambulatova, S. M. Volkov, L. T. Prokhorova, V.A. Krylov. Investigation of the temperature dependence of the specific heat capacity of the refined sunflower oils from their composition by the

method of differential scanning kalorimetry // Vestnik Mezhdunarodnoi akademii kholoda. – 2019. – Vol. 1. -P. 52–63.

19. S.E. Gustafsson, E. Karawacki, M.N. Khan. Determination of the thermal-conductivity tensor and the heat capacity of insulating solids with the transient hot-strip method // Journal of Applied Physics. – 1981. – Vol. 52, -No. 4. – P. 2596–2600. https://doi.org/10.1063/1.329068

20. Y. He. Rapid thermal conductivity measurement with a hot disk sensor: Part 1. Theoretical considerations // Thermochimica Acta. – 2005. – Vol. 436, -No.1-2. – P. 122–129. https://doi.org/10.1016/j.tca.2005.06.026

21. P. Grootenhuis, R. W. Powell, R. P. Tye. Thermal and electrical conductivity of porous metals made by powder metallurgy methods // Proceedings of the Physical Society. – 1952. – Vol. 65(7). – P.502-511. https://doi.org/10.1088/0370-1301/65/7/305

Funded by Al-Farabi KazNU

Physical Sciences and Technology. Vol. 9 (No. 3-4), 2022: 89-93

IRSTI 29.19.16 https://doi.org/10.26577/phst.2022.v9.i2.011

Obtaining manganese silicide films on a silicon substrate by the diffusion method

N.F. Zikrillayev, M.M. Shoabdurahimova,
T. Kamilov, A. Zh. Khusanov,
K.K. Kurbonaliev, N. Norkulov and E.B. Saitov-

Tashkent State Technical University, Tashkent, Republic of Uzbekistan
*e-mail: elyor.saitov@yandex.ru

(Received 26 October 2022; received in revised form 23 November; accepted 29 December 2022)

Investigation of auto-oscillation currents in compensated silicon doped with impurity atoms of manganese, zinc, sulphur or selenium can observe several types of current instabilities with different natures and excitation conditions. The boundary regions of auto-oscillation currents such as temperature instabilities, recombination waves and injection instabilities in temperature, electric field, intensity of illumination as well as in resistivity and conductivity type of compensated silicon samples were determined. From the analysis of the obtained results the possibility of using the detected auto-oscillation currents in compensated silicon for creating solid-state generators and sensors of physical quantities is shown. The mechanism of manganese diffusion into silicon leading to the formation of higher manganese silicides on the silicon surface was determined. The X-ray analysis data allowed to find that in the temperature range of thermal annealing T=800÷1100°C, polycrystalline films corresponding to the phases of higher manganese silicides are formed. The possibility of creating the efficient thermopiles based on the obtained structures of the MnxSi1-x – Si<Mn>-MnxSi1-x type based on silicon, the operating parameters of which are not inferior to existing thermopiles, and sometimes have certain advantages, is shown.

Keywords: auto-oscillation currents, electric field strength, illumination, temperature, compensated silicon, amplitude, frequency, heterogeneity, photon energy.
PACS numbers: 73.43.Fj, 73.50.Pz.

1 Introduction

The study of the diffusion distribution of impurities in semiconductor materials, in particular, in silicon, is necessary to elucidate the mechanism of the diffusion process, as well as to determine the role of impurity atoms on the electrical and photoelectric parameters of the source material [1–4].

The process of diffusion of impurity atoms into silicon is carried out in a relatively wide range of high temperatures (T=800÷1300°C), which leads to the formation of additional thermal defects, which strongly affect the fundamental parameters of silicon. In addition, during diffusion, silicides and other metal and dielectric film layers are formed on the silicon surface. The surface state of silicon after diffusion doping with impurity atoms has not been studied in detail. Some authors, when studying the processes of diffusion of impurity atoms into a semiconductor, removed near-surface layers and did not pay attention to studying the surface properties of diffusion-doped silicon [5, 6].

This paper presents the results of a study of silicon doped with impurity manganese atoms, in which higher manganese silicides were formed on the surface. Films of manganese silicides on silicon were obtained in an evacuated quartz ampoule of evacuated high vacuum, about $P=10^{-5} \div 10^{-6}$ mm Hg. Art. [7]. Single-crystal silicon grades KDB-1 and KDB-10, $10 \times 10 \times 0.8$ mm^3 in size, with the [111] crystallographic axis orientation, were used as substrates. The surface of the substrates was cleaned mechanically and chemically before loading into ampoules. The amount of manganese diffusant in the quartz ampoule was based on the calculation of the evaporation time and is sufficient for complete deposition on the silicon substrate. The samples were cooled slowly in air to room temperature without violating the vacuum level in the ampoule. The results of the study showed that by controlling the modes (temperature, time) of the technological process, it is possible to obtain films of manganese silicides with different thicknesses and electrical parameters. These results made it possible to determine the optimal temperature and time for the formation of silicide with the desired parameters.

2 Technology for obtaining materials and research method

The electrical parameters of the obtained films were measured by the Van der Pauw method on the Ecopia HMS-3000 Hall Measurement System, and the electrical resistance and Hall coefficient were determined as a function of temperature. The Hall coefficient in all silicide layers of the obtained silicon samples, regardless of the diffusion temperature and additional thermal annealing, was positive, the concentration of current carriers was equal to $\rho \approx 10^{20}$см$^{-3}$. The dependence of the structure of the formed films on the substrate temperature was also studied. X-ray and electron microscopic methods were used to control the composition and structure of the obtained films. The phase analysis of manganese silicide films was carried out by taking X-ray reflection spectra on a DRON-1 instrument. The topology of the resulting films of manganese silicides and their elemental composition were evaluated using an X-ray microanalyzer in a Ukha-840 scanning electron microscope.

From the analysis of the obtained X-ray patterns, it was found that in the temperature range of thermal annealing T=800÷1100°C, polycrystalline films corresponding to the phases of higher manganese silicides (HSM) are formed. The composition of the films grown in the temperature range T=910÷1040°C, obtained using an X-ray microanalyzer, turned out to be close to the composition of bulk HSM (MnSi). It is established that the formed film microstructures depend on the substrate temperature ($T_{subs.}$). An amorphous film of manganese silicides formed at temperatures T≤880°C, with a subsequent increase in temperatures above T≥970°C, forms a single-crystal layer consisting of manganese monosilicide. The surface topology of the obtained films was studied using a scanning electron microscope. Grain sizes were determined from the surface images of manganese silicide films. For example, in the samples obtained at T=1070°C, the grain sizes are ~5÷20 μm. The electron diffraction patterns for reflection from the surface of the obtained films indicate that they mainly constitute the HSM phase, but, in addition, lines belonging to manganese monosilicide were detected.

It is known that a banded structure is observed in massive HSM crystals, this is due to the precipitation during the growth of interlayers of silicon-depleted manganese monosilicide. An analysis of the structural data suggests that the resulting films, at T≥970°C, the HCM film grows in the form of grains. Thus, in the process of diffusion of manganese atoms into silicon, a flow of atoms is formed, which are deposited on substrates and, as a result of diffusion, form compounds of the MnxSi$_{1\text{-}x}$ type. Structural studies, depending on the technological modes of manganese diffusion, made it possible to optimize the conditions for obtaining manganese silicide films with specified electrophysical parameters.

3 Experimental results and their discussion

An analysis of literature data [8-12] shows that the phase of higher manganese silicides Mn0.25Si1-0.25 (HSM) formed at a thermal annealing temperature in the range T=1050÷1150°C is the most promising material for thermoelectric generators (converters) in photoelectronics. A correlation between the phase composition of silicide films and the coefficient of anisotropic thermal EMF has been established, and the possibility of obtaining polycrystalline films approaching in electrical and kinetic parameters to a massive HSM single crystal has been shown. It was shown that technological factors such as vacuum level, substrate temperature, quartz ampoule volume, substrate surface treatment, and cooling conditions are important for the production of HCM films. Table – 1 shows the values of some physical parameters of the obtained films of higher manganese silicides in silicon, where you can see the systematic dependence of the parameters of the obtained films of manganese silicides on the substrate temperature.

It has been established that the films grown on the basis of the initial KDB-1 and KDB-10 silicon in the temperature range T=1040÷1070°C contained predominantly the HSM polycrystalline phase; in the films grown in the temperature range T=1100÷1200°C, monosilicides were the dominant phase; at temperatures below T≤900°C, the films were amorphous.

Table 1 – Physical parameters of manganese silicide films (vacuum P~10^6 mm Hg, rapid cooling)

Diffusion temperature, °C	Surface resistance, R_r, Ом	Surface resistivity ρ, Ohm×cm	Conversion factor, Sv, µV/W	Hall coefficient, Rx,1/Ohm•cm^{-1}
1120	264	0,004	266	0,065
1110	180	0,012	310	0,059
1070	165	0,023	486	0,062
1040	115	0,026	1880	0,066

The study of the phase composition of the films over the thickness showed that during the evaporation of impurity Mn atoms in a quartz ampoule with a diameter of 10 – 12 mm in vacuum, P≈10^{-5} mm Hg. Art. in the temperature range T=1050÷1100°C with subsequent slow cooling of the samples, polycrystalline films were formed, which near the silicon surface consisted of a mixture of two phases – manganese monosilicide and higher manganese silicides with a predominance of monosilicide, in the upper layer there are mainly HSM phase layers. Interesting scientific results were obtained [13,14] when conducting diffusion in a quartz tube of evacuated vacuum P≈10^{-2} mm Hg. Art. during the entire process of diffusion of manganese atoms into silicon and subsequent slow cooling in air. Under these conditions, films were formed consisting of HSM grains up to 10 µm thick. Additional thermal annealing of the samples in the temperature range T=350÷800°C led to the enlargement of the formed HSM grains. It has been established that such films have a high conversion coefficient [15], and anisotropic properties of kinetic and thermoelectric parameters corresponding to the parameters of bulk HSM single crystals have been found in them.

When studying the topology of the silicon surface with films of higher manganese silicides, it was found that, on average, the grain size is 4–5 µm, although individual crystallites reach up to ≈10 µm. Micrographs of the HSM film grown by us are shown in Fig. 1.

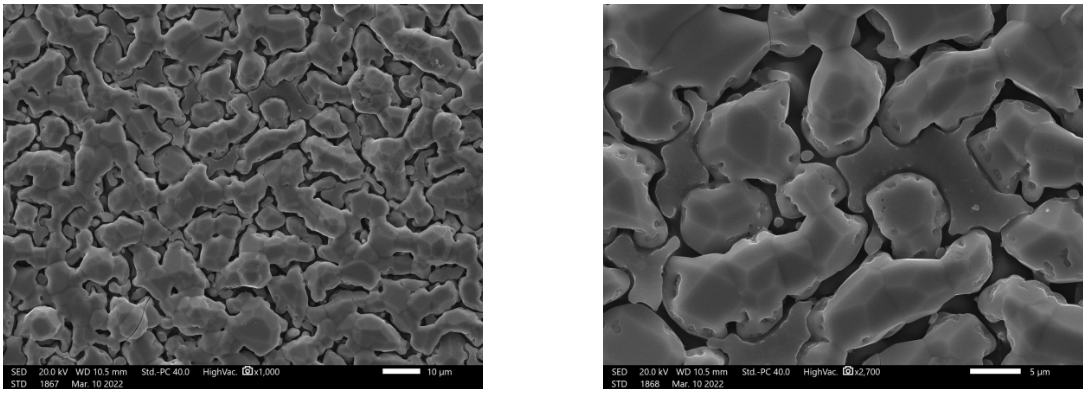

a) at a resolution of 10 µm. b) at a resolution of 5 µm.

Figure 1 – Electron diffraction patterns "for reflection" from a polycrystalline film of manganese silicides on silicon

An analysis of the results of complex studies of the physical properties of higher manganese silicide on the silicon surface, carried out by various modern methods, shows that all numerous crystalline structures have a tetragonal syngony (Fig. 2) and exhibit a superperiodic structure in the direction of the c axis (c is the main crystal growth axis of silicon). The HSM crystal lattice is usually described on the basis of the concept of a "hard" manganese sublattice and a relatively "soft" silicon sublattice. In the manganese sublattice, for all detected HSM phases, one can single out a subcell or nanocluster containing four Mn atoms with a lattice constant parameter along the c axis, which is approximately equal to 4.36Å. Silicon atoms in adjacent layers, perpendicular to the c axis, are arranged in pairs in adjacent squares, which also makes it possible to isolate a subcell of four manganese atoms in the silicon sublattice (Fig. 2).

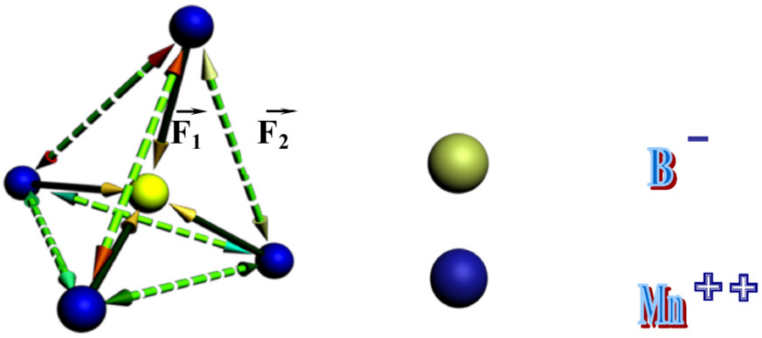

Figure 2 – Structure of a nanocluster of manganese atoms in a silicon lattice $[(Mn)_4^{+8}B^-]^{+7}$.

After analyzing the main regularities of the crystal structure of the studied phases, based on the results obtained, it was concluded that, in reality, the set of structures that can arise in the homogeneity region of HSM is much wider, since a change in the composition of HSM does not lead to the formation of structural defects, but only to a change in the ratios of characteristic sublattice parameters along the c axis. A universal method of description was proposed and all commensurate structures located in the domain of HSM existence were calculated.

4 Conclusions

The crystal axis with the orientation of the tetragonal cell of the manganese sublattice and the pitch of the helix along which the silicon atoms are arranged are incommensurable. It is known that the interaction of periodic subsystems with mutually incommensurable periods leads to the formation of incommensurate structures, which are something intermediate between crystalline and disordered structures. However, despite the absence of periodicity along the axis with any finite period, the diffraction patterns from such structures contain reflections with a small width.

Electron microscopic studies have confirmed the presence of incommensurate superstructures on the silicon surface of higher manganese silicides Mn_xSi_{1-x}. In [16], the authors analyzed the diffraction effects appearing in electron diffraction patterns from crystals with incommensurate modulated structures and orientational anomalies associated with them.

An analysis of the results obtained using a transmission electron microscope showed that, in the grown HSM films with grain sizes on the order of ~10 μm, manganese monosilicide can be present as a polycrystalline phase on the silicon surface as a crystallite.

As a result of the studies carried out, the mechanism of manganese diffusion into silicon was established, leading to the formation of higher manganese silicides on the silicon surface. It has been established that the films grown on the silicon surface consist of HSM grains with the predominant orientation of the c axis perpendicular to the substrate. On the surface of HSM crystallites, manganese monosilicide is present as a polycrystalline phase. Such films have a high conversion coefficient, anisotropic properties of kinetic and thermoelectric parameters are found in them, depending on the direction of the crystallization axis of the silicon substrate.

The possibility of creating efficient thermopiles based on the obtained structures of the type Mn_xSi_{1-x} – Si<Mn>-Mn_xSi_{1-x} based on silicon, the operating parameters of which are not inferior to existing thermopiles, and sometimes have certain advantages, is shown.

Acknowledgements

The work was financially supported by the Ministry of Innovative Development of the Republic of Uzbekistan within the framework of the project F-OT-2021-497 – “Development of the scientific foundations for the creation of solar cogeneration plants based on photovoltaic thermal batteries”.

References

1. B.I. Boltaks Diffusion and point defects in semiconductors. Nauka, Leningrad. 1972, 384 p. (In Russian).
2. M.G. Milvidsky, V.V. Chaldyshev. Nanosized atomic clusters in semiconductors – a new approach to the formation of material properties // Semiconductors. -1998. -Vol. 32. -No. 5. -P. 457-465. https://doi.org/10.1134/1.1187418
3. B.I. Boltaks, M.K. Bakhadirkhanov, S.M. Gorodetsky, G.S. Kulikov. Compensated silicon. Nauka, Leningrad, 1972, 122 p. (In Russian).
4. S. Zainobiddinov. Physical foundations of the formation of deep levels in silicon. Fan, Tashkent, 1984, 160 p.
5. A.A. Tasnin, E.G. Tishkovsky. Formation of selenium-containing complexes in silicon // Semiconductors. – 2002. -Vol. 36, -P. 605-614. https://doi.org/10.1134/1.1485656
6. M.K. Bakhadirkhanov, B.A. Abdurakhmonov. Physical and technological foundations for the formation of clusters of impurity atoms in silicon // Report of the Academy of Sciences of the Republic of Uzbekistan. -2013. -No.3.- P.29-33.
7. N.F. Zikrillaev, K.S. Ayupov, M.M. Shoabdurahimova, K.K. Kurbonaliev. Program for calculating the distribution of diffusion of manganese atoms into silicon from boron atoms on its surface // Intellectual Property Agency under the Ministry of Justice of the Republic of Uzbekistan. No. DGU 16201, 2022 y.
8. A.S. Risbaev, M.T. Normuradov, S.S. Nasriddinov, K.A. Adamboev. Properties of silicide films created by low-energy implantation of metal ions into silicon // Radio engineering and electronics. -1997. -Vol. 42. -No.1. -P. 125-128.
9. A.S. Risbaev. Thin nanoscale silicide films: preparation and properties. Monograph, Tashkent. 2013.
10. A. S. Risbaev, A. A. Risbaev, Zh. B. Khuzhaniezov, A. M. Rakhimov, and L. Kh. On the formation of new surface superstructures during the formation of thin nanoscale films of silicides // Uzbek Journal of Physics. – 2013. -Vol. 15. -No.1-2. -P. 16-32.
11. G.V. Samsonov, L.A. Dvorina, B.M. Dud. Silicides. Moscow, Metallurgy, 1979, 272 p. (In Russian).
12. M.K. Bakhadirkhanov, T.S. Kamilov, A.Zh. Khusanov et al. Investigation of the influence of the layer surface on the photoelectric properties in the structures of higher manganese silicide (HSM) Si-<Mn>-M // Surface. X-ray synchronous and neutron studies. -2002. -No. 6. -P. 100-103.
13. A.S. Risbaev, T.S. Kamilov, V.V. Klechkovskaya, A.S. Orekhov, B.D. Igamov, I.R. Bekpulatov. The influence of structural defects in silicon on formation of photosensitive Mn_4Si_7-Si<Mn>-Mn_4Si_7 and Mn_4Si_7-Si<Mn>-Mn heterostructures // Applied Solar Energy. -2019. -Vol. 55. -No. 6. -P. 380-384. https://doi.org/10.3103/S0003701X19060057
14. A.S. Risbaev, I.R. Bekpulatov. Thermoelectric converters of infrared radiation based on films of higher manganese silicide. Monograph: Ziyo print. Tashkent, Uzbekistan. 2020, 140 p.
15. V.V. Klechkovskaya, A.S. Rysbaev, T.S. Kamilov, I.R. Bekpulatov, B.D. Igamov, I.Kh. Turapov. Formation of thin Mn4Si7 films on various substrates by magnetron sputtering and pulsed laser deposition // Uzbek Physics Journal. – 2021. -Vol. 22. -No. 3. -P. 43-48.
16. A.S. Risbaev, I.R. Bekpulatov, B.Z. Khairiddinov, Zh.B. Khuzhaniezov. Structure and physical properties of nanosized films of metal silicides. Monograph. Tashkent. Adad plus. Tashkent, Uzbekistan. 2017, 230 p.
17. I. Sapaev, E. Saitov, N. Zoxidov, B. Kamanov. Matlab-model of a solar photovoltaic station integrated with a local electrical network // IOP Conference Series: Materials Science and Engineering. -2020. -Vol. 883. -P. 012116. https://doi.org/10.1088/1757-899X/883/1/012116
18. M.K. Bakhadyrkhanov, S.A. Valiev, N.F. Zikrillaev, S.V. Koveshnikov, E.B. Saitov, S.A. Tachilin. Silicon photovoltaic cells with clusters of nickel atoms // Applied solar energy. -2016. -Vol. 52. -P. 278-281. https://doi.org/10.3103/S0003701X1604006X
19. Sh.A. Faiziev, Yu.B. Sobirov. Measurements of solar resources in Uzbekistan // Applied Solar Energy. – 2017. -Vol. 53. -No. 1. -P. 57–60. https://doi.org/10.3103/S0003701X17010054
20. M.K. Bakhadyrkhanov., S.A. Valiev., N.F. Zikrillaev., S.V. Koveshnikov., E.B. Saitov., S.A. Tachilin. Silicon photovoltaic cells with clusters of nickel atoms // Appl. Sol. Energy. -2016. -Vol. 52. -P. 278–28. https://doi.org/10.3103/S0003701X1604006X
21. B.E. Umirzakov, D.A. Tashmukhamedova, M.A. Tursunov, Y.S. Ergashov, G.K. Allayarova. Escape depth of secondary and photoelectrons from CdTe films with a Ba film // Tech. Phys. -2019. -Vol. 64. -P. 1051–1054. https://doi.org/10.1134/S1063784219070260

Funded by Al-Farabi KazNU

CONTENTS